Dynamics of Cell–Matrix Mechanical Interactions in Three Dimensions

Thesis by

Jacob Notbohm

In Partial Fulfillment of the Requirements

for the Degree of

Doctor of Philosophy

California Institute of Technology

Pasadena, California

2013

(Defended May 22, 2013)

Acknowledgments

Throughout my academic career, I have been fortunate to interact with an excellent group of talented and inspiring people. I would like to begin by thanking my adviser, Professor G. Ravichandran. Ravi's flexible mentoring style has given me an ideal academic opportunity to independently pursue my own research interests. Besides an academic adviser, Ravi has served as a mentor, and his guidance has shaped my approach to problem solving in research and life. I would also like to thank the members of my committee: Professors David Tirrell, Kaushik Bhattacharya, and Dennis Kochmann. Dave's insightful comments and suggestions guided much of my work in this thesis. I am grateful for the joint meetings with Kaushik's research group, which have inspired an appreciation for rigorous mathematical analysis. I would also like to thank my undergraduate advisers at the University of Wisconsin–Madison, especially Kevin Turner, who introduced me to scientific research through an undergraduate research opportunity in his lab.

None of my work would have been possible without collaborators in mechanical engineering, bioengineering, and chemical engineering. I am especially thankful for my interactions with senior coworkers: Christian Franck, Chris Kovalchick, Justin Brown, Mike Mello, and Shuman Xia. These academic "older brothers" have provided useful discussion, advice, encouragement, and leadership during my time at Caltech. I am also thankful for support and feedback from all members of the Ravichandran research group: Sharlotte Kramer, Benny Poon, Michael Silva, Laurence Bodelot, Addis Kidane, Maen Alkhader, Victoria Stolyar, Kristen John, Mike Rauls, Aaron Stebner, Aaron Albrecht, and various interns/visiting students. My primary collaborator for the content of this thesis, Ayelet Lesman, has enabled this work through her expertise in

tissue culture, biomaterials, and imaging, and I am grateful for the opportunity to work jointly with her. Caltech staff members have also played an important supportive role in my research. I especially thank Cheryl Gause and Linda Miranda for their administrative assistance and Petros Arakelian for assistance in experimental design, troubleshooting, and maintaining a constant supply of small (but important) laboratory parts.

I thank my family and friends for their support and encouragement. Because scientific research is a constant series of challenges, having a supportive group to discuss both frustrations and triumphs has enabled a positive work environment and a healthy perspective on academia. I am also thankful for the friends I have made during a variety of non-academic activities—from softball and skiing to daily lunchtime conversations. These interactions have taught me that it is truly the people that make Caltech a special place.

Finally, I acknowledge sources of funding, specifically a grant from the National Science Foundation through the Center for the Science and Engineering of Materials at the California Institute of Technology. Additionally, I acknowledge support from the Department of Defense through the National Defense Science and Engineering Graduate Fellowship Program and from the National Science Foundation Graduate Research Fellowship under grant number DGE-1144469.

Abstract

The forces cells apply to their surroundings control biological processes such as growth, adhesion, development, and migration. In the past 20 years, a number of experimental techniques have been developed to measure such cell tractions. These approaches have primarily measured the tractions applied by cells to synthetic two-dimensional substrates, which do not mimic *in vivo* conditions for most cell types. Many cell types live in a fibrous three-dimensional (3D) matrix environment. While studying cell behavior in such 3D matrices will provide valuable insights for the mechanobiology and tissue engineering communities, no experimental approaches have yet measured cell tractions in a fibrous 3D matrix.

This thesis describes the development and application of an experimental technique for quantifying cellular forces in a natural 3D matrix. Cells and their surrounding matrix are imaged in three dimensions with high speed confocal microscopy. The cell-induced matrix displacements are computed from the 3D image volumes using digital volume correlation. The strain tensor in the 3D matrix is computed by differentiating the displacements, and the stress tensor is computed by applying a constitutive law. Finally, tractions applied by the cell to the matrix are computed directly from the stress tensor.

The 3D traction measurement approach is used to investigate how cells mechanically interact with the matrix in biologically relevant processes such as division and invasion. During division, a single mother cell undergoes a drastic morphological change to split into two daughter cells. In a 3D matrix, dividing cells apply tensile force to the matrix through thin, persistent extensions that in turn direct the orientation and location of the daughter cells. Cell invasion into a 3D matrix is the first step required for cell migration in three dimensions. During in-

vasion, cells initially apply minimal tractions to the matrix as they extend thin protrusions into the matrix fiber network. The invading cells anchor themselves to the matrix using these protrusions, and subsequently pull on the matrix to propel themselves forward.

Lastly, this thesis describes a constitutive model for the 3D fibrous matrix that uses a finite element (FE) approach. The FE model simulates the fibrous microstructure of the matrix and matches the cell-induced matrix displacements observed experimentally using digital volume correlation. The model is applied to predict how cells mechanically sense one another in a 3D matrix. It is found that cell-induced matrix displacements localize along linear paths. These linear paths propagate over a long range through the fibrous matrix, and provide a mechanism for cell–cell signaling and mechanosensing. The FE model developed here has the potential to reveal the effects of matrix density, inhomogeneity, and anisotropy in signaling cell behavior through mechanotransduction.

Contents

List of Figures

List of Tables

Chapter 1

Introduction

The fact that biological cells exert mechanical forces on their surroundings is a natural extension of the observation that tissues are composed of collections of cells and structural fibers. The cells act as active machines that convert chemical energy into mechanical energy, resulting in tissue deformation during processes ranging from movement to respiration. Thus, it is well established that an understanding of physiology requires an understanding of the physical processes undergone by the cell. Only recently appreciated however is the fact that mechanical cues control cell behavior in the same way as chemical signals. Cancer can result either from an increase in the stiffness of a cell's environment or a change in the way a cell responds to mechanical force signals [1]. Stem cell differentiation has been shown to depend on the stiffness of the cell's surroundings [2]. The stiffness of a cell's environment also controls cellular development, morphology, migration [3], and expression of genes associated with cell adhesion [4]. With the knowledge of the importance of mechanical signals in dictating cell fate comes the need for quantitative measures of a cell's mechanical state. The observation that mechanical and chemical signals work together to dictate cellular processes has stimulated the development of various experimental approaches to study a cell's mechanical behavior. However, many of the experimental approaches that probe the mechanical behavior of a cell apply forces to the cell [5], causing the cell to actively respond and change its mechanical and chemical state. Thus, passive approaches that do not apply loading to the cell are a better choice for more biologically relevant measurements. One common method of passively quantifying a

cell's mechanical state is through measuring cell traction forces.

1.1 Cell Traction Forces

The term traction refers to the force per unit area at the surface or boundary of a material. Biological cells can be thought as active materials that apply tractions to their surroundings, for example, to migrate. Besides creating a mechanism for migration, cell tractions control a variety of processes including activating stress fiber networks within the cell, triggering mechanosensitive ion channels, changing the cell membrane shape, and modulating cell adhesion receptor conformation [6]. The mechanical signaling required for these processes modulates the cell's chemical environment and therefore controls cellular behavior in a process called mechanotransduction. Mechanotransduction events require interaction between the cell and the surrounding environment through traction stresses. Thus, tractions are present in a wide variety of cellular processes, and quantification of cell tractions can serve as a readout for the physical state of the cell.

1.2 Traction Force Microscopy

Cell tractions are measured using a well-known technique called traction force microscopy (TFM). The working principle behind TFM is that cell-induced deformations are observed in a material with a microscope. Such deformations result from cell traction forces, and they serve as a readout for cell contractile activity. The earliest work on cell traction measurements used a thin polymer membrane as a force sensor [7]. Cells adhered to the membrane and contracted, forming membrane wrinkles as a result of localized membrane buckling. This relatively straightforward approach allowed investigators to directly determine the location of cell tractions. However, due to the nonlinearities associated with membrane buckling, quantitative computation of traction magnitudes and directions was unfeasible. For more quantitative measurements, micron-sized particles were attached to the membrane, and the cell-induced

membrane deformation was deduced by following the particle displacements. Cell traction forces were estimated from the measured particle displacements by performing separate control experiments to determine the relationship between applied force and membrane displacement [8, 9]. Later, others employed a more refined displacement and traction computation, as described in the following sections.

1.2.1 Measuring Cell-Induced Displacements

In TFM, the deformation of the extracellular material is used as a detector for cell tractions. Hence, an accurate traction measurement requires an accurate displacement measurement. Since cells apply tractions at multiple locations, a full-field displacement measurement technique is required. The use of a random array of micron-sized particles offers such a full-field approach. The first TFM experiments to use particles as a readout of substrate displacements simply tracked the translation of individual particles between multiple images [10, 11]. While tracking the motion of individual particles does indeed result in displacement measurements at various points within an imaging field, single particle tracking is subject to noise, with a typical noise floor ranging from 0.05 to 1 pixels [12, 13, 14]. Furthermore, when the particle density becomes too high, particle tracking algorithms cannot distinguish between neighboring particles, which introduces additional sources of error. Since the particle density is directly related to the spatial resolution of the measurement, single particle tracking approaches can inhibit accurate displacement measurements and reduce the spatial resolution.

Compared with following single particles, correlating a subset of particles using digital image correlation (DIC) offers a lower noise floor in the range of 0.01–0.02 pixels [15, 16]. Since a subset of a random arrangement of particles has a unique intensity distribution, DIC can be used with high particle densities. Both free and commercial DIC codes are now commonly available. With these advantages, several authors have begun to apply DIC or other similar subset correlation algorithms to compute cell-induced substrate displacements in TFM experiments [17, 18].

1.2.2 Computing Tractions from Displacements

A typical TFM experiment involves plating cells on a flat substrate and measuring the 2D in-plane substrate displacements. Since information about the substrate displacements is known only at the top boundary, stresses within the substrate cannot be computed directly. Therefore, a mechanical solution is required to solve for the tractions applied by the cells. The earliest work [10, 11, 19] computed tractions by using Boussinesq's solution for a point force applied to an infinite half space (Fig. 1.1), given by [20]

$$\begin{aligned} u_\alpha &= \frac{1+\nu}{2\pi E r}\left[2(1-\nu)F_\alpha + \frac{2\nu x_\alpha}{r^2}F_\beta x_\beta\right] \\ \alpha,\beta &= 1,2 \end{aligned} \tag{1.1}$$

where E and ν are Young's modulus and Poisson's ratio of the substrate, r is given by $r = (x_\beta x_\beta)^{1/2}$, and summation over repeated indices is implied. Here, Eq. (1.1) assumes that the point force acts only in the in-plane (x_1–x_2) directions. Authors have proposed various explanations for only measuring in-plane displacements, including that cells lying on a flat substrate exert tractions only in the in-plane direction [11, 21], that the thin substrate behaves as if it were under a plane stress state [22], and that the cell's height is small compared to its width, so out-of-plane tractions are negligible [23]. The point force solution given in Eq. (1.1) is used as a Green's function to compute the displacements induced by an arbitrary traction field as given below:

$$\begin{aligned} u_\alpha(\boldsymbol{x}) &= \iint_A G_{\alpha\beta}(\boldsymbol{x}-\boldsymbol{x}')t_\beta(\boldsymbol{x}')d\boldsymbol{x}\prime \\ G_{\alpha\beta}(x_\alpha, x_\beta) &= \frac{3}{4\pi E r}\left(\delta_{\alpha\beta} + \frac{x_\alpha x_\beta}{r^2}\right) \end{aligned} \tag{1.2}$$

Here, ν is assumed to be 0.5 and δ_{ij} is the Kronecker delta.

In this approach, displacements—instead of tractions, which are found in the integrand of Eq. (1.2)—are known, and therefore an inverse solution is required. The inverse of the

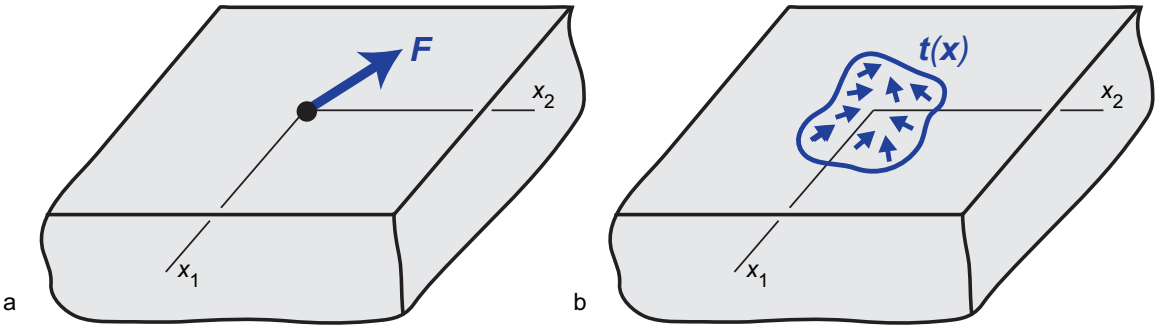

Figure 1.1: The Boussinesq solution for a point force $\boldsymbol{F}$ applied to an infinite half space (a) is used as a Green's function to relate the displacements induced by an arbitrary traction field $\boldsymbol{t}(\boldsymbol{x})$ (b).

Boussinesq approach (Eq. (1.2)) is ill-posed due to sensitivity to noise in the data, and therefore computational processes such as maximizing the Bayesian likelihood that a computed traction profile results in the measured displacements [10, 11] or a Fourier-transform-based solution [19] are required. Other studies have avoided the need for the inverse Boussinesq solution by plating cells on an array of compliant microposts [24]. In these experiments, the cells apply tractions to the posts resulting in post bending. This approach treats the posts as linear, elastic beams, and therefore the force applied to each post can be computed directly after the post displacement is measured.

One drawback of using the Boussinesq solution is that it assumes the substrate is infinitely thick, resulting in traction measurement errors, especially for thin substrates [25]. Thus, more advanced methods of traction computation have been developed that take into account the substrate thickness [25]. Other researchers have computed tractions by inputting the measured displacements as a boundary condition into a finite element framework [26], avoiding the need for an inverse solution and the added computational complexities associated with accounting for a finite substrate thickness.

1.3 Current Shortcomings of Traction Force Microscopy

While TFM has gained widespread popularity in recent years, the technique is still relatively new, having been developed only about 15 years ago. Thus, multiple limitations still remain, including solving the inverse Boussinesq problem, accounting for a finite substrate thickness, quantifying experimental errors, and ignoring out-of-plane tractions. Furthermore, modern TFM experiments use cells plated on flat, artificial substrates that do not reflect the *in vivo* environment of most cell types. These shortcomings highlight a need for further refinement of current TFM approaches and extension of TFM to 3D measurements and systems.

1.3.1 Best Practices

The computational complexity of computing cell tractions (e.g., through Eqs. (1.2)) requires that a researcher interested in quantifying cell tractions have a background in mechanical engineering, applied mathematics, or a similar field. Thus, an interdisciplinary team of researchers consisting of both biologists and engineers often works to answer biologically relevant questions involving cell tractions. To make TFM more approachable to the biology community, there is a need for developing a standard set of "best practices" to quantify and minimize measurement error, thus maximizing the significance of results drawn from TFM experiments. Such best practices would involve recommendations for experimental approaches for displacement measurement and traction computation. These recommendations would minimize experimental noise and error while maximizing spatial resolution. Furthermore, recommendations for experimental conditions that affect the cell's mechanical environment—such as substrate thickness and modulus measurement—would lead to more controlled studies.

While several researchers have investigated the effect of substrate thickness on cell behavior [27, 28, 29] and quantified the modulus of commonly-used polyacrylamide substrates [30, 31], there remains a lack of quantification of error associated with TFM. Currently, most reports of traction experiments are highly subject to experimental and computational error. Even recent work by interdisciplinary teams have reported traction measurement errors in

the range of 25–30% [32, 33]. While errors associated with inaccuracies in displacement measurements can be quantified with control experiments, the errors associated with solving the inverse Boussinesq problem (Eqs. (1.2)) to compute tractions are less well defined. Previous studies have described regularization approaches to solve the ill-posed inverse Boussinesq problem [11, 34, 35], but such regularization procedures further complicate accurate quantification of traction measurement error. Recent work has more thoroughly investigated errors associated with the inverse problem by solving the inverse problem for theoretical displacement fields [33, 35], but performing such a computational study to analyze error in every TFM experiment is not feasible. Thus, there is a need for developing a simpler approach to traction computation that avoids the inverse Boussinesq solution. This thesis describes such an approach, which applies a direct traction computation, avoiding the need to solve an inverse problem. The direct computation approach quantifies the error associated with the displacement and traction measurements in an easily understandable way.

1.3.2 Importance of Three-Dimensional Analysis

While the first TFM experiments assumed that cells on a flat substrate applied tractions only in the in-plane (x–y) directions, recent experiments have demonstrated that cells also apply out-of-plane tractions to flat substrates [36, 37, 38]. While these 3D results have led to insights in how cells mechanically deform a flat substrate, their reliance on the use of cells plated on artificial 2D substrates and kept alive with cell culture medium do not mimic *in vivo* conditions for most cell types. Not only do synthetic 2D substrates fail to replicate a cell's natural chemical environment, but a 3D matrix is also a different mechanical environment for a cell. In three dimensions, the cell interacts with the matrix along curved surfaces and forms adhesions to the extracellular material in three dimensions, in contrast to the discrete in-plane focal adhesions that occur on a flat, 2D substrate (Fig. 1.2). Since the cell's mechanical environment has been shown to control processes such as stem cell differentiation [2], migration [39], proliferation [40], stress fiber formation [41], and others [3], there is a need for experimental

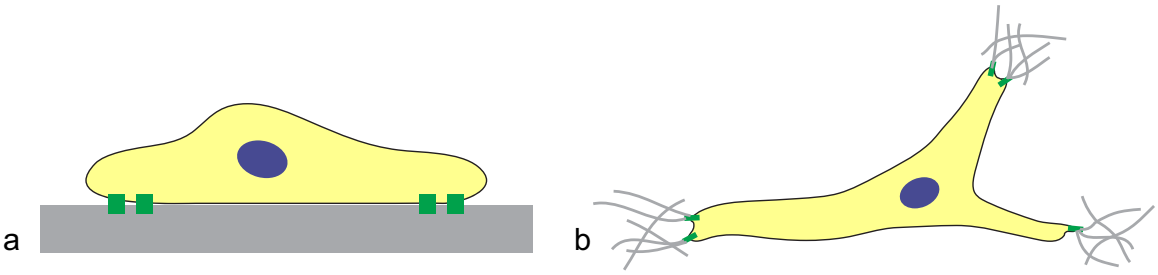

Figure 1.2: A cell's mechanical surroundings are different in two and three dimensions. (a) A cell adheres to a 2D substrate at discrete points along a single plane. (b) In a 3D matrix, a cell interacts with a fibrous matrix, forming non-flat, curved surfaces.

techniques to characterize a cell's mechanical behavior in three dimensions.

Besides the mechanical differences between two and three dimensions, a 3D matrix made of fibrous proteins represents a useful *in vitro* system for studying cellular processes in a tissue-like environment [42]. The traction forces applied by cells embedded in these matrices remodel fibers and create an inhomogeneous distribution of fiber density. Such perturbations in fiber density control cell behavior by both changing the mechanical stiffness sensed by the cell and controlling gene expression through chemical signaling pathways [43]. Therefore, a more complete understanding of cellular processes such as migration, differentiation, proliferation, and stress fiber formation will require experimental approaches that mimic the cell's 3D environment. Furthermore, the study of mechanics in biology is becoming of interest to communities outside cell biology, including developmental biology and tissue engineering, both of which inherently work with 3D systems. These fields would benefit from an experimental technique capable of measuring cell tractions for cells embedded in 3D systems.

1.4 Outline of This Thesis

This thesis is organized into four main chapters, excluding the introduction, conclusions, and appendix. Chapter 2 describes the development of a dynamic 3D TFM technique for cells encapsulated within a 3D matrix. Experimental noise and error are both quantified, and the 3D TFM approach is demonstrated for spread cells in a 3D fibrin matrix. Chapter 3 studies cell

division, wherein a mother cells splits into two daughter cells. In a 3D matrix, dividing cells mechanically connect and apply tractions to matrix fibers through thin cellular processes that are not observed in two dimensions. Unlike previous work on traction measurements during cell division on a 2D substrate, Chapter 3 describes the mechanics of division in a 3D environment and reveals how the dividing cell's environment controls the positioning of the daughter cells. Chapter 4 uses 3D TFM to examine cell invasion into a 3D matrix, a fundamental process that forms a model system for cell migration and metastasis. In addition to measuring cell tractions, Chapter 4 highlights the importance microstructural characterization through direct visualization of matrix fibers. Finally, Chapter 5 addresses the ability for cells to sense one another mechanically through displacements applied to a 3D matrix. In addition to experimental evidence for mechanosensing, Chapter 5 describes a predictive model for cell-induced displacements and strains in a fibrous matrix. The mechanical model uses the finite element method to simulate the matrix as a random collection of fibers that each support axial stress. The finite element model accurately describes the cell-induced matrix displacements in three dimensions, and it explains the localized matrix microstructural deformations observed by direct matrix imaging.

Chapter 2

Three-Dimensional Traction Force Microscopy

While traction force microscopy (TFM) has become a common technique for measuring tractions applied by cells to a flat, synthetic substrate, there remains a need to measure cell tractions in a biologically relevant three-dimensional (3D) environment. Developing a 3D TFM technique has a variety of challenges, including the need for quantitative 3D imaging and data analysis, employing a biologically relevant 3D extracellular matrix, and maintaining cell viability throughout the experiments. This chapter describes the application of confocal microscopy for quantitative imaging of fibroblast cells encapsulated within a fibrous, 3D matrix. Displacements are measured throughout the fibrous matrix in three dimensions using digital volume correlation (DVC). The experimental noise and error associated with displacement and strain measurements using DVC are analyzed. The 3D TFM method is demonstrated by measuring cell-induced displacements in a 3D matrix. Finally, tractions applied by the cell to the matrix are computed directly from the displacement data.

2.1 Confocal Microscopy

Measuring cell tractions in three dimensions requires an imaging approach that can render a 3D volumetric image. Confocal microscopy, originally designed by Minsky [44] to improve the contrast and resolution of an imaging system, offers a means of obtaining 3D image volumes.

The key feature of a confocal microscope is the introduction of a pinhole in the light path (Fig. 2.1). Inspection of Fig. 2.1 shows exactly how the confocal microscope creates an image. Illumination light is sent through a pinhole and focused onto the specimen with a lens. The light then either passes through the specimen (Fig.2.1a) or reflects off of the specimen (Fig. 2.1b) and focuses through a second pinhole and onto a detector. The dotted gray lines in Fig. 2.1 show light paths from a point that does not lie on the focal plane. These light paths are rejected by the pinhole and do not pass through to the detector. Thus, the pinhole has two purposes in the confocal microscope. It increases the resolution by rejecting diffraction rings, and it increases contrast by blocking out-of-focus light. Fine control of the illumination and emission light paths is critical to focus the light through the pinholes; therefore, monochromatic light, generated with a laser, is normally used to prevent optical aberrations caused by refractive index change due to different wavelengths of light.

The enhancement in resolution caused by the pinhole can be evaluated by first considering the resolution of a non-confocal imaging system. Due to the resolution limits of an optical system, a captured image is a convolution of the object and the image of a point source, which is a diffraction spot called the point spread function (PSF). The PSF is well-approximated by [45]

$$\mathrm{PSF}(u,v) = \left[\int_0^1 J_0(v\rho)\exp(iu\rho^2/2)\rho d\rho\right]^2, \tag{2.1}$$

where u and v are optical dimensionless coordinates given by $u = 2\pi \mathrm{NA}^2 z/(\lambda n)$ $v = 2\pi \mathrm{NA} r/\lambda$. Here, z and r are spatial coordinates in the axial and radial directions. λ is the wavelength of light and NA is called the numerical aperture of the objective, $\mathrm{NA} = n\sin(\theta)$, where n is the index of refraction of the specimen and θ is half the cone angle of light the objective focuses onto the specimen (Fig. 2.2). The resolution of an optical system, defined as the smallest distance that can be measured between two points, can be approximated by computing the distance to

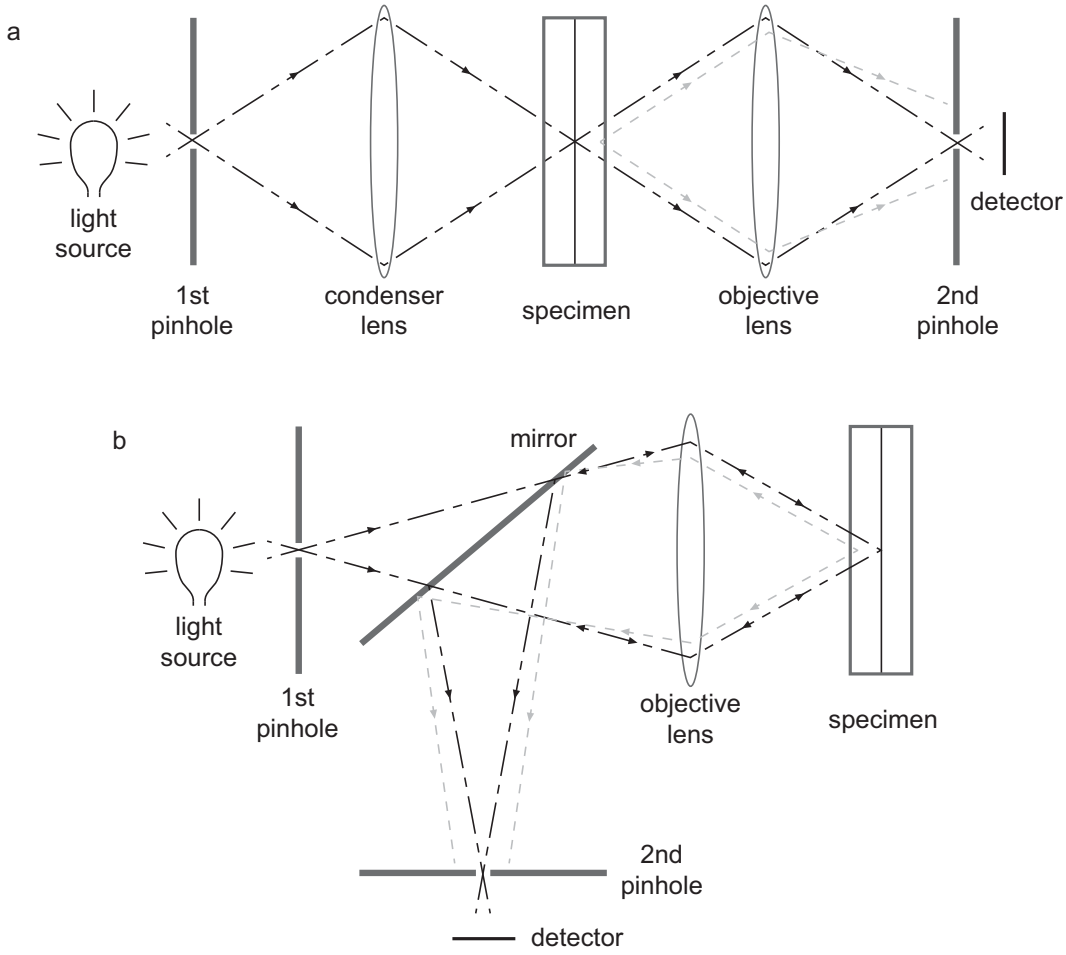

Figure 2.1: Sketch of the primary optical components and light paths in a confocal microscope, adapted from Minsky's original confocal microscope patent [44]. (a) In the transmission approach, light (dash-dot black line) passes through a pinhole and is focused onto the specimen with a condenser lens. It then passes through the sample and is focused through a second pinhole and onto a detector with an objective lens. Out-of-focus light (dotted gray line) from the specimen is rejected by the second pinhole. (b) A confocal microscope in a reflection configuration uses the objective lens to focus the light onto the specimen. A beam splitting or dichroic mirror is used to relay the light to the detector. Again, out-of-focus light is rejected by the second pinhole.

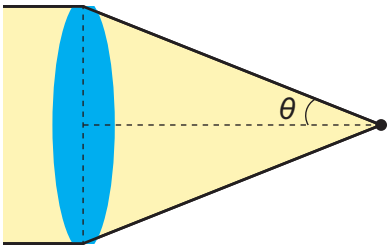

Figure 2.2: θ is defined as half the angle formed by the cone of light that passes through the objective and focuses on the specimen.

the zeros of the PSF in the radial and axial directions:

$$\mathrm{PSF}(0, v) = (2J_1(v)/v)^2, \tag{2.2}$$

$$\mathrm{PSF}(u, 0) = [\sin(u/4)/(u/4)]^2. \tag{2.3}$$

The above equations have zeros at $v = 3.83$ and $u = 4\pi$, respectively. In dimensional coordinates, this corresponds to a PSF radius r and height z given by

$$r = 0.61\lambda/\mathrm{NA}, \tag{2.4}$$

$$z = 2n\lambda/\mathrm{NA}^2. \tag{2.5}$$

Since a confocal microscope uses a pinhole for illumination, the image formed becomes a convolution of the object, the PSF of a point source object, and the PSF of a point source of illumination. For confocal microscopes operating using reflection, the PSF of the illumination and the point source object are the same, because the same objective is used for illumination and imaging. Thus, squaring Eq. (2.1) changes Eqs. (2.4) and (2.5) to

$$\mathrm{PSF}^2(0, v) = (2J_1(v)/v)^4, \tag{2.6}$$

$$\mathrm{PSF}^2(u, 0) = [\sin(u/4)/(u/4)]^4. \tag{2.7}$$

The relative intensities of the PSFs for widefield and confocal microscopy are plotted in Fig.

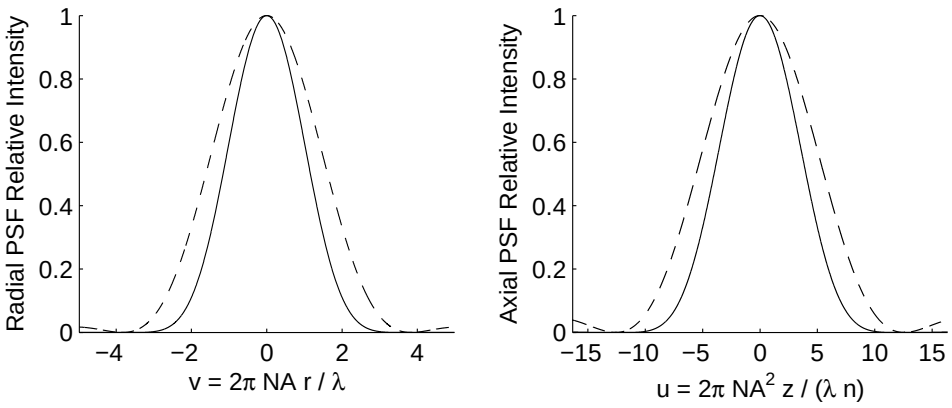

Figure 2.3: The relative point spread functions in the in-plane (v) and axial (u) directions are plotted for a traditional widefield microscope (dotted line) and a confocal microscope (solid line). Zeros are at $v = \pm 3.83$ and $u = \pm 4\pi$.

2.3. While the zeros of Eqs. (2.6) and (2.7) are the same, the full width half maximum is smaller by a factor of about 1.4 [46]. Therefore, the resolution of a confocal microscope is about 1.4 times better than the resolution reported in Eqs. (2.4) and (2.5).

The computation of the resolution of the confocal imaging system does not include the important fact that the pinhole increases contrast in addition to increasing the resolution. As described previously, the pinhole blocks out-of-focus light, allowing for the collection of high contrast images throughout the thickness of a specimen. This effect can be explained mathematically by analyzing the frequency domain analog of the PSF, called the optical transfer function. It can be shown [46] that the transfer function without the confocal pinhole approaches a constant value as the distance from the focal plane z increases, effectively forming a contrast-free gray image. However, with a pinhole, the transfer function goes to zero as z increases for all frequencies, meaning that as the defocus z increases, the signal goes to zero. Therefore, the pinhole in the confocal microscope optically sections a volume into a high contrast slice of finite thickness. Thus, a confocal microscope can be used to stack together planar images collected at different focal depths to assemble an image volume.

Since the pinhole restricts the imaging of a confocal microscope to only a single point, the microscope must scan to acquire an image. The earliest scanning methods used a stage that translated in the x, y, and z directions, which allowed for stacking together a series of images

into an image volume. Modern scanning confocal microscopes use mirrors mounted on galvanometers to scan light across a specimen, forming an image. A disadvantage of the scanning confocal microscope is that a considerable amount of time is required to assemble an image in a point-by-point fashion. Thus, manufacturers recently have begun to make high speed confocal microscopes that use a linear or circular array of pinholes to form an image, which reduces image acquisition time with the trade off of a slight decrease in resolution and contrast [47].

The most common method of forming an image in the biological sciences is through the use of fluorescence. A specimen can be labeled with a fluorophore that absorbs light, leaving it in an excited quantum mechanical state. Upon return to the ground state, the fluorophore emits light at a lower energy than the absorption energy. This energy difference is observed as an increase in the wavelength between excitation and emission. Using optical filters, the excitation light is filtered out so that only the light emitted from the fluorophore reaches the detector, leaving a high contrast image of the biological specimen.

A confocal microscope is not limited to using fluorescence. Confocal reflection microscopy is a common technique used to measure the profile of a surface. In this technique, light reflected directly from the surface is used for imaging, avoiding the need to use fluorescent labels for image formation [48]. The reflection technique has also been applied to biological systems, where backscattered light caused by a mismatch in index of refraction within the specimen creates contrast [49]. However, using backscattered light for image formation in biological materials has the drawback that the light primarily reflects in the direction of the objective axis, resulting in an anisotropic imaging system [50]. In addition to using reflection, one can design a confocal microscope to operate in a transmission mode, as depicted in Fig. 2.1a. However, the transmission design suffers the drawback of requiring a second objective lens and increased difficulty aligning a second pinhole with the light path. Nevertheless, researchers have designed transmission confocal microscopes, circumventing the pinhole alignment problem by replacing the second pinhole with a second harmonic generation crystal that depends on the square of the light intensity. Thus, in-focus light is amplified while out-of-focus light is not,

resulting in a spatial filtering similar to a pinhole [51].

High speed confocal microscopy is used in this thesis to collect image stacks of both cells and their surroundings. Increased image acquisition rates are achieved by using a Swept Field confocal scanner (Nikon Instruments, Melville, NY), which sweeps light across a linear array of pinholes to simultaneously capture multiple confocal spots with a CCD camera. Fluorescence is used for image formation due to its high contrast and the ability to image specific cellular organelles with a targeted fluorescent label. The image stacks of the cell's surroundings then form the basis for displacement computation via digital volume correlation.

2.2 Digital Volume Correlation

Digital volume correlation (DVC) is an extension of digital image correlation, a commonly used, noncontact, optical deformation and strain measurement technique [52]. The DVC technique uses a high contrast speckle pattern to measure displacements of a solid material during deformation. Rather than tracking the motion of single speckles, the technique correlates displacements of small subsets of particles called subvolumes. DVC was first applied to study the deformation of trabecular bone [53]. The bone was imaged through its volume using x-ray microtomography. The porosity of the interior trabecular bone formed a random, high contrast pattern for correlation, and the displacements within the bone specimen under loading were measured with DVC.

Since this early work, others have refined the DVC technique and applied it to other systems. For example, polymer specimens embedded with glass particles have been shown to achieve sufficient contrast for DVC when imaged with x-ray microtomography [54]. In addition, a synchrotron has been used as an x-ray source, allowing for magnification of the x-rays and an improvement in spatial resolution to 1 μm. The synchrotron x-ray source produced the ability to use the heterogeneous microstructure of wood to be used as a high resolution speckle pattern [55, 56]. Other imaging techniques such as neutron tomography [57] and magnetic

resonance imaging [58] show promise for volumetric imaging with sufficient contrast for DVC. Important to the biology and soft materials communities, confocal microscopy has been applied to collect volumetric images for DVC by using fluorescent particles embedded in a transparent gel for contrast generation [59]. Typically reported displacement and strain resolutions are in the range of 0.04–0.2 voxel and 0.004%–0.2% strain [53, 54, 60]; however, these values depend heavily on the quality of imaging and speckle pattern.

In addition to the variety of techniques used for image acquisition, various authors have reported enhancements in DVC such as the application of parallel computing for faster computation [54] and a finite-element-based global DVC approach that correlates displacements while simultaneously enforcing smooth displacement fields [61] and mechanical equilibrium of the volume under investigation [62]. Furthermore, DVC is now commercially available for purchase from Lavision, Inc. (Ypsilanti, MI). With these recent advancements in available software and techniques, it is likely that DVC will soon become a routine procedure for measurements of 3D deformation throughout a material.

DVC is used here for quantifying tractions applied by cells to their surroundings. While other displacement measurement techniques such as particle tracking [12] exist, DVC offers the advantage of lower noise, the ability to use a large density of particles to increase spatial resolution, and the ability to compute displacements without using fluorescent particles. The DVC algorithm used in this thesis was originally written by Franck et al. [59]. An illustration of the DVC algorithm is shown in Fig. 2.4. The simplest version of the correlation assumes the subvolumes undergo a mapping from the reference configuration $\boldsymbol{x}$ to the current configuration $\boldsymbol{y}$ that includes only a rigid body translation $\boldsymbol{u}$:

$$\boldsymbol{y} = \boldsymbol{x} + \boldsymbol{u}. \tag{2.8}$$

This simple mapping neglects rotation, stretching, and shearing of the subvolume, but it has the advantage that the DVC computation can be implemented efficiently with a cross corre-

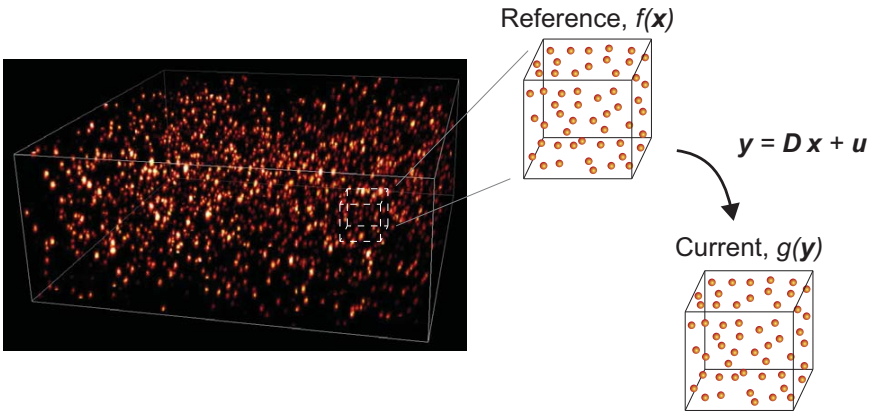

Figure 2.4: The DVC algorithm considers a subvolume within the entire volume stack for correlation. The subvolume is assumed to undergo the mapping from the reference state $\boldsymbol{x}$ to the current state $\boldsymbol{y}$ given by $\boldsymbol{y} = \boldsymbol{D}\boldsymbol{x} + \boldsymbol{u}$, where $\boldsymbol{D}$ is a diagonal tensor consisting of the stretches of the subvolume and $\boldsymbol{u}$ is a rigid body translation of the subvolume. The correlation computes the unknowns $\boldsymbol{D}$ and $\boldsymbol{u}$ such that the image intensity in the reference state $f(\boldsymbol{x})$ equals the intensity measured in the current state $g(\boldsymbol{y})$ as described in the text.

lation. Letting f represent the intensity of the high contrast pattern for a subvolume in the reference configuration and g the intensity in the current configuration, the cross correlation is written

$$c\left(\boldsymbol{u}\right) = \int f\left(\boldsymbol{x}\right) g\left(\boldsymbol{x}+\boldsymbol{u}\right) d\boldsymbol{x}. \tag{2.9}$$

Equation (2.9) can be solved efficiently using the fast Fourier transform by finding the translation $\boldsymbol{u}$ such that the cross correlation c is a maximum:

$$c\left(\boldsymbol{u}\right) = \mathcal{F}^{-1}\left\{\overline{\mathcal{F}\left[f\left(\boldsymbol{x}\right)\right]}\mathcal{F}\left[g\left(\boldsymbol{x}\right)\right]\right\}, \tag{2.10}$$

In Eq. (2.10), $\mathcal{F}$ represents the Fourier transform, and the overbar represents the complex conjugate.

For additional accuracy, the cross correlation implementation of the DVC can also include normal stretches of the subvolumes by writing the mapping

$$\boldsymbol{y} = \boldsymbol{D}\boldsymbol{x} + \boldsymbol{u}, \tag{2.11}$$

where $\boldsymbol{D}$ is a diagonal tensor containing the normal stretch components, and $\boldsymbol{u}$ is the rigid body translation. Under the mapping given in Eq. (2.11), the intensity in the reference configuration f is related to the intensity in the current configuration g by the equation

$$f(\boldsymbol{x}) = g(\boldsymbol{y}) = g(\boldsymbol{D}\boldsymbol{x} + \boldsymbol{u}). \tag{2.12}$$

It can be shown that a mathematically equivalent condition to Eq. (2.12) is

$$\det(\boldsymbol{D})\, F(\boldsymbol{D}\boldsymbol{k}) = e^{i\boldsymbol{k}\cdot\boldsymbol{u}} G(\boldsymbol{k}), \tag{2.13}$$

where $F(\boldsymbol{k})$ and $G(\boldsymbol{k})$ are the Fourier transforms of $f(\boldsymbol{x})$ and $g(\boldsymbol{x})$, respectively. The exponential term is removed from Eq. (2.13) by comparing the power spectra of F and G, and $\boldsymbol{D}$ is determined by applying a cross correlation:

$$c(\boldsymbol{D}) = \int |F(\boldsymbol{D}\boldsymbol{k})|\, |G(\boldsymbol{k})|\, d\boldsymbol{k}. \tag{2.14}$$

To find the vector $\boldsymbol{D}$ that maximizes the cross correlation c in Eq. (2.14), the equation is converted into a logarithmic frequency domain:

$$\tilde{c}[\log(\boldsymbol{D})] = \int \left|\tilde{F}[\log(\boldsymbol{D}) + \log(\boldsymbol{k})]\right| \left|\tilde{G}[\log(\boldsymbol{k})]\right| d\log(\boldsymbol{k}). \tag{2.15}$$

Eq. (2.15) can be solved by noting it is equivalent to solving Eq. (2.9) with Eq. (2.10). Thus, the normal stretch components contained in the tensor $\boldsymbol{D}$ are determined. The initial subvolume in the reference state $\boldsymbol{x}$ is stretched by pre-multiplying by the stretch tensor, $\boldsymbol{x}' = \boldsymbol{D}\boldsymbol{x}$, and a "stretch compensated" mapping is generated:

$$\boldsymbol{y} = \boldsymbol{x}' + \boldsymbol{u}. \tag{2.16}$$

Using the stretch compensated correlation, Eq. (2.12) is rewritten

$$f(\boldsymbol{x}) = g(\boldsymbol{x}' + \boldsymbol{u}). \tag{2.17}$$

The cross correlation is then written

$$c(\boldsymbol{u}) = \int f'(\boldsymbol{x}')\, g(\boldsymbol{x}' + \boldsymbol{u})\, d\boldsymbol{x}', \tag{2.18}$$

where f' satisfies $f'(\boldsymbol{x}') = f(\boldsymbol{x})$. Eq. (2.18) is then solved using Eq. (2.10) to give the displacement of the subvolume $\boldsymbol{u}$. The DVC approach is repeated for multiple subvolumes within the image stack, resulting in a full-field displacement measurement throughout the image volume.

2.3 3D Traction Computation in 2D Systems

Recently, 3D experimental approaches, some of which applied digital volume correlation, have shown cells exert both shear and normal tractions to a flat, 2D substrate [36, 37, 63]. The 3D approaches applied the fact that 3D experimental techniques capture displacements throughout the volume of the substrate [37, 63]. Therefore, direct differentiation of the displacements gives the strain tensor, and application of a constitutive law gives the stress tensor. Tractions can then be computed by using the Cauchy relation, $\boldsymbol{t} = \boldsymbol{\sigma} \cdot \boldsymbol{n}$, where $\boldsymbol{t}$ is the traction vector $\boldsymbol{\sigma}$ is the stress tensor at the surface of the substrate, and $\boldsymbol{n}$ is the outward unit normal vector from the substrate. In this direct approach, no mechanical solution is used, so mechanical equilibrium must be verified after tractions are computed. The advantages of the 3D experimental approaches are as follows:

1. tractions are computed directly, without the need for an ill-posed inverse solution (e.g., the inverse Boussinesq solution described in Chapter 1);

2. the traction computation is not sensitive to selecting the cell boundary as it is in the inverse solutions [11, 19]; and

3. tractions applied by the cells to the substrate are computed in *three dimensions*.

While 3D cell tractions have been measured previously, the 3D measurements have been limited to cells on a flat, 2D substrate. Most cell types live in a 3D environment, and it has previously been shown that cellular processes including adhesion [64] and morphology [65] differ between 2D and 3D cultures. Thus, there remains a need to develop new experimental techniques capable of measuring tractions applied by cells encapsulated within a 3D matrix.

2.4 Extending Traction Force Microscopy to 3D Systems

One previous study has reported measuring cell tractions within a fully 3D environment [66]. This study imaged cells and fluorescent particles encapsulated within an artificial polyethylene glycol (PEG) hydrogel. The authors developed a particle tracking algorithm to follow the 3D displacements of the particles, which served as a readout of the cell-induced displacements of the PEG gel. Maximum gel displacements near the cell body were found to be 5 μm, and the displacements decreased with increasing distance from the cell. Displacement and strain magnitudes far from the cell were measured to be in the range of 0–1 μm and 0–10%, respectively. These values of displacement and strain indicate the noise floor of the experimental technique. Tractions applied by the cells to the matrix were computed using an inverse method similar to the inverse Boussinesq solution that is used to compute tractions applied by cells to 2D substrates [11]. Since the interface between the cell body and the PEG gel was not flat as in 2D TFM experiments, the Boussinesq solution was not used to compute the Green's function relating displacements to tractions. Instead, a finite element approach was employed to approximate the Green's function at various points on the cell surface and to solve the inverse problem to compute tractions from the displacement data.

Despite the importance of a TFM technique capable of measuring tractions applied by cells in a 3D environment [66], several challenges remain. First, the use of particles can cause cell toxicity and analysis errors due to Brownian motion. Second, the use of a finite element

approximation to a Green's function requires a level of computational sophistication that is not available in most research groups that study biology and biological processes. While it is possible to use an analytical solution to solve the inverse problem of computing tractions from displacements, such analytical solutions are not significantly simpler and are subject to errors of greater than 30% [67]. Finally, this study used an artificial PEG gel with a pore size significantly smaller than a typical fibrous matrix that cells experience *in vivo*. While a different study measured the cell-induced displacements in a fibrous collagen matrix [68], this work used fluorescent particles to compute displacements. Also, the authors did not compute tractions applied by the cells, choosing instead to analyze only the strain energy induced in the matrix by the contracting cells. In this section, these challenges are addressed with the development of an alternative 3D TFM approach to the ones developed previously [66, 68].

2.4.1 Fibrous Extracellular Matrix

Instead of an artificial PEG gel, a natural fibrous matrix (Fig. 2.5) is chosen, since natural matrices have been shown to better mimic a tissue-like environment for the study of cellular processes [42]. The fibrous matrix selected here is fibrin, which has been shown to support cell growth, adhesion, migration and angiogenesis [69]. In addition, fibrin is a natural environment for fibroblast cells during wound healing [70]. Fibrin gels were prepared by mixing various concentrations of fibrinogen (Omrix Biopharmaceuticals, Israel) ranging from 1 to 10 mg/mL with a 20 U/mL thrombin solution (Omrix) at a 1:1 ratio. To image the fibrin matrices with confocal microscopy, the fibrinogen was fluorescently labeled before mixing with thrombin. The fluorescent dye, 546 Alexa Fluor coupled to an amine-reactive succinimidyl ester (Invitrogen Life Technologies, Grand Island, NY), was first mixed with fibrinogen solution in a 5:1 dye-to-protein molar ratio for 1 hour at room temperature and then filtered through a HiTrap desalting column packed with Sephadex G-25 resin (GE Healthcare, Milwaukee, WI) to separate the unreacted dye. The 546 Alexa Fluor dye was chosen to have a high fluorescence quantum yield ($\sim 80\%$) to minimize heat generation during imaging.

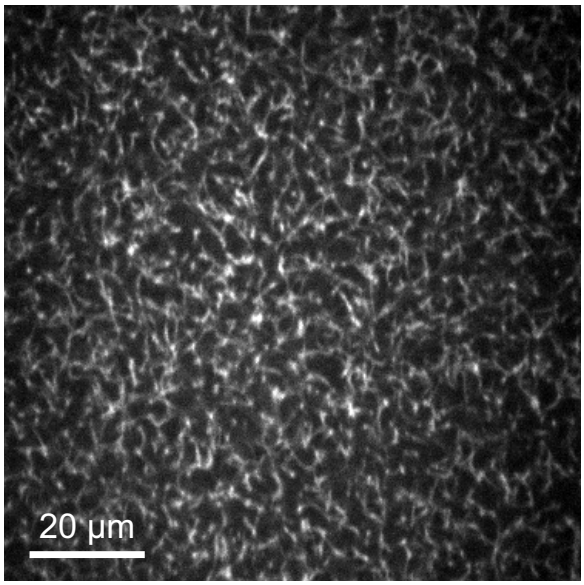

Figure 2.5: A typical image of a fluorescently labeled fibrin matrix. The fibrinogen concentration is ~ 3 mg/mL.

In some experiments, fluorescent particles were used as a speckle pattern for DVC. The particles, ranging in size from 0.5 μm to 1 μm and carboxylate modified (Invitrogen), were mixed with 20 μL of a 20 U/mL thrombin solution (Omrix) and vortexed for 1 minute to a final particle concentration of 0.05%. The thrombin suspension was placed on a #1.5 cover-slip in a 35 mm dish (MatTek, Ashland, MA), and mixed gently with the fibrinogen suspension.

The constitutive properties of fibrin gels (3 mg/mL of fluorescently labeled fibrinogen) were measured using a stress-controlled AR1000 rheometer (TA Instruments, New Castle, DE) equipped with 8-mm diameter aluminum parallel plates. The temperature was set to 37°C to match experiments with cells. Stress sweep tests were initially performed to evaluate the stress in the linear region appropriate for the frequency sweep tests. For the frequency sweeps, a stress of 4 Pa and a frequency range of 0.1–1 rad/s were applied. The fibrin gel was prepared on the rheometer itself while sandwiched between two sheets of sandpaper to avoid slipping. After 15 minutes of polymerization, warm PBS was added to cover the gel. Six different samples were included in the analysis. Mean $\pm$ standard deviation values of the shear elastic and loss moduli are shown in Fig. 2.6. The mean elastic component of the shear modulus was found

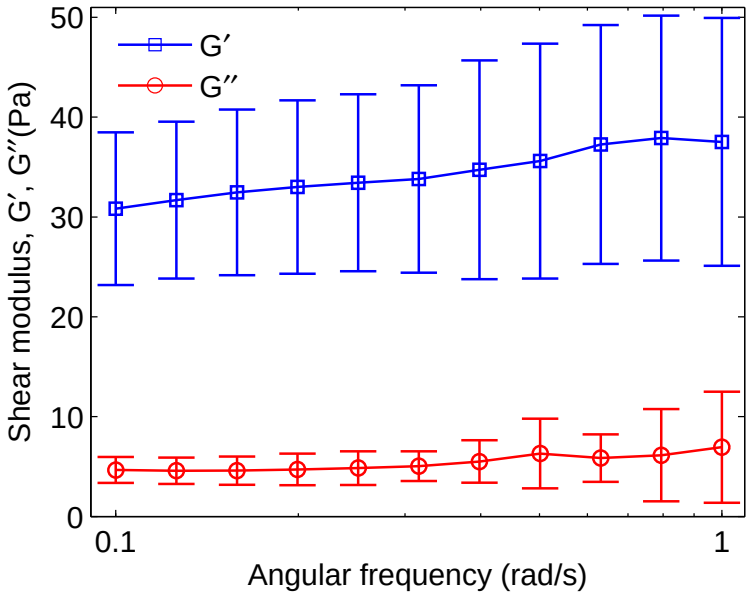

Figure 2.6: Mechanical properties of fibrin gels (3 mg/mL fibrinogen) are measured using a rheometer. Mean shear elastic (G') and loss (G'') moduli are approximately 33 Pa and 7 Pa, respectively, over a range of frequencies. Error bars are standard deviations. $n = 6$ specimens.

to be approximately 33 Pa over a range of frequencies. While the loss tangent, $\tan(\delta) = G'/G''$ is ~ 0.15, the time required for the cell to apply tractions to the matrix was on the order of minutes. Therefore, for the purposes of this study, viscoelastic effects were neglected, and the fibrin matrix was assumed to be isotropic and linearly elastic. Since the fibrin gels were mostly water, they were also assumed to be incompressible. More detailed constitutive models could be used in the future to improve the accuracy of the stress and traction measurements.

2.4.2 Displacement and Strain Computation

Digital volume correlation was used to measure displacements of the fibrin matrix. To generate volume stacks for DVC, fibrin matrices were made with either fluorescent particles (at a volume fraction of 0.05%) or labeled fibrin at concentrations of 0.75, 1.5, 3, and 4.5 mg/mL fibrinogen (Fig. 2.9), which are typically used for 3D experiments with cells [69]. A Swept Field confocal microscope mounted on a Ti stand (Nikon Instruments, Melville, NY) was used for confocal imaging. A $40\times$ NA 1.15 water immersion objective was used to match the index of

refraction between the immersion medium and the water-based fibrin gel. Other experiments performed with oil immersion objectives exhibited significantly reduced contrast than the water immersion lens. The Swept Field confocal scanner's array of 60 µm pinholes was used for most experiments. Minimal laser power was used to excite the specimens to prevent photobleaching, phototoxicity, and thermal heating. Images were captured with a QuantEM:512SC camera (Photometrics, Tucson, AZ). While the camera could capture images with frame rates of up to 30 fps, the frame rate was effectively reduced to ~ 2 fps by averaging together two 200 ms exposure images at each axial (z) location, resulting in an increased signal-to-noises ratio. Volume stacks were collected with an out-of-plane (z) step size of 0.4 µm. The microscope was housed in a custom-built chamber heated to $37°$C with an Air-Therm ATX heater (World Precision Instruments, Sarasota, FL) with a precision of $\pm 0.1°$C. CO_2 conditions were maintained at 5% by circulating 5% CO_2 blood gas within the chamber. All experiments were performed > 3 hours after placing the specimens in the heated chamber to allow for thermal equilibration of the heated enclosure.

Volume stacks were collected at an interval of 15–20 minutes for several hours. At the end of the experiments with cells, 85 µM blebbistatin (Sigma–Aldrich, St. Louis, MO), a myosin-II inhibitor [71], was added to the media to inhibit cellular contraction. Thus, the blebbistatin created a reference state for displacement computation in experiments with cells. Additional volume stacks were then collected for two hours after injecting blebbistatin and used as a reference for DVC.

Before computing displacements, the Lucy–Richardson deconvolution algorithm [72] was used to improve the resolution in the axial (z) direction. Displacements were computed using the DVC algorithm described earlier in this chapter with the compensation for subvolume stretches [59]. Subvolumes were chosen to contain $64 \times 64 \times 64$ voxels, and they overlapped to provide displacements on a periodic grid with 16 voxel spacing. Strain tensor components were computed numerically from the displacement data throughout the image volume by extending a previously reported technique [73] to three dimensions. All computations were performed

using MATLAB (The MathWorks, Inc., Natick, MA). A $3 \times 3 \times 3$ grid of points was fit to the 3D linear function,

$$\tilde{u}_{ijk} = ax_{ijk} + by_{ijk} + cz_{ijk} + d \tag{2.19}$$

where x_{ijk}, y_{ijk}, and z_{ijk} are the x, y, and z coordinates at position (i, j, k) within the 3×3×3 grid of points. The constants a, b, c, and d are the unknowns of the problem. The sum of squares error, defined as

$$\begin{aligned} S &= \sum_{ijk} \left(\tilde{u}_{ijk} - u_{ijk}\right)^2, \\ i, j, k &= 1, 2, 3 \end{aligned} \tag{2.20}$$

is minimized by setting derivatives equal to zero:

$$\begin{aligned} \frac{\partial S}{\partial a} &= 0, \\ \frac{\partial S}{\partial b} &= 0, \\ \frac{\partial S}{\partial c} &= 0, \\ \frac{\partial S}{\partial d} &= 0. \end{aligned} \tag{2.21}$$

Eq. (2.21) constitutes a set of four equations with four unknowns, so a solution to this linear system is straightforward. It can be shown that

$$\begin{aligned} \frac{\partial u}{\partial x} = a = \frac{\sum_{ijk}\left(x_{ijk}u_{ijk}\right)}{\sum_{ijk}\left(x_{ijk}\right)^2}, \\ \frac{\partial u}{\partial y} = b = \frac{\sum_{ijk}\left(y_{ijk}u_{ijk}\right)}{\sum_{ijk}\left(y_{ijk}\right)^2}, \\ \frac{\partial u}{\partial z} = c = \frac{\sum_{ijk}\left(z_{ijk}u_{ijk}\right)}{\sum_{ijk}\left(z_{ijk}\right)^2}. \end{aligned} \tag{2.22}$$

The computation is repeated for all three displacement components to give a set of nine dis-

placement gradient terms. The infinitesimal strain tensor is then computed according to

$$\varepsilon_{ij} = \frac{1}{2}\left(\frac{\partial u_i}{\partial x_j} + \frac{\partial u_j}{\partial x_i}\right). \tag{2.23}$$

2.4.3 Noise and Error

Control experiments were performed to assess the noise and accuracy of the DVC algorithm for volume stacks collected with the confocal microscope. Volume stacks of both labeled fibrin and 1 µm fluorescent particles were collected for analysis. Since blebbistatin was used in the experiments with cells, blebbistatin (85 µM) was injected into the media during control experiments immediately after the $t = 240$ min time point. The final volume stack after blebbistatin injection was used as a reference for DVC.

The mean displacements (Figs. 2.7a & 2.8a) measured by DVC are not constant over time, indicating the presence of global drift of the fibrin matrix. Additionally, the diagonal components of the strain tensor (Figs. 2.7b & 2.8b) are nonzero, revealing that the fibrin gels expand and contract during the experiment. The drift of the fibrin in the z direction (along the axis of the objective) is most likely caused by temperature fluctuations. In separate experiments (not shown here), changes in temperature of only $0.1°$C were found to cause drift in the z direction of several microns. In the experiments shown here, efforts are made to minimize temperature fluctuations (e.g., by equilibrating the heated enclosure to $37°$C for 3 hours before beginning experiments), but not all temperature fluctuations can be removed. The relative amount of drift decreases with time, indicating that an equilibration time longer than 3 hours may further reduce the effects of thermal drift. The jump in the z displacements in Figs. 2.7a and 2.8a after the $t = 240$ min time point is caused by injecting blebbistatin into the medium. While the blebbistatin is enclosed in the same heated chamber as the microscope before injecting, the temperature in the chamber varies slightly with location; thus, injecting the blebbistatin causes a slight change in the temperature of the fibrin matrix, resulting in thermal drift.

The in-plane (x–y) drift and strain of the matrix is larger for the labeled fibrin (Fig. 2.8)

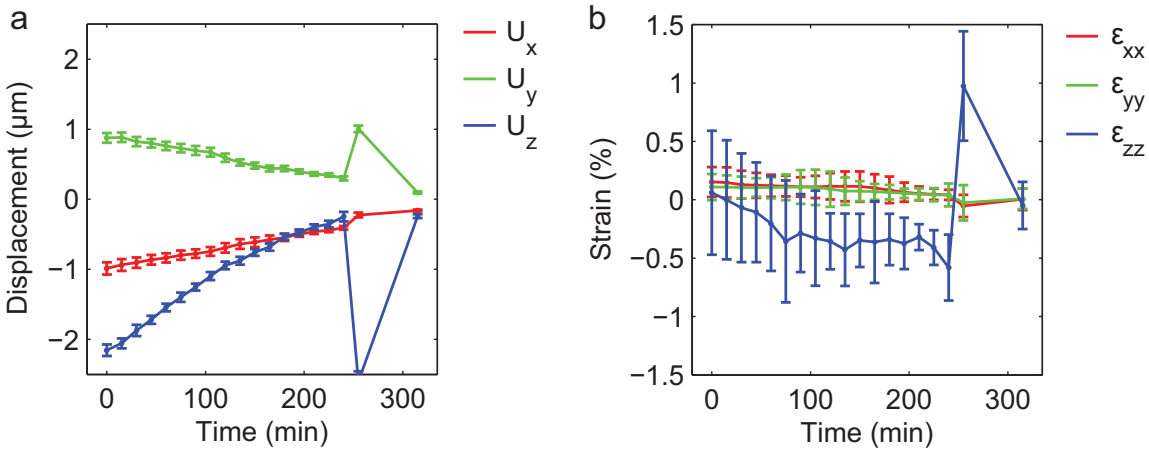

Figure 2.7: DVC is performed on volume stacks of 1 μm fluorescent particles encapsulated within a fibrin matrix. (a) Mean ± standard deviation of displacements. (b) Mean ± standard deviation of the normal strain components. The z direction is along the axis of the microscope objective.

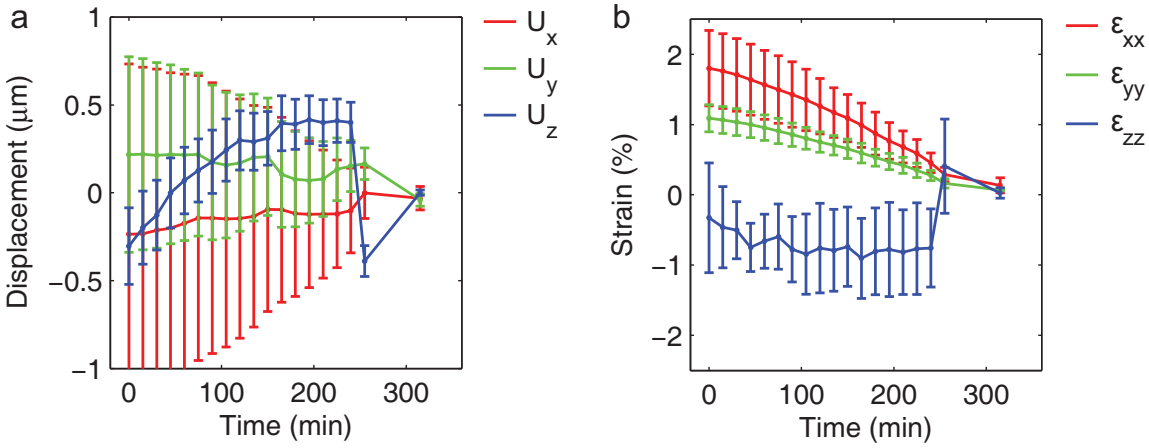

Figure 2.8: DVC is performed on volume stacks of labeled fibrin matrix (3 mg/mL fibrinogen). (a) Mean ± standard deviation of displacements. (b) Mean ± standard deviation of the normal strain components. The z direction is along the axis of the microscope objective.

than for the 1 μm particles (Fig. 2.7). Displacement standard deviations are also larger for the labeled fibrin, due to the larger strains. It was found that the labeled matrix expanded in the in-plane directions during imaging, possibly due to heating from the laser illumination. This expansion is not present in the volume stacks of the fluorescent particles, because the discrete particles have lower total fluorescence intensity than the labeled matrix, which has fluorescent molecules attached to every fiber. In all experiments, the laser intensity was minimized to reduce matrix expansion, but matrix expansion could not be completely eliminated.

The effects of gel contraction were compensated by computing average normal strains within the image stack. The displacements were then corrected so that normal strains in each volume stack equaled zero. Finally, drift in the experiment resulting from rigid body translation of the image volume was eliminated by translating the displacement data so that median displacements were zero. The complete displacement and strain results of various different fibrin matrix densities (Fig. 2.9) use these corrections.

As shown Fig. 2.9, after the corrections for swelling/contracting and drift, the mean displacements and strains fall to zero for all examined gel concentrations. System noise, described by the standard deviation of the displacement and strain data, is observed to depend on the contrast pattern used for DVC. A summary of typical noise levels is shown in Table 2.1 for the 1 μm particles and 3 mg/mL fibrinogen labeled matrix. Fluorescent particles, which provide the highest contrast, result in the lowest noise floor. DVC using labeled matrix fibers results in slightly higher noise levels. Of the labeled matrix correlations, the fibrinogen density of 3 mg/mL provides the lowest noise of < 0.25 μm and $< 0.75\%$ strain where an optimal speckle density for the DVC algorithm is achieved. There is generally more noise along the axial (z) direction than along the in-plane (x–y) directions due to the confocal microscope's decreased resolution in the axial direction. For all experimental conditions in Fig. 2.9, the system noise is found to be lower than reported in a previous study [66]. The improvement in noise observed here is likely due to the use of DVC, which correlates images over a volume instead of correlating pointwise as in particle tracking.

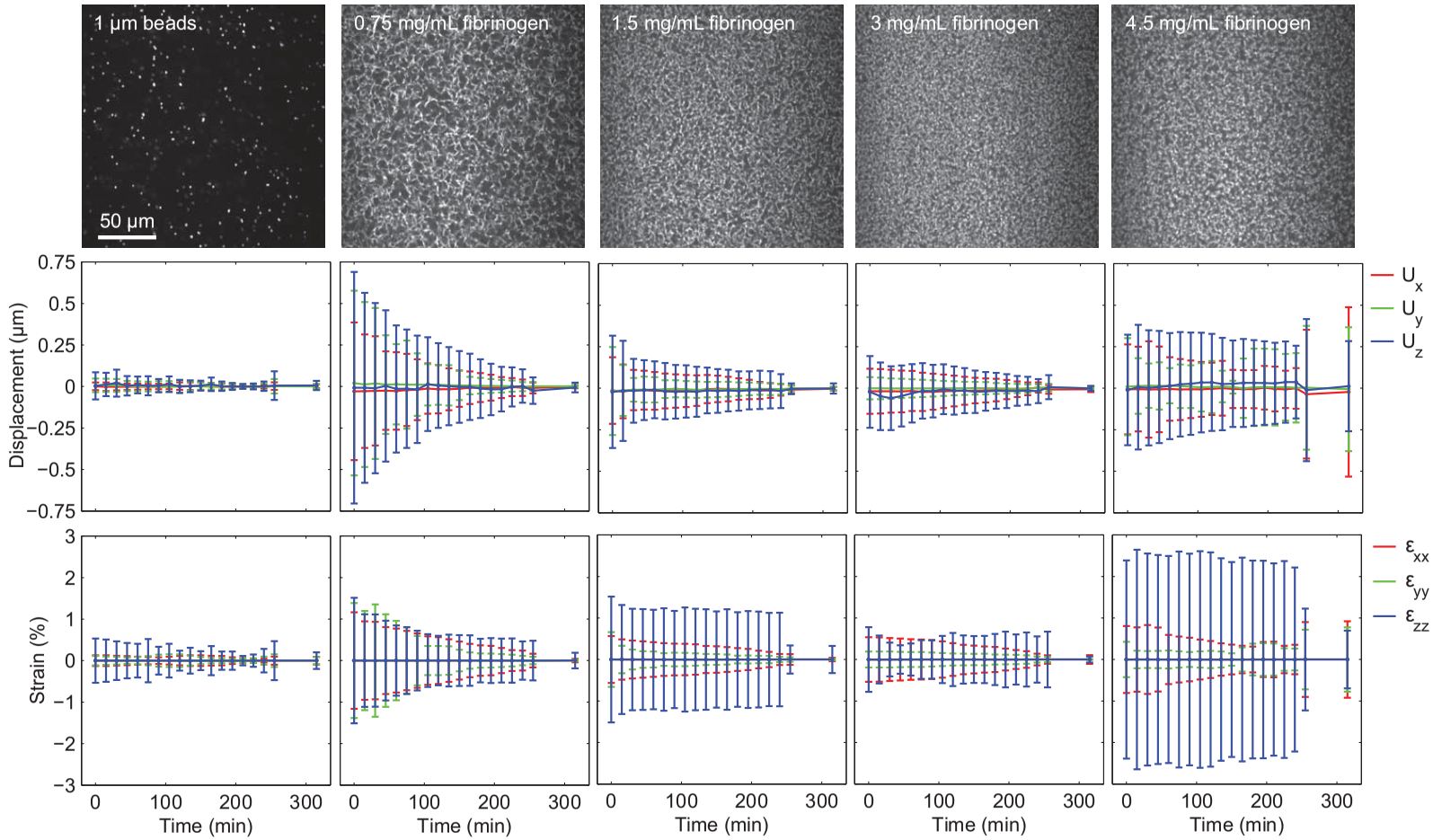

Figure 2.9: DVC is used to measure noise on gels with no cells. (Top row) 2D image slices of the volume stacks used in DVC show the contrast formed by either fluorescent particles suspended within the fibrin gel or fluorescently labeled fibrin. (Middle row) Mean ± standard deviation of displacements measured with DVC at all points in the 3D volume and at various time points. For all correlations, the reference stack is chosen to be the final stack collected after injecting blebbistatin. (Bottom row) Mean ± standard deviation of normal strain components computed by differentiating the displacements.

The accuracy of the DVC was assessed by applying artificial computational translations of 0–4 µm to the matrix image volumes and measuring these translations using DVC (Fig. 2.10). The DVC algorithm was found to be accurate in measuring displacements with typical errors shown in Table 2.2. Similar to the experiments to quantify the noise floor (Fig. 2.9), the 1 µm beads, which provided the best image contrast, resulted in the highest accuracy. Nevertheless, the DVC is found to be sufficiently accurate when using the labeled matrix fibers as a random contrast pattern.

When using DVC, both noise and accuracy depend on the size of the subvolume chosen. As mentioned previously, this work uses $64 \times 64 \times 64$ pixel subvolumes, resulting in the noise and accuracy given in Tables 2.1 and 2.2. Increasing the size of the subvolumes would provide more data for correlation, resulting in reduced noise. However, larger subvolumes reduce the spatial resolution of the measurement. Overlapping subvolumes are commonly used to increase spatial resolution, and an overlap of $1/4$ the size of the subvolume is chosen here, meaning that the $64 \times 64 \times 64$ pixel subvolumes are each centered on a 3D grid of points separated by 16 pixels for correlation. A typical pixel size is 0.4 µm, resulting in 3D displacement measurements every 6.4 µm. Finer spatial resolution is achievable by using smaller subvolumes during correlation, but decreasing the subvolumes below $64 \times 64 \times 64$ pixels was found to significantly increase the noise and error associated with the measurement.

If a finer spatial resolution were required for a particular measurement, one could use either a higher magnification objective with a corresponding reduction in field of view or a higher resolution camera with an increase in data acquisition and computation time. In addition, reducing the pixel size with a different objective lens or camera would not improve the axial resolution of the measurement, and therefore would likely not improve spatial resolution significantly. Alternatively, a higher density pattern could be employed for DVC. As observed in Fig. 2.9 the density of 1 µm particles is low, especially when compared to a typical speckle pattern for image correlation [52]. A higher particle density would offer better correlations with a smaller subset size but would limit the ability to image deeply into a specimen due to

Table 2.1: Typical noise floor for DVC displacement measurements using 1 µm particles and labeled fibrin (3 mg/mL fibrinogen). Noise is quantified by taking the mean standard deviation of the data in Fig. 2.9.

	U_x (µm)	U_y (µm)	U_z (µm)	ε_{xx} (%)	ε_{yy} (%)	ε_{zz} (%)
1 µm particles	0.02	0.03	0.13	0.10	0.09	0.34
Labeled fibrin	0.09	0.04	0.14	0.38	0.14	0.56

Table 2.2: Typical error of the DVC displacement measurements using 1 µm particles and labeled fibrin (3 mg/mL fibrinogen). Error is quantified by taking the mean standard deviation of the "cumulative" data in Fig. 2.10.

	U_x (µm)	U_y (µm)	U_z (µm)
1 µm particles	0.05	0.04	0.07
Labeled fibrin	0.17	0.06	0.22

increased alteration of the light paths by the increased particle density. Alternative imaging approaches like two photon microscopy could potentially improve image contrast with high particle densities with the caveat of two photon microscopy being a slower and more expensive imaging approach. Including particles of multiple colors could also increase the effective particle density with a minimal reduction in contrast with the trade-off that particles of multiple colors would require additional laser channels and increased imaging times. For particle free experiments that use labeled matrix for DVC, the density of the high contrast speckle pattern more closely matches a typical speckle pattern for image correlation. Instead of speckle density, the primary limitation on the labeled matrix is the contrast, which potentially could be improved with an alternative imaging approach like single point confocal or two photon microscopy. However, these approaches require longer acquisition times and expose the specimen to higher intensity light, which has the potential to cause thermal drift within the specimen as observed in Fig. 2.8. Considering the above tradeoffs between spatial resolution, image acquisition time, and cost, it was determined to use $64 \times 64 \times 64$ pixel subvolumes for all displacement computations using DVC in this study.

Since the displacement measurement errors in Table 2.2 contain both error and noise, these

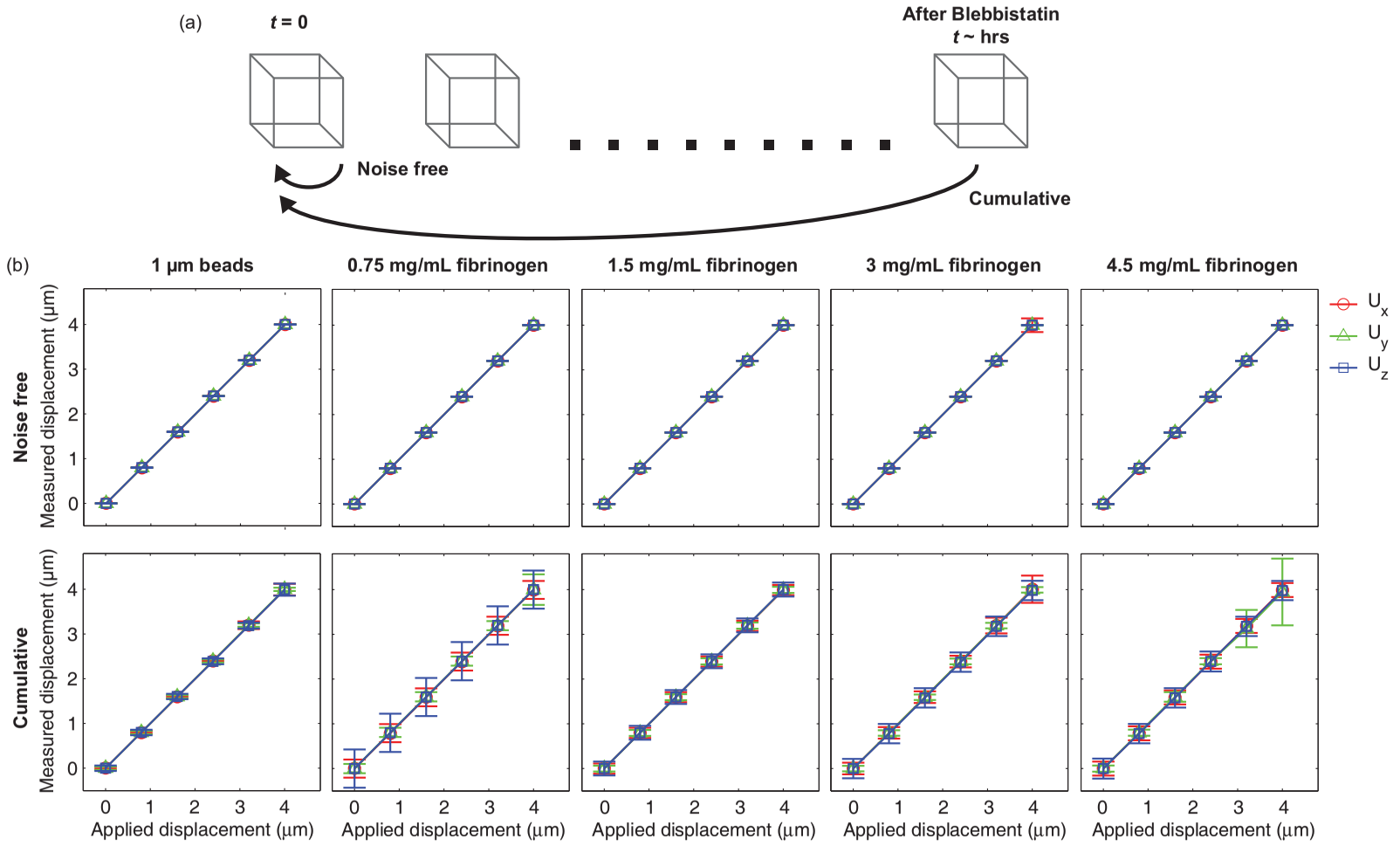

Figure 2.10: Artificial computational translations are applied to volume stacks to compute the accuracy of the method. (a) Two types of translations are applied. The noise free translations use the same volume stack as a reference and translated stack. The cumulative translations use the final stack collected after blebbistatin (as in Fig. 2.9) as the reference. (b) Mean ± standard deviation of the translated volume stacks computed with DVC.

errors are used to approximate the error in the strain computation. Upon substituting $n = 3$ (due to using a $3 \times 3 \times 3$ grid of points for strain computation) into Eqs. (2.22), the displacement gradient terms are simplified. As an example, the displacement gradient $\partial u/\partial x$ becomes

$$\frac{\partial u}{\partial x} = \frac{\sum_{i,j,k=-1}^{1} \left(x_{ijk} u_{ijk}\right)}{\sum_{i,j,k=-1}^{1} \left(x_{ijk}\right)^2}. \tag{2.24}$$

For a $3 \times 3 \times 3$ grid with a spatial resolution given by r_s, Eq. (2.24) simplifies to

$$\frac{\partial u}{\partial x} = \sum_{i,j,k=-1}^{1} \frac{1}{18 r_s^2} \left(x_{ijk} u_{ijk}\right). \tag{2.25}$$

Since all displacement measurements are uncorrelated from one position to another (i.e., the DVC algorithm computes displacements at each position independently), the error in strain is estimated according to the standard formula for propagation of uncertainty,

$$\sigma_\varepsilon^2 = \left(\frac{\partial \varepsilon}{\partial u_{ijk}}\right)^2 \sigma_u^2, \tag{2.26}$$

where $\varepsilon = \partial u/\partial x$ is the displacement gradient, σ_ε^2 is the variance of the error in strain, and σ_u^2 is the variance of the error in the displacement measurement. Since

$$\frac{\partial \varepsilon}{\partial u_{ijk}} = \frac{1}{18 r_s^2} x_{ijk}, \tag{2.27}$$

Eq. (2.26) becomes

$$\begin{aligned} \sigma_\varepsilon^2 &= \sum_{ijk} \left(\frac{1}{18 r_s^2} x_{ijk}\right)^2 \sigma_u^2, \\ &= \sum_{ijk} \frac{1}{18^2 r_s^4} x_{ijk}^2 \sigma_u^2. \end{aligned} \tag{2.28}$$

When $i = 0$, $x_{ijk} = 0$, but for all other values of i, j, k, $x_{ijk}^2 = r_s^2$. Thus, Eq. (2.28) simplifies to

$$\sigma_\varepsilon^2 = \frac{\sigma_u^2}{18 r_s^2}. \tag{2.29}$$

Table 2.3: Error in the strain computation, estimated by applying Eq. (2.30) to the data in Table 2.2.

	ε_{xx} (%)	ε_{yy} (%)	ε_{zz} (%)
1 µm particles	0.19	0.13	0.28
Labeled fibrin	0.61	0.23	0.80

Thus, the standard deviations in error in strain tensor components σ_ε can be related to the standard deviations in error of the displacement measurements through σ_u

$$\sigma_\varepsilon = \frac{\sigma_u}{3\sqrt{2}r_s}. \tag{2.30}$$

To verify this result, Eq. (2.30) is applied to the displacement noise in Table 2.1 and the resulting strains agree fairly well with the computed strain noise floor reported in Table 2.1. Eq. (2.30) is finally applied to the typical displacement measurement errors reported in Table 2.2, and the results are given in Table 2.3. In summary, typical errors in displacement measurement are ~ 0.1 µm when using fluorescent particles and ~ 0.2 µm when using labeled matrix. Typical errors in strain measurement are $\sim 0.3\%$ when using particles and $\sim 0.6\%$ when using labeled fibrin.

2.4.4 Preparation of Cell–Matrix Constructs

To measure cell-induced displacements and cell tractions, fibrin gels (3 mg/mL fibrinogen) were prepared with embedded cells. NIH 3T3 fibroblast cells (passages 10–20) were cultured in DMEM medium supplemented with 10% fetal bovine serum and $1\times$ non-essential amino acids in a 37°C humid incubator. The fibroblasts stably expressed GFP attached to actin, which allowed for direct visualization of the actin stress fibers within the cell. To seed the cells within the fibrin gels, the cells were mixed with the thrombin solution before mixing with fibrinogen. Generally, cell densities of around 3000 cells in 20 µL fibrin gel were used. The resulting fibrin gels were placed in an incubator for 15 minutes to fully polymerize, after which

warm cell culture medium was added to cover the gel.

2.4.5 Cell-Induced Displacements and Tractions

Volume stacks of fluorescently labeled fibrin matrix and single cells were collected every 15–30 minutes for a period of several hours using the confocal microscope (Fig. 2.11a). 85 µM blebbistatin was injected into the cell medium to inhibit cell contractile activity, allowing the fibrin matrix to recover to an unstressed state. It was found that the blebbistatin normally took full effect after $\sim$ 2 hours. Real time cumulative matrix displacements were computed by using the unstressed matrix state ($\sim$ 2 hours after addition of blebbistatin) as a reference for DVC (Fig. 2.11b). Drift and swelling/contracting of the matrix was corrected as described previously. Displacement values under a threshold of 0.08 µm were set to zero. The threshold value was determined from the noise floor for the 3 mg/mL fibrinogen labeled matrix (Fig. 2.9). Displacements were differentiated in three dimensions as described earlier in this chapter to compute the strain tensor ε. The stress tensor $\boldsymbol{\sigma}$ was computed by applying the incompressible, linear, elastic Hooke's Law, $\boldsymbol{\sigma} = 2\mu\varepsilon$. Traction vectors on the surface of the cell were computed directly from the stress tensor using the Cauchy relation $\boldsymbol{t} = \boldsymbol{\sigma} \cdot \boldsymbol{n}$ where $\boldsymbol{n}$ is the outward unit normal vector from the cell surface. The outward unit normal was computed in MATLAB by creating a 3D isosurface plot of the cell and computing the outward direction at various positions along the isosurface. Stress tensor components on the cell isosurface were computed using a linear interpolation.

This 3D TFM technique is capable of simultaneously observing matrix fibers (Fig. 2.11a), measuring cell-induced displacements (Fig. 2.11b), and computing cell tractions (Fig. 2.11c). Cells encapsulated in fibrin gels exert forces against their surrounding matrix that leave a hallmark of local matrix deformation (Fig. 2.11a). Such matrix deformations are characterized by increased fiber density (brighter fluorescence) and aligned fibers (Fig. 2.11a box i) as compared to areas distal to the cell, which exhibit a random arrangement of fibers (Fig. 2.11a box ii). The largest matrix displacements of 3–4 µm are observed near the tips of thin extensions of

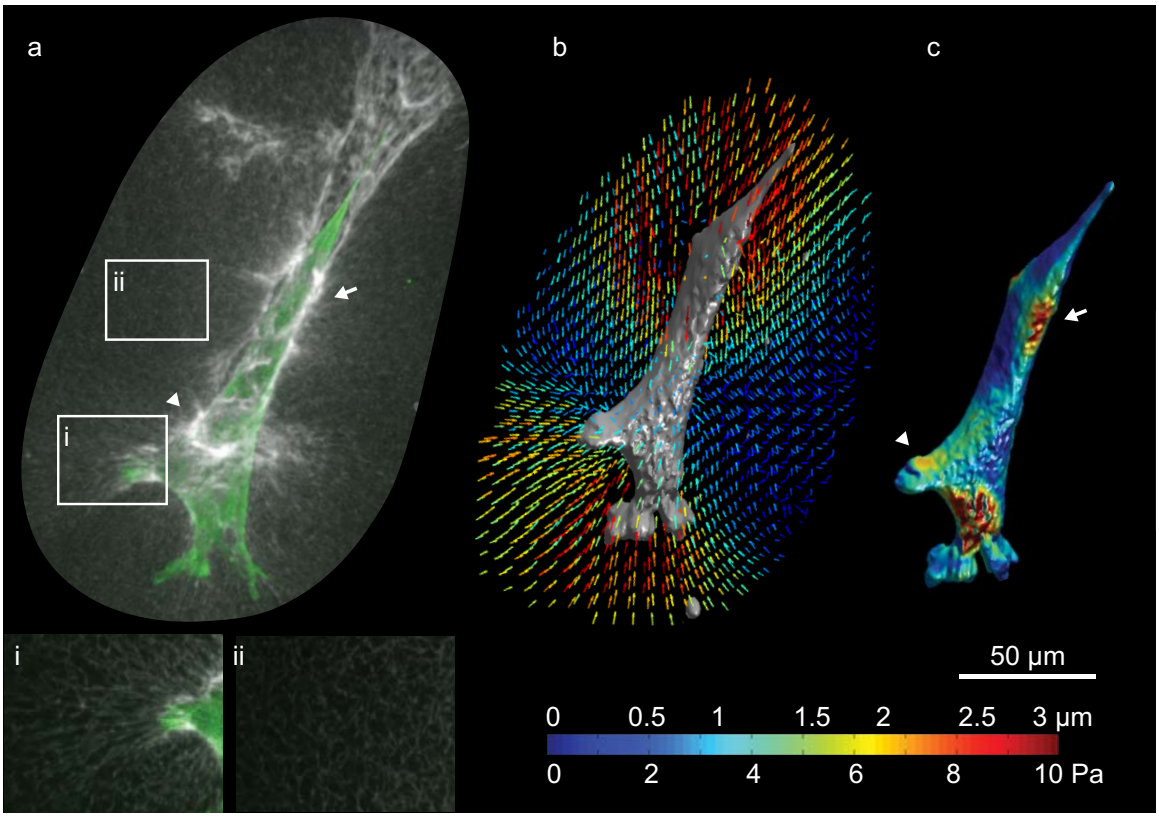

Figure 2.11: (a) A fibroblast cell (actin, green) applies tractions and rearranges the matrix (gray) at the tips of slender extensions. Matrix alignment toward the cell is present near these extensions (i) but not in regions away from the cell (ii). (b) The cell applies inward matrix displacements of up to 3 µm primarily near the extensions' tips. (c) The contour plot of tractions applied by the cell to the matrix indicates the cell exerts tractions at localized regions on the cell surface that correspond to areas of fiber compaction (arrows).

the cell (Fig. 2.11b). The displacements fall to negligible levels in all directions away from the cell. Cells embedded in a 3D fibrin matrix exert tractions of up to 10 Pa primarily at peripheral areas of cellular extensions at locations behind the extensions' tips (Fig. 2.11c). These sites are coupled to ring-like structures of compacted fibers of higher fluorescence intensity (Fig. 2.11a,c arrows).

2.5 Discussion

This chapter describes the development of a 3D traction measurement approach suitable to cells embedded in a biologically relevant fibrous matrix. The 3D TFM technique developed

here uses a time-lapse imaging approach, resulting in the capability to dynamically monitor cell tractions and matrix deformations over time. The time-lapse control experiments described in this chapter show that the experimental noise in measuring displacements and strains is relatively constant in real time (Fig. 2.9), indicating that this 3D TFM approach is applicable to dynamic, time-dependent experiments. While cell-induced matrix displacements and cell tractions are only shown for a single time point in this chapter (Fig. 2.11), Chapters 3 and 4 apply the 3D TFM technique to cell division and invasion, respectively. These dynamic cellular processes require not only time-lapse microscopy but also sufficiently high speed data acquisition to capture the biological processes of interest.

The 3D TFM approach described here uses a high speed confocal scanner with an array of pinholes that increases image acquisition speed by a factor of 2–10. The array of pinholes also distributes the excitation laser light over an area instead of focusing the light on a single point as is done with a typical point scanning confocal system. The reduced power of the illumination light associated with the light distributed over an area exposes the cells to lower light intensity and therefore results in reduced phototoxicity. Previous approaches to measure 3D tractions on a flat substrate using a point scanning confocal microscope have reported collecting volume stacks every ~ 30 minutes [37, 63], and increased imaging rates were likely unfeasible due to phototoxicity. Thus, in addition to higher possible image acquisition rates, use of a confocal scanner with an array of pinholes maintains cell viability during imaging.

The primary limitation of the approach described here is in the assumption that the fibrin matrix behaves as a homogeneous, isotropic, linear, elastic material to compute the stress tensor within the matrix. The direct imaging of matrix fibers shows that some cell-induced matrix deformation is highly localized with anisotropic alignment of matrix fibers (Fig. 2.11a, arrows). While some of the localized deformation is recoverable elastic deformation, plasticity is likely to be present in the fibrin matrix at the large strains observed in the experiments ($\sim 10\%$). Indeed, a stress–relaxation experiment to quantify the the constitutive properties of the fibrin matrix (Fig. 2.12) reveals that the stress within the matrix relaxes to nearly

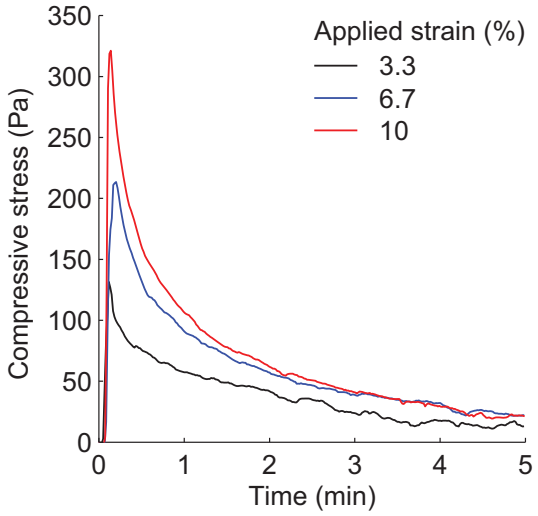

Figure 2.12: A stress–relaxation experiment is performed by placing a cylindrical fibrin gel specimen (height: 3.04 mm; diameter: 6.36 mm; 7.5 mg/mL fibrinogen) under compressive strain and monitoring the change in compressive stress over time using a previously described loading apparatus [59]. Stress–relaxation data is shown for compressive strains of 3.3%, 6.7% and 10%.

zero within ~ 5 minutes after loading. This result indicates that for strains of up to $\sim 10\%$, viscoelastic effects occur over a time scale of minutes. Furthermore, the significant relaxation of stress indicates that the fibrin matrix is better described as viscoplastic rather than linearly elastic. While more work is required to develop a viscoplastic constitutive model for the fibrin matrix, such detailed constitutive modeling is beyond the scope of this thesis. Thus, tractions are computed here using the linearly elastic approximation.

While previous techniques have reported measuring cell-induced strain energy in a 3D collagen gel [68] and cell tractions in an artificial PEG gel [66], these studies used techniques that were restricted to measuring displacements by imaging particles. Visualizing particles does not yield detail of the cell-induced structural rearrangement of surrounding fibers. Such details are integral to revealing the local physical variations of the ECM and allow for more thorough analysis of cell-matrix interactions. For example, visualizing the fibrillar ECM provides direct insights into mechanisms of matrix remodeling events such as matrix deposition, degradation, and deformation, all of which occur *in vivo* [74]. Additionally, highly remodeled ECM zones of *in vitro* collagen gels have been shown to provide a pathway for cell motility,

prompting the transition toward collective cancer cell invasion [74].

Thus, imaging of matrix fibers while simultaneously quantifying tractions is required to fully capture how cells interact with the extracellular environment. While measurements of matrix displacements have previously been reported by imaging fibers in gels without cells [75], and cell contractile activity has been observed by direct imaging of matrix fibers [76], no studies have yet combined these two approaches into one complete technique. Thus, the live imaging of fibrillar matrices coupled with cell traction force measurements described here represents a step forward in TFM by providing "2-in-1" structural-mechanical information in *three dimensions*. It is anticipated that this technique will provide new insights regarding how the ECM mechanically signals the cell to control mechanotransduction and cell fate. In addition, this technique can be readily extended to different imaging approaches such as multiphoton microscopy, label-free confocal reflection microscopy, and imaging in live organisms by using images of the native ECM. The following sections of this thesis describe the use of this technique for analyzing the mechanics of cell division, cell invasion, and cell mechanosensing in three dimensions.

Chapter 3

Cell Division in Three-Dimensional Fibrous Matrices*

3.1 Abstract

The role of the extracellular matrix in regulating cell division is not well understood. Here we report simultaneous observation of cell division dynamics and traction force microscopy for cells embedded in fibrous three-dimensional (3D) matrices. We show that during cell division in a 3D fibrin matrix, fibroblasts remain anchored to the matrix at the tips of persistent thin protrusions while the cell body rounds and disengages from the matrix. The cells apply tensile forces that deform the matrix locally around the protrusions, and finally divide along the protrusion axis. The results illustrate that cell division in three dimensions is regulated by forces exerted by highly polarized adhesive structures that are not observed in cells dividing on two-dimensional (2D) substrates.

3.2 Introduction

Cells orchestrate striking changes in their interaction with the extracellular matrix as they divide. In 2D cultures, when a cell rounds to divide, it maintains short adhesion fibers that

*This chapter is written as a stand-alone manuscript to be submitted for publication. The text and figures in this chapter are written in collaboration with A. Lesman, G. Ravichandran, and D. Tirrell.

link the cell body to the substratum. The adhesion fibers bear forces that direct the orientation of the mitotic spindle [77, 78] and assist the daughter cells to respread and separate [79]. *In vivo*, mitotic cells in the developing zebrafish neural tube form daughter cells of defined fates that depend on their connection to the extracellular surroundings [80]. Proper regulation of adhesion to the extracellular matrix is imperative for controlled cell division a process that is central to tissue morphogenesis and homeostasis.

Previous studies of cell division in culture have used hard 2D substrates. However, various cellular functions, including adhesion, differ greatly for cells embedded in 3D matrices [64, 81]. In 3D fibrous matrices, cells spread along discrete fibers, rather than on a continuous flat substrate. Fibroblast cells on 2D surfaces develop spread, sheet-like morphologies with numerous focal adhesions, rather than the elongated shapes characteristic of cells embedded in 3D matrices *in vivo* [64]. Even the way cells probe their surroundings and migrate depends strongly on the dimensionality and geometry of the matrix [81]. The aim of this work is to elucidate cell–matrix interactions during mitosis in a model extracellular matrix system that mimics the essential features of many tissue environments: soft, fibrous and 3D.

3.3 Results and Discussion

To capture the dynamics of cell division in 3D environments, we co-encapsulated fibroblasts and endothelial cells in fibrin gels, which have been shown to support cell growth, adhesion, migration and angiogenesis [69]. Endothelial cells were included to promote fibroblast proliferation [82]. The fibrin gels used in this study exhibited fibrillar morphologies and shear moduli characteristic of compliant tissues such as mammary gland and brain (typically about 100 Pa) [3, 83]. We used time-lapse confocal microscopy to collect stacks of images of dividing fibroblasts that expressed an actin–GFP fusion protein (actin–GFP) throughout the cell division cycle (Fig. 3.1a, Fig. 3.2).

Before division begins, the cell has a visible nucleus and is spread with well-developed ex-

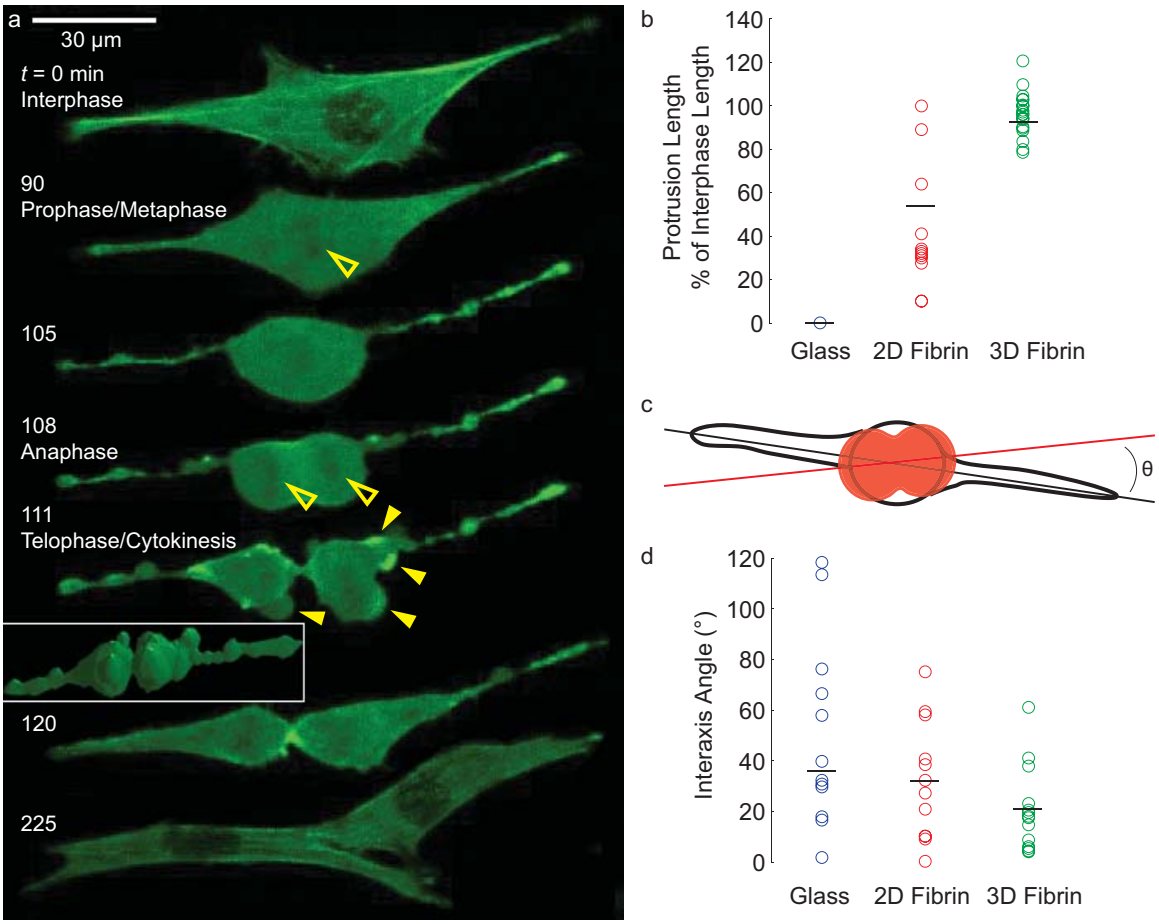

Figure 3.1: Time-lapse confocal microscopy reveals cellular morphology and cell division kinematics and orientation. (a) A single well-spread actin–GFP fibroblast cell embedded in a 3D fibrin gel rounds into a sphere before cytokinesis ($t = 0$–105 min). After the nuclear membrane breaks down, the nuclear material can be seen as dark spots at the center of the cell (hollow yellow arrows). After rounding, cytokinesis occurs within minutes ($t = 108$–111 min). Long, thin protrusions are apparent throughout the division process, and blebbing occurs during late cytokinesis ($t = 111$ min, yellow solid arrows; inset box shows a 3D rendering). After division ($t = 120$–225 min) the daughter cells respread along the long axis of the protrusions. 3D renderings are shown in Fig. 3.2. (b) Protrusion length measured 5 min before cytokinesis reveals maintenance of the interphase length for cells embedded in 3D gels. (c) 3D renderings were used to calculate the angle θ between the direction of the protrusions during cell rounding (black line) and the division axis during anaphase (red line). (d) Protrusion direction and division orientation are well correlated for cells embedded in 3D matrices ($n = 20$), in contrast to the 2D cases (glass; $n = 14$, and 2D fibrin; $n = 12$).

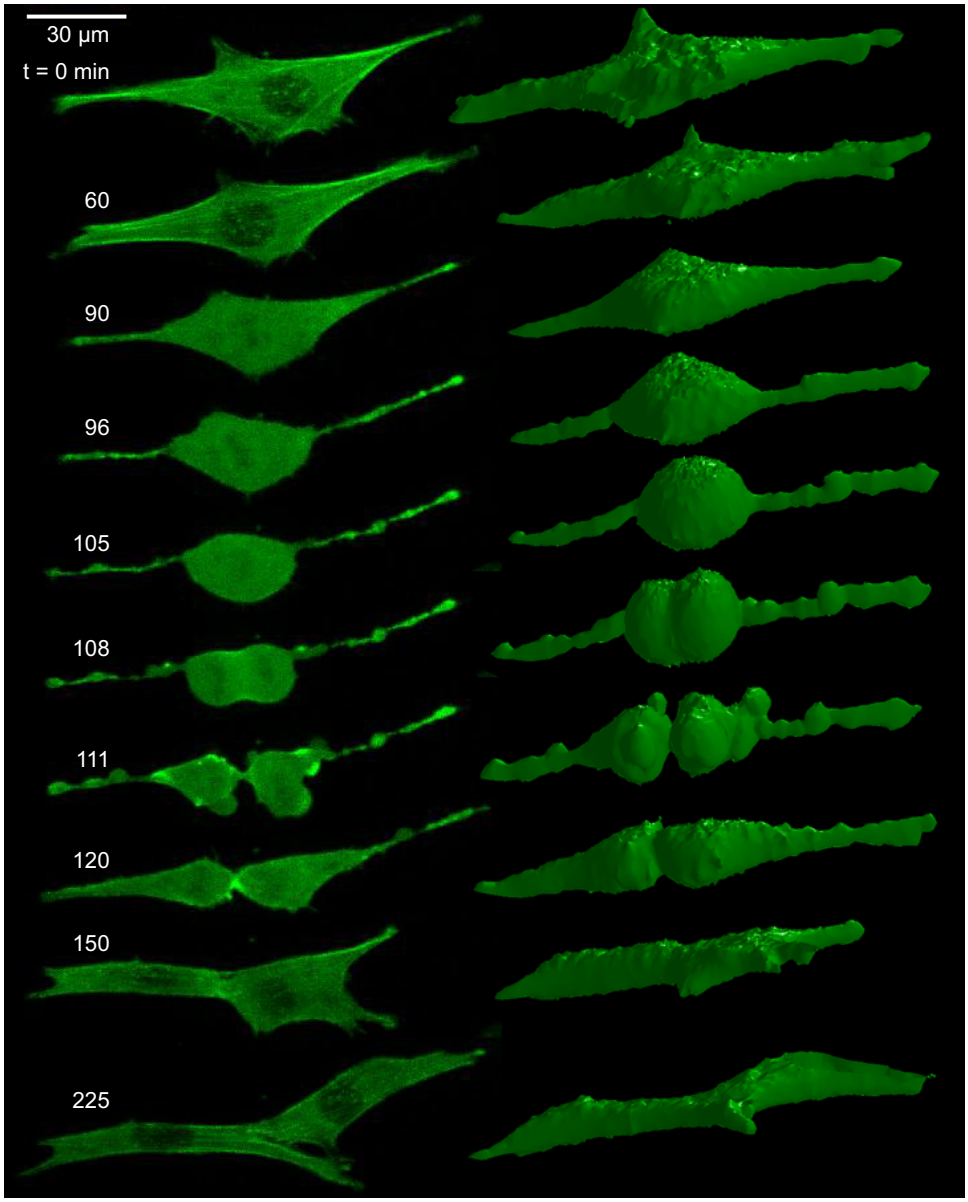

Figure 3.2: Maximum intensity projections and 3D renderings of the a dividing fibroblast shown in Fig. 3.1.

tensions (interphase, Fig. 3.1a, $t = 0$ min). The cell begins dividing by adopting a spherical shape. At this stage, the characteristic extensions at the poles of the cell body become thinner but remain intact, the nuclear structure starts to disassemble, and the chromosomes condense (prophase/metaphase, Fig. 3.1a, $t = 90$–105 min). The sphere then starts to divide, the chromosomes separate, a cleavage furrow is assembled (anaphase, Fig. 3.1a, $t = 108$ min), and cytokinesis occurs with the formation of blebs (telophase/cytokinesis, Fig. 3.1a, $t = 111$ min). Finally, the daughter cells reassemble their nuclei and spread along the long axis of the protrusions (Fig. 3.1a, $t = 225$ min, Fig. 3.2). Complete separation between daughter cells was observed to require minutes to hours (Fig. 3.1a, $t = 225$ min, Fig. 3.3).

The most striking of these observations is the fact that dividing cells maintain long, thin protrusions (referred to as "mitotic protrusions" hereinafter) tethered to the matrix throughout mitosis (Fig. 3.1a, Fig. 3.2). The mitotic protrusions are substantially larger, fewer in number and more polarized than retraction fibers, the adhesion structures observed in 2D systems [77, 78]. They show diverse morphologies, spanning ~ 100 µm in length and ~ 2 µm in width (Fig. 3.4). Similar long cellular processes have been associated with asymmetric cell division in the neural tube of the developing zebrafish [80]. When we cultured cells on glass dishes or on top of thick fibrin gels, we observed complete or partial retraction of the protrusions (Fig. 3.5); there was no evidence of protrusions for cells on glass substrates entering cytokinesis (Fig. 3.1b). For cells encapsulated in 3D fibrin gels, we found strong correlation ($p < 0.001\%$, Kolmogorov-Smirnov test, see methods for more details) between the orientation of the cell division axis (determined at anaphase, Fig. 3.1c) and that of the mitotic protrusions (determined at cell rounding, Fig. 3.1c), with 80% of divisions occurring within an angle smaller than $25°$ (Fig. 3.1d). After cytokinesis, the daughter cells respread along the direction of the protrusions (Fig. 3.1a, $t = 225$ min), even in events where the division and protrusion axes were misaligned (angle $> 40°$, Fig. 3.3). These observations suggest that cells embedded in 3D matrices maintain strong adhesive cues from interphase in the form of long protrusions that determine the orientation of division.

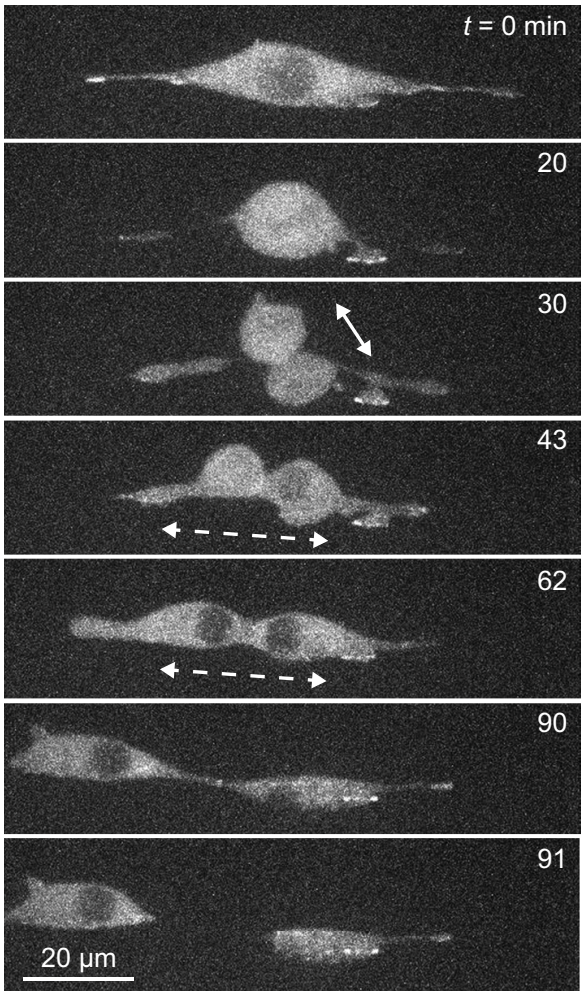

Figure 3.3: The daughter cells respread and separate from one another along the long axis of the mitotic protrusions. Even in events where the division axis ($t = 30$ min, white arrow) was not correlated with the direction of the protrusions (dotted white arrow), the daughter cells shifted their orientation and spread along the protrusions ($t = 43$–62 min).

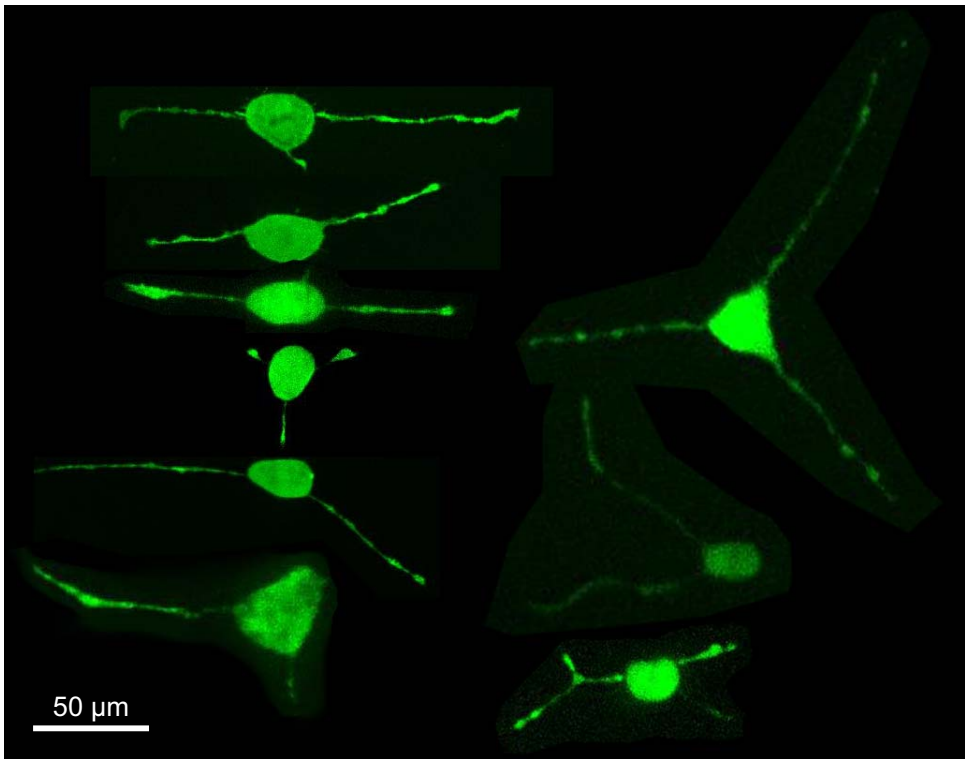

Figure 3.4: Dividing 3T3 fibroblasts consistently form thin long protrusions while dividing in a 3D fibrin matrix. Each cell is in the spherical stage just before cytokinesis.

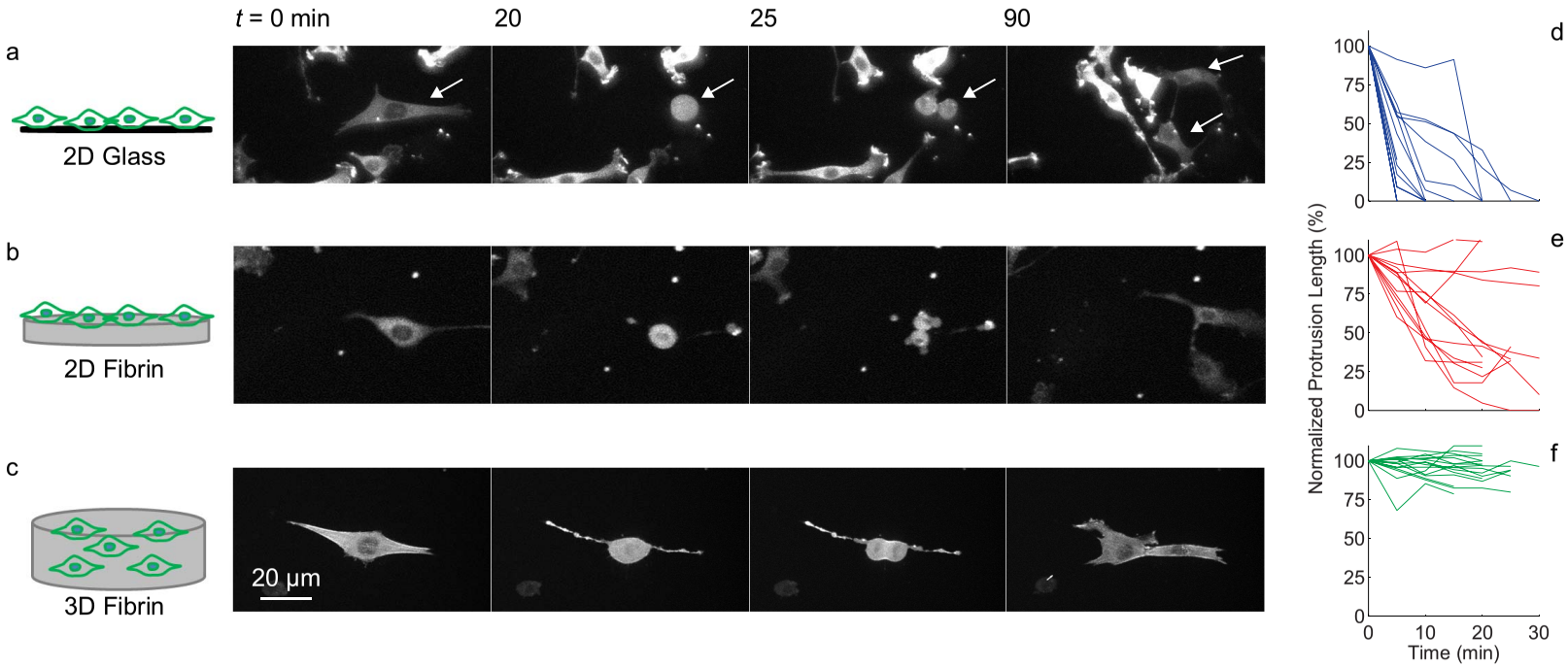

Figure 3.5: Comparison of the division cycle of cells cultured on 2D glass dishes (a), on top of 200 µm-thick fibrin gels (b) or embedded in 3D fibrin gels (c). Quantification of protrusion length over the course of the cell rounding phase demonstrates that dividing cells on glass substrates completely and rapidly retract their protrusions (d) and cells on top of 2D fibrin gels show gradual and partial retraction (e). In contrast, cells in 3D fibrin gels maintain their protrusions for the entire division cycle (f).

To explore further the role of matrix interaction and mitotic protrusions in cell division, we used 3D traction force microscopy [37, 63] to measure cell-induced matrix displacements throughout the cell division cycle. Traction forces exerted by retraction fibers have been shown to control the orientation of the mitotic axis in two dimensions [78], and to assist the daughter cells to respread and separate [79]. Although Burton and Taylor have reported pioneering measurements of traction forces generated during cell division in 2D systems [79], we believe that the experiments described here constitute the first quantitative study of cell-induced matrix displacements during division in three dimensions. Briefly, we co-encapsulated cells and 0.5 μm fluorescent particles in fibrin gels (Fig. 3.6a), acquired confocal volume stacks of the cells and the particles surrounding them, and computed matrix displacements with a digital volume correlation (DVC) algorithm [59]. The DVC algorithm was used to correlate all volume stacks to a reference time point acquired after injection of blebbistatin. Treatment with blebbistatin inhibited the contractile activity of the cell [71] and allowed imaging of a stress-free reference state of the gel (Fig. 3.6).

DVC analysis shows that as cells round up, matrix displacements adjacent to the cell body decrease to nearly undetectable values (Fig. 3.6b). These findings are consistent with earlier observations of reduced 2D traction forces near the cell body just prior to cytokinesis [79]. Cell-induced displacements do not return to the region surrounding the cell body until the daughter cells attempt complete separation (abscission) (Fig. 3.7). In contrast, during mitotic cell rounding, large matrix displacements were observed at the tips of the mitotic protrusions that anchor the cell to the matrix (Fig. 3.6b, $t = 0$ arrow heads). Following cytokinesis, as the daughter cells begin to respread into the matrix and attempt complete separation, they apply large tractions mainly at the leading edges of newly developing extensions (Fig. 3.6b, $t = 210$ min, Fig. 3.7). The surge in total matrix displacements after cytokinesis (Fig. 3.6c) suggests that traction forces contribute to respreading and separation of the daughter cells. The results also suggest that tensile forces transmitted from the matrix through the mitotic protrusions act as polarizing signals on the cell cortex to align the division axis with the direction of matrix

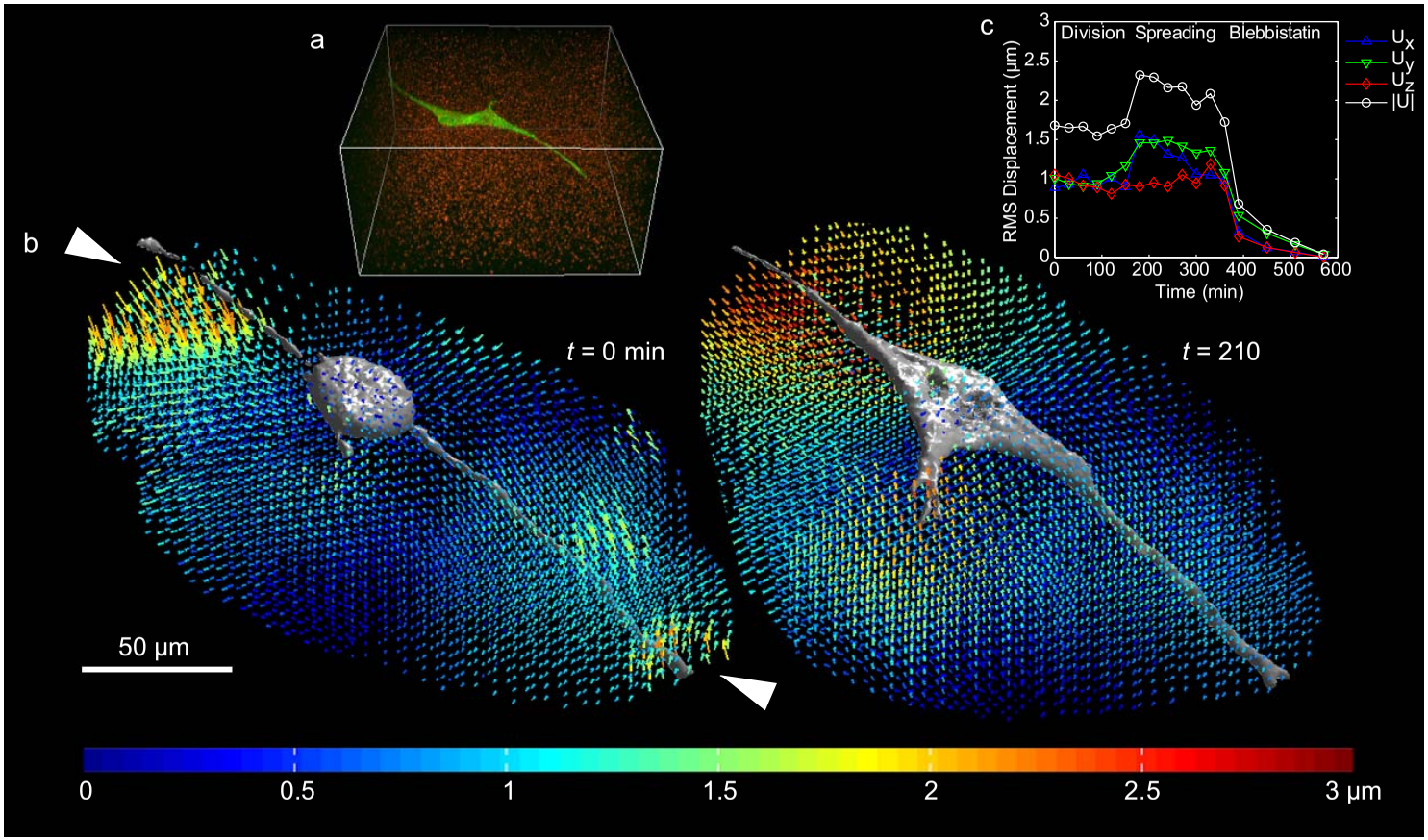

Figure 3.6: 3D traction force microscopy captures the dynamics of cell-induced matrix displacements during division and respreading. (a) 3D view of the imaging volume of a dividing cell and fluorescent particles. (b) Quiver plots of 3D matrix displacements show that the cell applies tractions to the matrix primarily at the tips of its long protrusions during division (white solid arrows). Approximately 3 hours after division the daughter cells apply larger displacements as they respread and extend into the matrix. (c) The root-mean-square matrix displacements increase shortly after division and then decrease to zero after blebbistatin is injected into the medium (at $t = 360$ min).

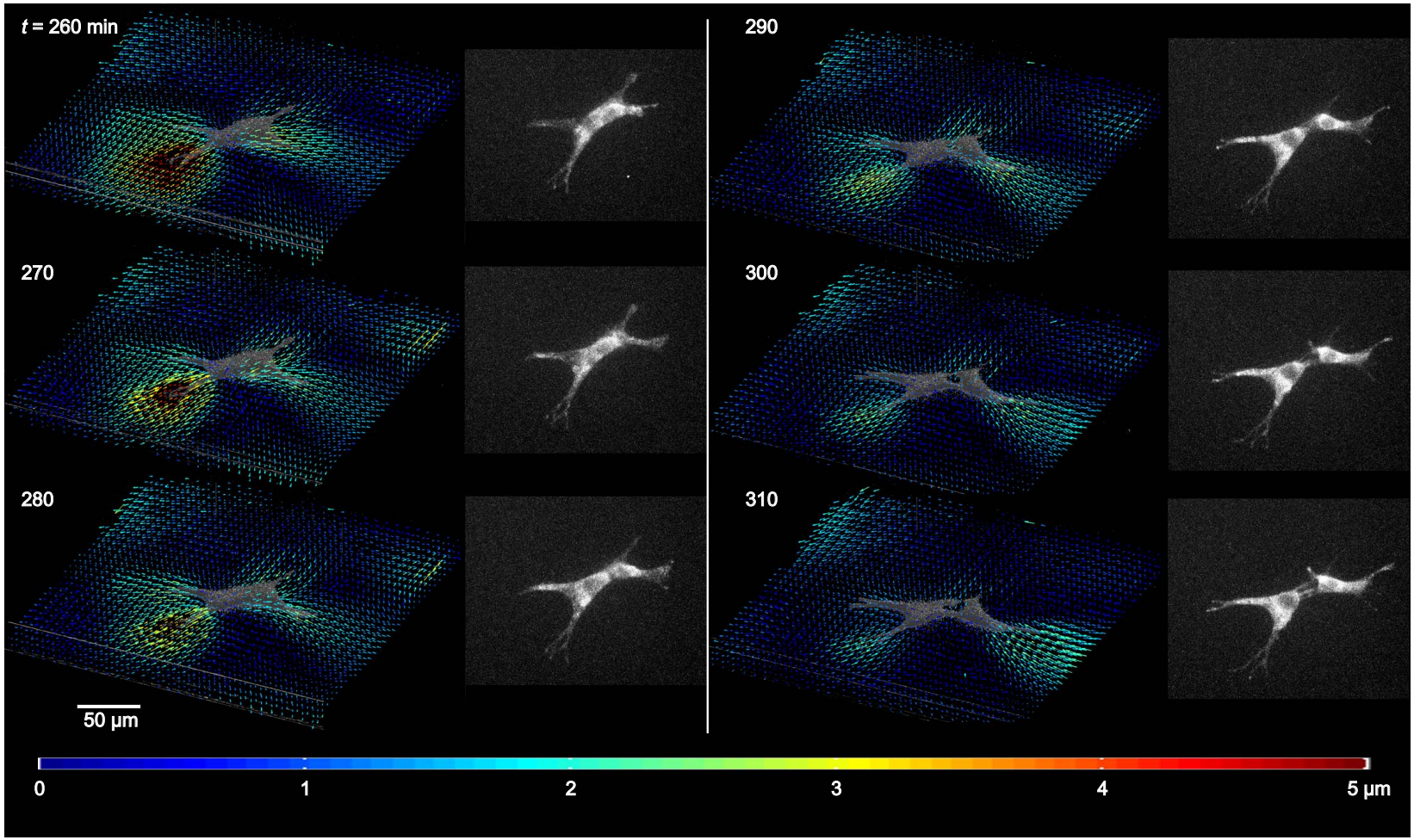

Figure 3.7: After division, the daughter cells pull on the matrix to separate from one another. The quiver plots of matrix displacements in 3D show how the matrix deforms around the daughter cells between $t = 260$ and 310 min after division occurs. The 2D maximum intensity projections of the cells show that daughter cells are moving in opposite directions attempting separation.

tension.

The interactions of dividing cells with the surrounding matrix were examined further through 3D imaging of fibrin gels labeled with fluorescent dyes (Fig. 3.9). The matrix fibers around actin–GFP fibroblasts during interphase are aligned and denser at the tips of cell protrusions than they are elsewhere (Fig. 3.8a), implying that the cell applies localized force in these areas. Images of dividing GFP–actin fibroblasts and the surrounding fibrous matrix reveal that around the mitotic protrusions the matrix is highly remodeled (Fig. 3.9a, strong red signal). In contrast, the matrix fibers adjacent to the dividing cell body remain undeformed (Fig. 3.9a) and leave a clear void separating the cell body from the matrix (Fig. 3.9a, arrows).

Inspection of the matrix voids reveals that as the cell rounds to divide, the body disengages from the matrix, leaving voids that reflect the shape of the fully spread cell (Fig. 3.9b, Fig. 3.8b). Interestingly, the matrix does not deform further as the cell divides, implying that the voids form through proteolysis of the gel as the cell spreads after seeding. Throughout mitosis, the tips of the cellular protrusions are well embedded in the matrix meshwork (Fig. 3.9, Fig. 3.8b,c) consistent with the large matrix displacements measured at the tips (Fig. 3.6b, $t = 0$). Imaging of live fibroblasts that express GFP fused to the focal adhesion protein vinculin further confirms that the cell body does not adhere to the matrix during division (Fig. 3.9c, lower image), while non-dividing, well-spread fibroblasts form focal adhesion clusters in 3D fibrin matrices (Fig. 3.9c, top image). After division, the daughter cells first reoccupy the matrix voids, a region of lower physical resistance (Fig. 3.8d); then they invade the fibrillar meshwork, a process that requires application of traction forces (Fig. 3.6b, $t = 210$ min, Fig. 3.9c). Voids such as those observed here are distinctive features of 3D environments, and are likely to influence cellular location, orientation, movement, and shape *in vivo*.

This study has identified new roles for cell–matrix interactions in regulating cell division in 3D environments. The model that emerges is summarized in Fig. 3.10: During cell rounding, the cell releases adhesive contacts with the matrix around the cell body, but remains anchored by traction forces acting at the tips of polarized long protrusions. The dividing cell applies

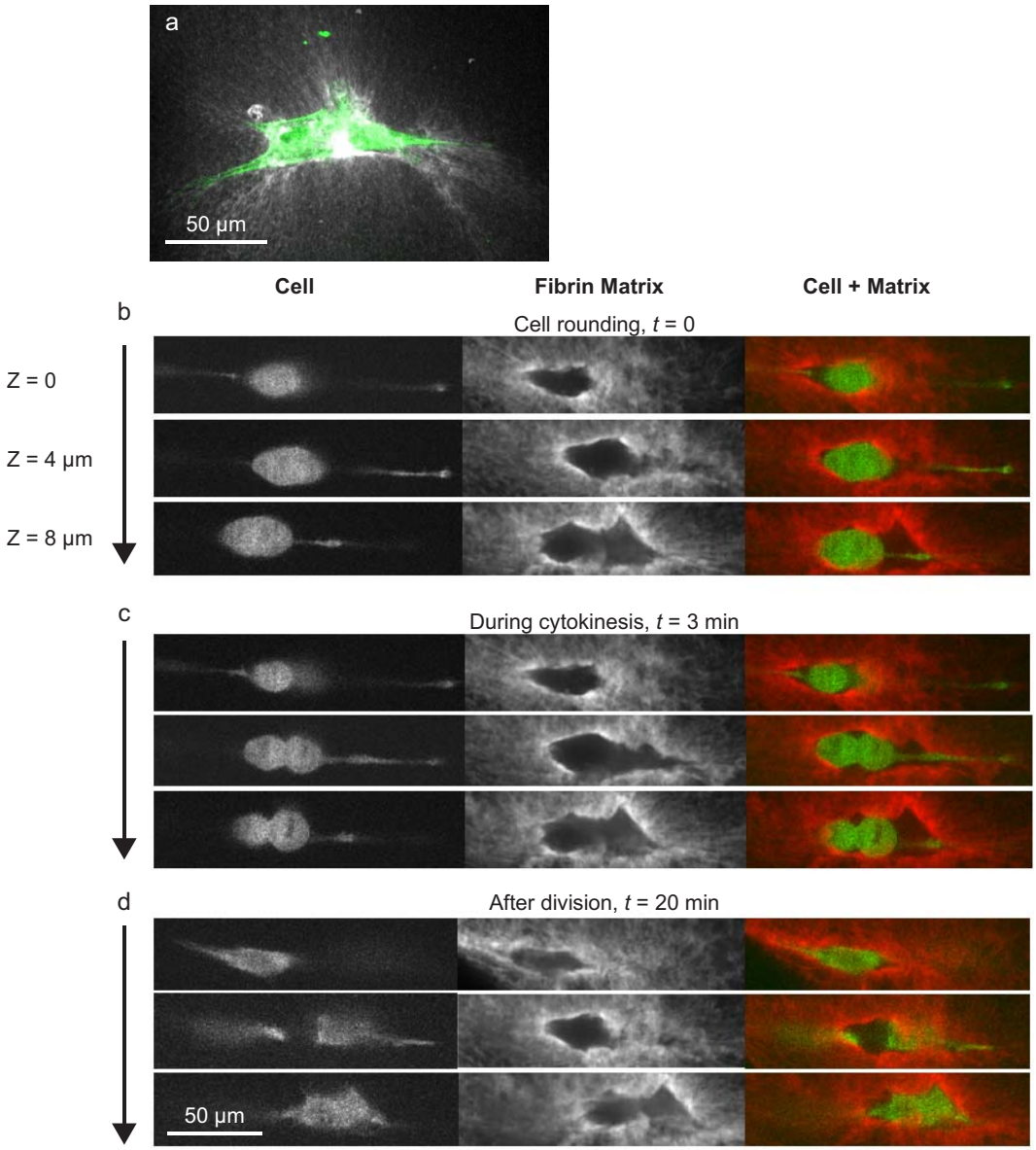

Figure 3.8: Direct visualization of cell–matrix interactions during division. (a) Maximum intensity projection image of a spread GFP–actin fibroblast (green) during interphase in a fluorescently labeled fibrin matrix (gray). The cell is well embedded in the matrix, and the matrix is aligned and denser (brighter) at the cell protrusion tips. (b–d) Fibroblast (gray on left panel, green on right panel) embedded in a fibrin matrix (gray on middle panel, red on right). Each image shows one confocal plane at various z focus points as the cell rounds to a sphere (b), during cytokinesis (c), and following division (d). While the protrusion tips are well embedded in matrix, voids around the cell body indicate that the cell body disengages from the matrix during division. After cytokinesis, the daughter cells take on the shape of the matrix void (d).

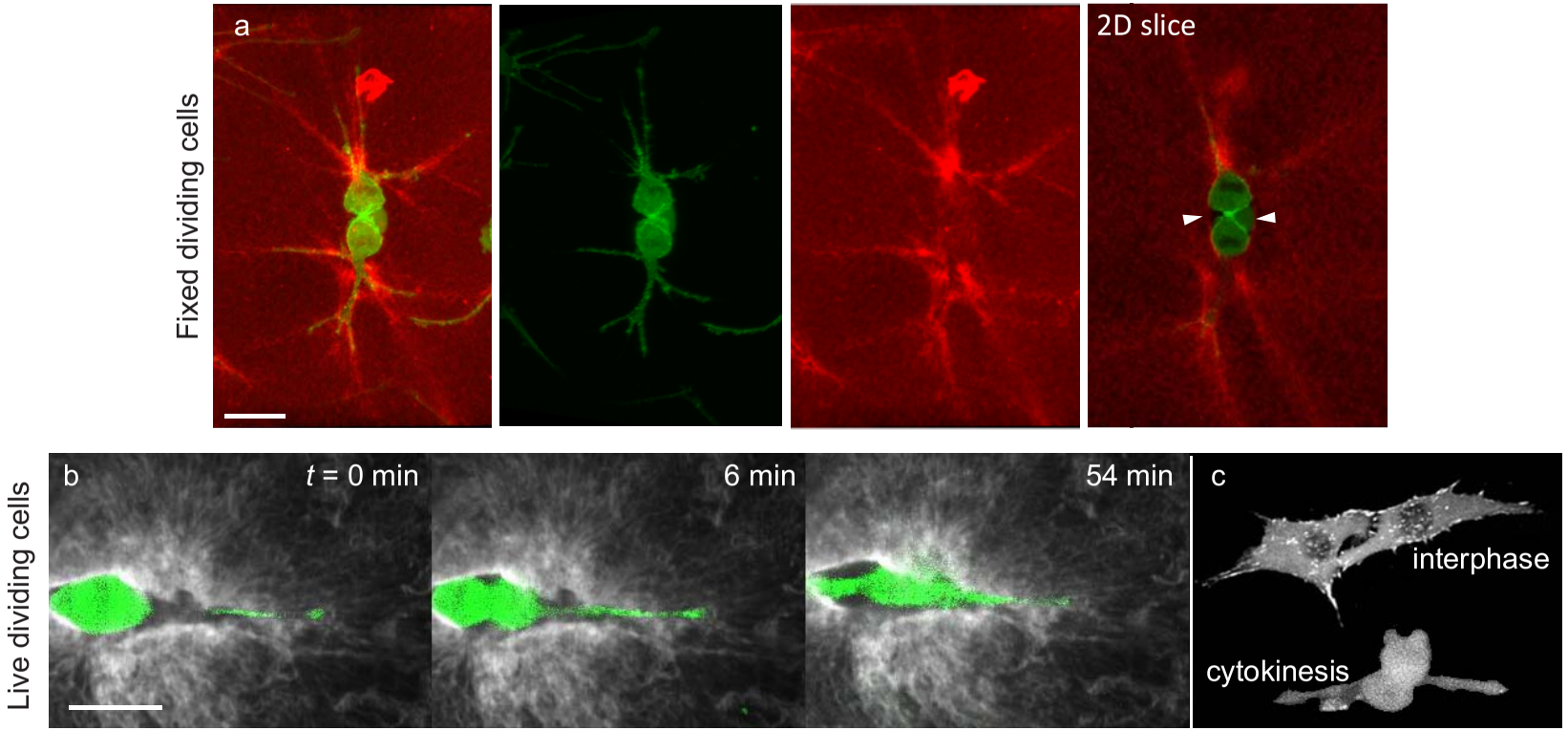

Figure 3.9: Imaging of dividing cells embedded in fluorescently labeled fibrin matrices. (a) Fixed gels showing a dividing fibroblast cell (actin–GFP, green) during cytokinesis and the fibrin matrix (red). Dividing cells deform the matrix locally around the mitotic protrusions (strong red signal due to dense fibers) but not around the cell body. Matrix voids are evident between the mitotic cell body and the matrix ("2D slice," arrowheads). (b) One confocal plane of a live dividing cell (actin, green) and the labeled fibrin matrix (gray) at cell rounding ($t = 0$), cytokinesis ($t = 6$ min) and shortly after division ($t = 54$ min). During division, voids separate the cell and matrix, indicating uncoupling of the cell body from the surrounding matrix. Throughout the division process, long, thin protrusions are apparent, with their tips well embedded in the matrix. After division, the daughter cells spread to fill the matrix voids. See SI Fig. 3.7 for the entire sequence of events. (c) Maximum intensity projections of live fibroblasts expressing GFP–vinculin. The bright spots indicate focal adhesions during interphase (upper image). Live imaging of GFP–vinculin reveals a significantly lower expression of focal adhesions during division (lower image, cytokinesis). Scale bars are 30 µm.

tensile forces against the extracellular matrix through the mitotic protrusions in the direction of the division axis. These forces and the resulting localized tension that develops along matrix fibers may trigger intracellular signaling pathways that play complementary roles in regulating cell division. While future investigations should reveal the impact of specific extracellular cues including matrix stiffness, geometry or adhesion sites, this study highlights the importance of cell–matrix interactions in shaping cell division in three dimensions.

3.4 Materials and Methods

3.4.1 Cell Culture

Swiss 3T3 fibroblasts (passages 10–20) stably transfected either with GFP–actin or with GFP–vinculin were cultured in DMEM medium supplemented with 10% fetal bovine serum and $1\times$ non-essential amino acids in a $37°$C humid incubator. Human umbilical vein endothelial cells (HUVEC) stably transfected with RFP (Angio–Proteomie, Boston, MA) were cultured in Endothelial Growth Medium containing 5% serum, growth supplements and $1\times$ penicillin and streptomycin (Angio–Proteomie) (passages 4–9) also in a $37°$C humid incubator.

3.4.2 Fibrin Gel Preparation

3T3 fibroblasts–GFP–actin (ca. 3000 cells) and HUVEC–RFP (ca. 3000 cells) were mixed with 20 µL of 5 mg/mL fibrinogen (Omrix Biopharmaceuticals, Israel). In a separate vial, 0.5 µm carboxylated modified fluorescent particles (Invitrogen, Carlsbad, CA) were mixed with 20 µL of a 20 U/mL thrombin solution (Omrix Biopharmaceuticals, Israel) and vortexed for 1 minute to a final particle concentration of 0.05%. The thrombin suspension was placed on a # 1.5 coverslip in a 35 mm dish (MatTek, Ashland, MA), and mixed gently with the fibrinogen suspension. The resulting fibrin gel was placed in the incubator for 15 minutes to polymerize fully, after which warm medium (50% fibroblast, 50% HUVEC medium) was added to cover the gel. For imaging of cell division without measurement of matrix displacements, fibrin gels

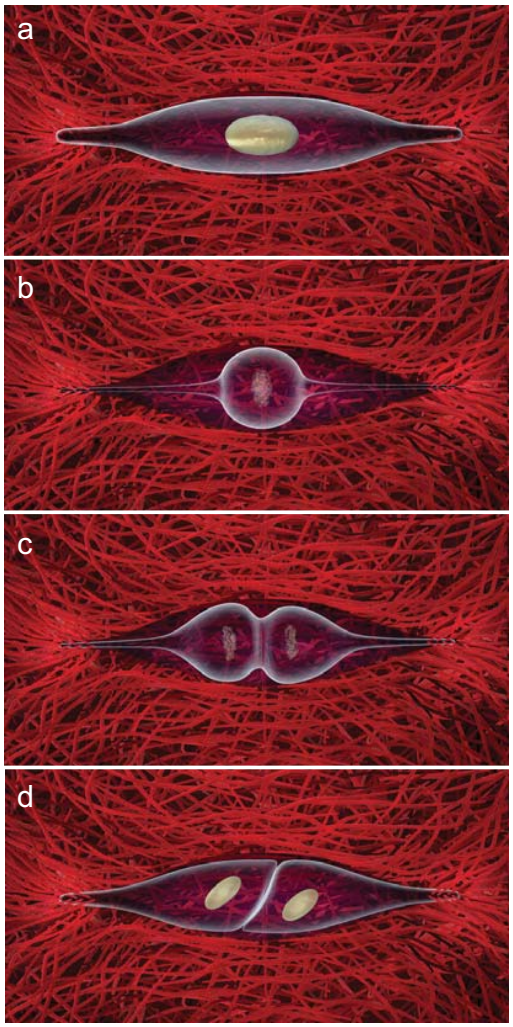

Figure 3.10: Illustration of cell division in a 3D matrix. (a) A cell starts out spread and fully embedded in the matrix meshwork while maintaining an elongated shape. (b) As the cell rounds, protrusions thin and a void is created between the cell and matrix. The shape of the void is determined by the shape of the spread cell. Protrusion tips are well embedded in the matrix at all times. (c) The cell divides along the direction of the protrusions while exerting minimal tractions on the matrix at the cell body but applying high tractions at the tips of the protrusions. (d) Daughter cells split apart, fill the matrix void space, and re-spread into the matrix along the long axis of the protrusions.

were made in a similar way but without including fluorescent particles.

3.4.3 Fibrin Gel Labeling and Fixation

Alexa Fluor 546 carboxylic acid, succinimidyl ester (Invitrogen, catalog number A20002) was mixed with fibrinogen solution in a 7.5:1 molar ratio for 1 hour at room temperature and then filtered through a HiTrap desalting column (GE Healthcare, Milwaukee, WI) packed with Sephadex G–25 resin to separate the unreacted dye. The labeled fibrinogen was then mixed with solution of thrombin/cells to create labeled, cell-loaded fibrin gels (as described above). For the fixation protocols, labeled fibrin gels loaded with 3T3 GFP–actin cells for at least 6 hours were immersed in 4% paraformaldehyde for 10 minutes and subsequently washed with PBS. The nuclear material was labeled with DAPI before imaging.

3.4.4 Fibrin Gel Characterization

The constitutive mechanical properties of fibrin gels without cells were measured using a stress-controlled AR1000 rheometer equipped with 8-mm diameter aluminum parallel plates. Frequency sweep and creep tests were performed. The fibrin gel was prepared on the rheometer and placed between sheets of sandpaper to avoid slipping. The bulk material stiffness could not be used to compute traction forces owing to local matrix inhomogeneity at the scale of the cell.

3.4.5 Time-Lapse Microscopy

After overnight incubation, the fibrin gels were imaged with a Swept Field confocal microscope mounted on a Ti stand (Nikon Instruments, Melville, NY) outfitted with a 40×1.15 NA water immersion objective (Nikon) using the microscope's 30 µm pinhole (for imaging the fluorescent particles), 45 µm pinhole (for imaging the fibrin gel), or 60 µm pinhole (for imaging the cells). Imaging was performed in a custom-built $37°$C/5% CO2 incubation chamber after allowing the system to thermally equilibrate for ca. 4 hours. All experiments were conducted

on cells positioned at least 100 μm from the surface of the gel.

Confocal z-stacks capturing single fibroblast cells were acquired every 15–30 minutes (for measurement of matrix displacements) or every 2–3 minutes (for visualizing dividing cells) for about 6 hours. Stacks were collected with a z-step size of 0.4 μm (for displacement measurements) to 1 μm (for cell visualization). For experiments involving analysis of matrix displacements, blebbistatin (85 μM, Sigma-Aldrich, St. Louis, MO) was added to the medium at the end of the experiment and stress-free stacks were acquired for an additional 4 hours.

3.4.6 Measurement of Matrix Displacements

To compute matrix displacements, 0.5 μm fluorescent particles (Invitrogen) were used to create a random speckle pattern for a digital volume correlation (DVC) algorithm [59] that was implemented in MATLAB (The MathWorks Inc., Natick, MA). Before running the DVC algorithm, deconvolution was performed on the volume stacks of the particles using the Lucy–Richardson algorithm as described previously [59]. The DVC algorithm used a Fourier-transform-based correlation to compute the 3D displacements at the center of a subset of $64 \times 64 \times 64$ voxels on a grid of points within the image volume of $512 \times 512 \times 276$ voxels. Real time displacements were computed by using blebbistatin (final concentration of 85 μM) to inhibit the cell's myosin–II activity, thus allowing the gel to recover to an unstressed state. All stacks collected before injecting blebbistatin were correlated to the unstressed stack acquired after addition of blebbistatin. To account for minor swelling/shrinking of the fibrin gels during displacement measurements, the mean normal matrix strains were computed. The displacement fields were then corrected by subtracting the displacements associated with mean normal matrix strains. It was found that shortly after injection of blebbistatin, total displacements dropped sharply to zero, confirming stress-free conditions (Fig. 3.6c).

To quantify the experimental error associated with the displacement measurements, separate experiments were performed on fibrin gels without cells. In these experiments, confocal stacks were collected every 30 minutes for approximately 6 hours. Then, blebbistatin was in-

jected into the medium to a concentration of 85 μM. The DVC algorithm was applied to compute the matrix displacements and strains. Further experiments to analyze the DVC algorithm's ability to compute matrix displacements and strains were conducted by applying a computational translation or strain to the volume stacks. After correcting for swelling or shrinking of the fibrin gels, displacements were found to be within a standard deviation (~ 0.3 μm) of their expected values. A further experiment was performed wherein a fibrin gel was imaged during a compression experiment as described previously [59]. The displacements again were within a standard deviation of their expected values.

3.4.7 Quantification of Protrusion Direction and Division Orientation

Mitotic protrusion directions were measured during cell rounding by fitting a line between the protrusion tip and its intersection with the rounded cell body. Vectors associated with the direction of each protrusion were computed and normalized to unit length. The normalized protrusion vectors were averaged to determine a mean resultant protrusion direction. The division axis orientation was quantified by fitting spheres to renderings of the two daughter cells collected immediately after cytokinesis, computing the vector connecting the centers of the spheres, and normalizing the computed vector to unit length. The angle between the average protrusion direction and the division axis orientation was computed by taking the dot product of the unit vectors associated with these directions. The distribution of angles between the division axes and protrusion directions was compared to a uniform distribution. For cells embedded in 3D gels, it was found that the data do not fit a uniform distribution at a confidence level of $p < 0.001\%$ (Kolmogorov-Smirnov test).

Chapter 4

Cell Invasion in a Three-Dimensional Matrix

Cell migration is involved in processes ranging from embryonic development to cancer cell invasion to wound healing. Previous work has revealed the chemical and physical mechanisms involved in cell migration on a two-dimensional (2D) substrate [84], and there is currently interest in extending the experimental approaches used in 2D systems to a physiologically relevant three-dimensional (3D) matrix. For example, previous work has measured cell migration speeds in a fibrous 3D matrix to assess the effect of matrix modulus and density [85]. Other work has highlighted the molecular signaling pathways that control motility in three dimensions and the mechanisms the cell uses to navigate through an array of matrix fibers [86]. Several questions remain in our understanding of cell migration, especially in the mechanics required for 3D migration. For example, cell motility along linear ("one-dimensional") tracks has been shown to mimic physical migration mechanisms in three dimensions with migration rates, directional persistence, and dependence on myosin contractility similar between one and three dimensions [87]. Other work has shown that cells apply several different mechanisms to make their way through a 3D fibrous network, and the reason for the cell's choice of mechanism remains unknown [88, 89]. These open questions require developing new experimental approaches for quantifying the mechanical interaction between a cell and its surroundings. The lack of experimental techniques is due in part to the increased difficulties of cell culture in a 3D matrix as compared to a 2D substrate and a lack of tools to characterize cell motility

and matrix deformation in three dimensions.

This chapter describes the study of the fundamental process of cell spreading into a 3D fibrin matrix, which is an early stage in cell migration. Previous experiments on cell spreading have followed a rounded cell flattening on a 2D substrate as a model system for investigating cell motility. It has been shown that cell spreading on a 2D substrate occurs in a three step process, and the timescales associated with each step have been quantified [90]. Other work developed homogenized [91] and microstructural [92] models to relate cell spreading to stress within the actin cytoskeleton.

In three dimensions, cell spreading is a more complex process, because the cell interacts with a fibrous matrix that both creates points for cell adhesion and contains fibers that inhibit motion. Thus, spreading in three dimensions is better described as invasion into a fibrous matrix. To navigate through a fibrous mesh, cells have been shown both to squeeze their way through gaps in the fiber network and to move aside or chemically degrade impeding matrix fibers [88]. Previous work in cell invasion has observed matrix fiber alignment [93] and degradation [94] to infer the mechanical interaction between a cell and the matrix, but there remains a lack of information on the mechanical forces between an invading cell and the matrix. Here, the tractions applied by an invading cell to the matrix are measured directly using the 3D traction force microscopy (TFM) technique described in Chapter 2. The resulting matrix deformations are quantified using TFM and direct microstructural imaging. Mechanical measurements and microstructural analysis achieved together using the combined TFM and matrix imaging approach reveal the physical mechanisms associated with cell invasion into a fibrous matrix.

4.1 Visualizing Cell Invasion for Quantitative Analysis

NIH 3T3 fibroblasts cells were suspended in a thrombin solution and mixed with fibrinogen to form fibrin matrices with encapsulated cells as described in Chapter 2. Initially spherical

in shape, the cells began to spread within hours after encapsulation. Cell spreading began with matrix invasion by thin processes referred to here as protrusions. After several hours, spreading continued with mechanical rearrangement and proteolytic degradation of the matrix fibers surrounding each encapsulated cell. After a period of ~ 12 hours, the cells appeared fully spread in the fibrous matrix with a matrix void space occupied by the spread cell.

Cells were imaged using a Swept Field confocal microscope outfitted with a $40\times$ water immersion objective (Nikon Instruments, Melville, NY) as described in Chapter 2. The normally adherent cells were in the spherical state at the beginning of each experiment, making them more sensitive to phototoxicity [95]. Therefore, minimal laser excitation power and imaging periods of ≥ 20 min were used to minimize the effects of increased cellular photosensitivity.

4.2 Matrix Structural Changes During Invasion

Matrix fiber imaging during cell invasion has revealed that cells reorganize the surrounding matrix by applying mechanical force. For example, qualitative inspection of single matrix fibers near a spreading cell has led to the observation that cells align matrix fibers toward the cell, indicative of traction force applied by the cell to the matrix [93]. Here, a more quantitative analysis is employed to study matrix density and fiber alignment. Matrix density is quantified by computing the mean normalized fluorescent intensity in a region of interest. Fiber alignment is assessed by adapting a previously described approach [96, 97]. The power spectral density (PSD) of a selected region of the fibrin matrix is computed as shown in Fig. 4.1b. Aligned fibers in the untransformed image appear as bands in the PSD image oriented at an angle of 90° to the fiber alignment angle in the untransformed image. The relative intensities of the bands in the PSD image are analyzed in polar coordinates to determine the angles that correspond to alignment of matrix fibers. Mean values along a ray drawn from the center to the edge of the PSD image are computed for various polar angles to the horizontal θ (Fig. 4.1c). As described previously [97], central PSD values, which are related to long wavelength

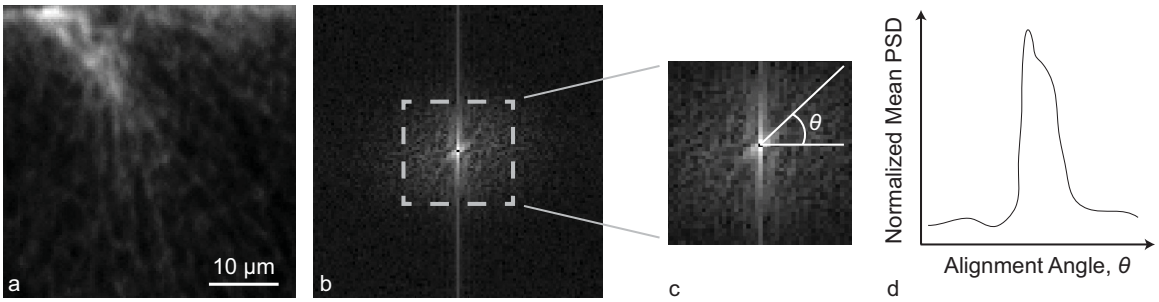

Figure 4.1: Matrix fiber alignment is quantified using a Fourier-transform-based technique. A region of interest (a) is selected from the volume stack, and its power spectral density (PSD) is computed (b). Fiber alignment in the region of interest corresponds to bands in the PSD image oriented at 90° to the fiber alignment angle. The angle of alignment is quantified by drawing rays from the center of the image at different angles θ (c). Finally, the mean PSD along each ray is computed and plotted for each angle θ (d).

image characteristics like mean image brightness, are not used in computing the mean. PSD mean values are normalized by the maximum mean value and plotted against angle θ (Fig. 4.1d). Normalized mean PSD values that are larger than the baseline PSD indicate more fiber alignment in the direction given by $\theta \pm 90^\circ$.

Fluorescently labeled matrix and single cells (labeled with green fluorescent protein linked to actin) are imaged during cell invasion in a 3D matrix (Fig. 4.2a). During the initial stages of invasion, the cell typically extends small perturbations in all directions (Fig. 4.2a $t = 0$ hr) to probe its local environment. After choosing a direction to spread, the cell extends a thin protrusion into the matrix. After a period of hours, the protrusion is hindered by fibers encircling the protrusion's leading edge (Fig. 4.2a $t = 3$ hr 20 min). This circular fiber structure corresponds to a denser distribution of fibers, observed by an increase in matrix fluorescent intensity (Fig. 4.2b, Region 1) at this time point. As the protrusion continues to grow, matrix fluorescent intensity increases, indicating that the cell rearranges the matrix fibers as it invades.

As shown in Fig. 4.2, the protrusion passes entirely through Region 1 at $t = 5$ hrs, and at this time, fluorescent intensity stops increasing in Region 1. Also at this time matrix fibers are not only more dense than far from the cell, but they are also more aligned. Analysis of fiber alignment along the protrusion stem at $t = 5$ hrs using PSD analysis (Fig. 4.2c) shows a spike in PSD values at an angle of -20°, indicating fiber alignment at an angle of $-20^\circ + 90^\circ = 70^\circ$,

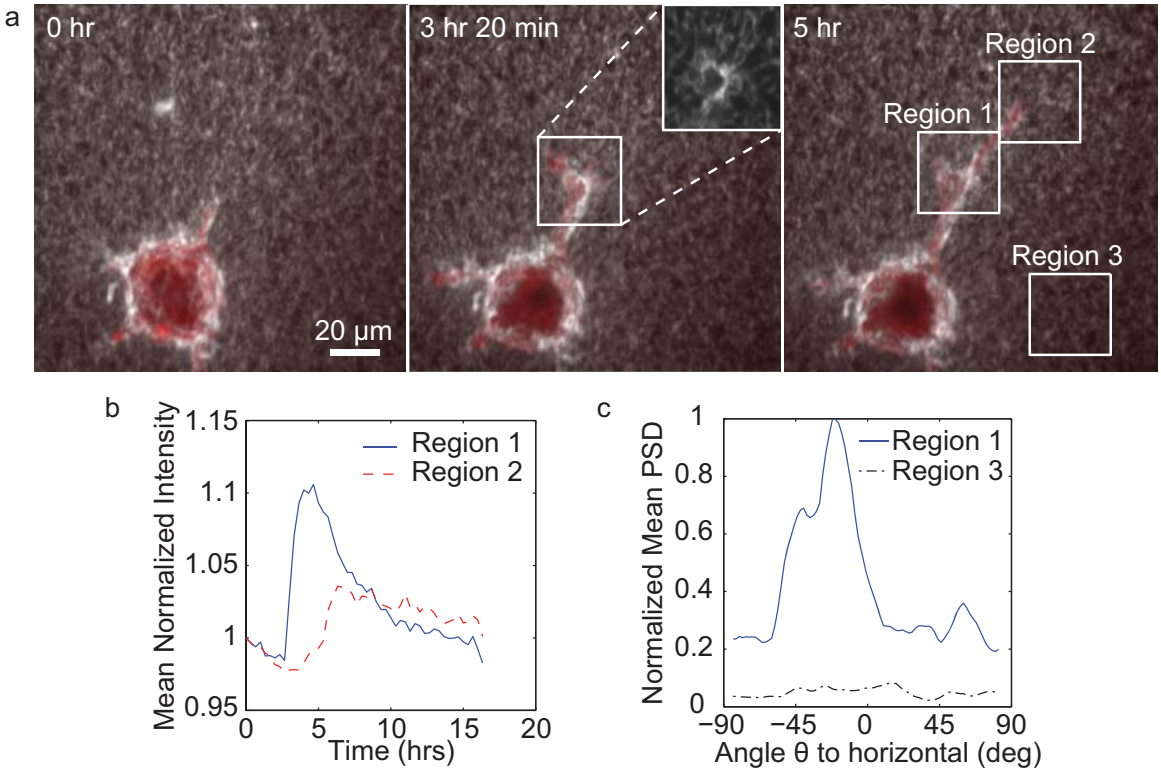

Figure 4.2: (a) Time-resolved morphological changes of the fibrous matrix (gray) during cell invasion. The cell initially deforms the matrix fibers around the protrusion stem (until 3 hr 20 min). Later, as the cell continues invading (5 hr), no apparent remodeling occurs at tip of cell protrusion. (b) As the protrusion initially extends into the matrix, normalized matrix fluorescent intensity sharply increases at the region surrounding the protrusion stem, corresponding to an increase in fiber density (Region 1). Fiber density is significantly lower at later time points around the protrusion's leading edge (Region 2). (c) The normalized mean PSD for Regions 1 and 3 is computed at $t = 5$ hrs. The PSD peak for Region 1, oriented 90° to the fiber alignment angle, indicates that the matrix fibers become aligned in the direction of the protrusion. The initial time, $t = 0$ hrs, corresponds to the first volume stack collected, which was ~ 5 hrs after cell encapsulation.

the same as the angle of the protrusion. In contrast, a region far from the cell (Fig. 4.2, Region 3) has an isotropic fiber orientation. After $t = 5$ hrs, fluorescent intensity begins to decrease, which could correspond to proteolytic degradation of the matrix by the cellular protrusion. As the protrusion extends into Region 2, matrix fluorescence in Region 2 increases (Fig. 4.2b), indicating that the leading edge of the growing protrusion continues to rearrange the matrix fibers.

4.3 Signatures of Matrix Tension and Compression

Direct microstructural imaging of matrix fibers can give a qualitative picture of where the cell applies traction to the matrix. Like the substrate wrinkling experiments described in Chapter 1, this qualitative analysis cannot yield a direct measure of force. Further analysis, however, can reveal how the matrix deforms under compressive and tensile normal stresses. Rigid spherical polymethylmethacrylate particles with a diameter of 45 μm are encapsulated in fluorescently labeled fibrin matrices (3 mg/mL fibrinogen, 40 μL total volume) as described in Chapter 2. The matrix fibers are imaged using confocal microscopy during compression experiments using a loading system similar to that described previously [59]. As shown in Fig. 4.3a, compressive stress is applied in the axial z direction. The mechanical solution for this experimental configuration is given by Goodier [98], and the stress concentration factor (ratio of local stress to far field stress) is given in Fig. 4.3b. The axial compression results compressive stress within the matrix at the poles of the sphere and, depending on the Poisson's ratio of the matrix, tensile stress along the equatorial plane. Under axial loading, the regions of the matrix under compression become dense with a high fluorescent intensity compared with regions away from the sphere (Fig. 4.3c, $z = 0$, 8 μm). In contrast, matrix intensity decreases in regions of the matrix near the equator of the sphere (Fig. 4.3c, $z = 32$, 40 μm). The reduction in image intensity near the equator indicates tensile stresses within the matrix. Inspection of Fig. 4.3b shows that tensile stresses only develop for a Poisson's ratio in the range of 0.4–0.5.

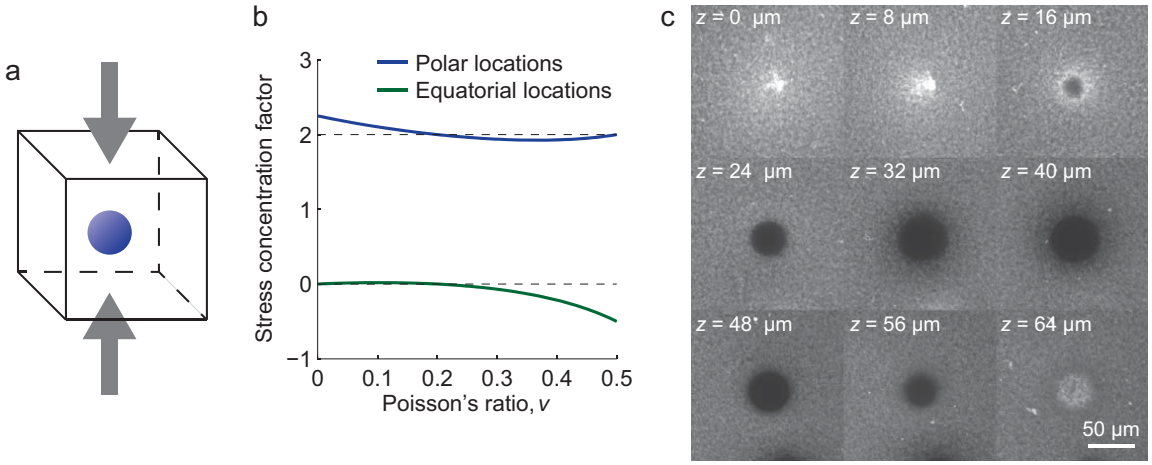

Figure 4.3: Local matrix deformation around a sphere under uniaxial compression of $\sim 30\%$. (a) A fibrin matrix (3 mg/mL fibrinogen) is loaded under compression. A rigid sphere is included to create an inhomogeneous stress state. (b) The stress concentration factor in the matrix on the sphere's surface is computed from Ref. [98] for the sphere's north/south poles and equator. Since the sphere is under compression, a positive stress concentration factor indicates compression. (c) The fluorescently labeled fibrin matrix is imaged during compression and plotted for various planes separated by 8 μm in the axial (z) direction.

Thus, the fibrin matrix behaves as an incompressible (or nearly incompressible) material. At the top of the sphere (Fig. 4.3b $z = 64$ μm) refraction of light traveling through the sphere during imaging degrades the image quality.

A second experiment is performed to load the matrix around the spherical inclusion in biaxial tension instead of uniaxial compression. The biaxial tension state is achieved by placing a glass coverslip onto the matrix during polymerization (Fig. 4.4a). When adhered to glass on the top and bottom, the matrix expands in biaxial tension due to the capillary forces between the fluid in the matrix and the glass, and typical matrix images at various axial (z) positions are given in Fig. 4.4b. The biaxial tension results in a reduction in matrix density at the sphere's equatorial plane (Fig. 4.4b, $z = 32$ μm), similar to that observed in Fig. 4.3. Also as a result of the biaxial tension, compressive stress is observed at the top and bottom poles of the spherical inclusion. Unique to this experiment is that the biaxial tension is so large that the matrix disconnects from the sphere, creating a void space next to the sphere (Fig. 4.4b, $z = 24$ μm) similar to the voids observed during cell division described in Chapter 3. Next to the void space where the matrix disconnects from the sphere, a unique area of bright and aligned fibers

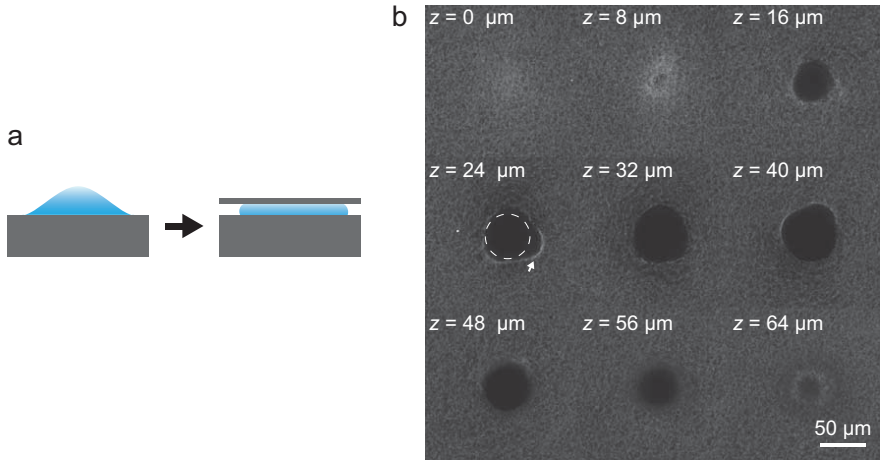

Figure 4.4: Local matrix deformation around a sphere under biaxial tension. (a) Biaxial tension is created within a fibrin matrix (3 mg/mL fibrinogen) by placing a coverslip on the gel during polymerization. (b) The resulting biaxial stress state in the in-plane directions is sufficient to rupture the adhesion between the fibrin matrix and the sphere (sphere outline shown by dotted line), as shown in the image slices of the fibrin matrix. Matrix fiber alignment and densification is observed where the matrix disconnects from the sphere (arrow).

is observed (Fig. 4.4b, arrow). These bright, aligned fibers appear to be unique features of a void space in the matrix, and their formation could result from the debonding of previously adhered fibers.

The matrix signatures of tension (increased pore size, decreased fluorescent intensity) and compression (fiber compaction, increased fluorescent intensity) presented here represent a set of "semi-quantitative" observations of the deformations within the 3D matrix. Inspection of Fig. 4.2a shows bright and aligned matrix fibers surrounding the cell and the invading cell protrusion. These fibers most resemble the fibers that align after disconnecting from the sphere due to tensile stress in Fig. 4.4b (arrow). Thus these aligned fibers with high fluorescent intensity appear to show the boundary of the fibrin matrix. Since the matrix fibers show alignment and high fluorescent intensity along the cell protrusion (Fig. 4.2a), analysis of the fibrin matrix fluorescent intensity (Fig. 4.2b) can give a readout of where the cell is proteolytically degrading and mechancially rearranging the matrix. While microstructural analysis does not allow for direct measurements of cell tractions, the analysis described here could be employed to predict cell tractions in future experiments. As such, direct imaging of the matrix is a powerful tool

for investigations of cell invasion and other cellular processes.

4.4 Quantifying Cell Tractions in Three Dimensions

While image analysis of matrix fibers gives qualitative and semi-quantitative information about cell tractions, quantitative experimental approaches can provide a direct readout of the cell's mechanical state. Tractions applied by live cells invading a 3D fibrin matrix are measured using real time 3D traction force microscopy. Matrix displacements (Fig. 4.5a) are computed from image volume stacks of the matrix collected every 20 minutes and analyzed using digital volume correlation (DVC). Since the first images were collected shortly (~ 5 hours) after cell seeding—before the cell began to apply tractions to the matrix—the first volume stack was used as an undeformed reference for DVC. Typical matrix displacements are ~ 4 μm and located near the leading edge of the cell protrusion. The magnitude and spatial extent of matrix displacements generally increase as the cell protrusion grows. Tractions, computed directly from the displacement data as described in Chapter 2, have a maximum magnitude of ~ 10 Pa near the leading edge of the cellular protrusion (Fig. 4.5b).

Inspection of individual time points (Fig. 4.6) shows that the maximum traction magnitudes applied by the cell to the matrix localize at discrete points on the cell surface. Traction components along (tangent to) the cell protrusion and normal to the protrusion surface are plotted in the red-to-blue color map in Fig. 4.6. In the early stages of cell spreading, the cell applies moderate tractions inward, toward the cell body (Fig. 4.6b). Normal traction components are minimal at this time point. When the cell encounters obstacles in the matrix, tractions increase. For example, at the leading edge of the protrusion, the cell applies large (magnitude ~ 10 Pa) compressive tractions in the tangential direction (Fig. 4.6b). The compressive traction is in the outward direction, meaning the cell pushes against the matrix at this location during spreading.

Later, as the protrusion continues invading the matrix, maximum tractions transition to

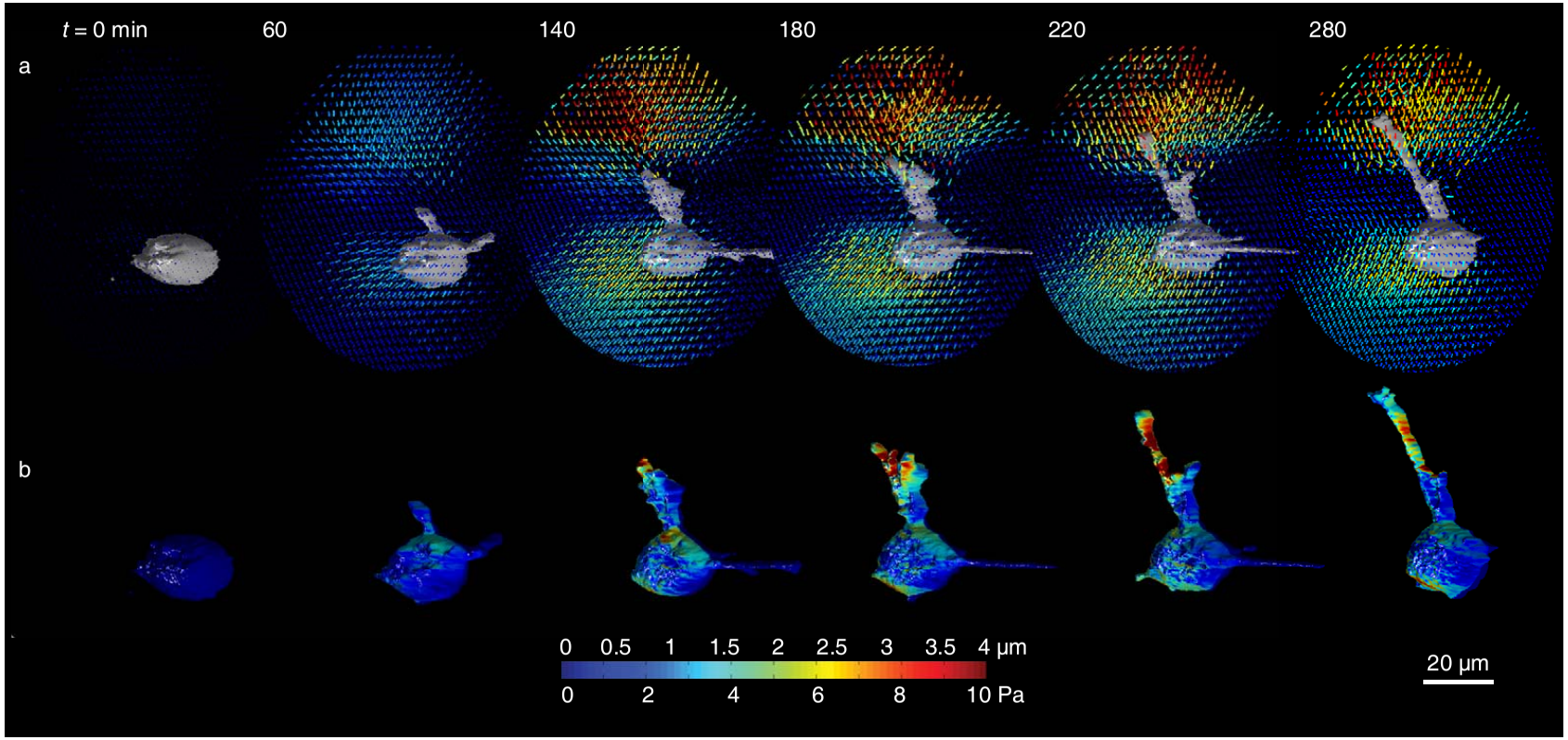

Figure 4.5: Time-resolved cell/matrix mechanical interactions during cell invasion in a 3D fibrin matrix. (a) 3D cell-induced matrix displacements, and (b) 3D traction magnitudes applied by the cell to the matrix.

locations behind the protrusion tip (~ 10 Pa traction, Fig. 4.6c). Except for some pushing tractions remaining from $t = 1$ hr 40 min, the tractions at later times are primarily in the inward direction, toward the cell body, indicating the cell is applying tension. This dynamic change in traction directions suggests that cells modulate the direction and magnitude of the tractions they apply to extend into the fibrous matrix. The fact that the largest traction magnitudes in Fig. 4.6c do not correspond to the leading edge of the protrusion indicates that the cell anchors itself to the matrix at distinct points and then uses these anchor points to pull the main body forward to continue invading.

The dynamics of invasion are quantified by measuring the growth of the cell protrusion over time (Fig. 4.7b). The protrusion grows at nearly a constant rate of ~ 10 μm/hr (Fig. 4.6b), while the mean traction magnitudes (Fig. 4.6c) in both the normal and tangential directions fluctuate significantly in time, indicating that the protrusion growth rate appears to be independent of tractions applied by the cell to the matrix. It is observed that cells exert approximately equal tangential and normal tractions during the spreading process (Fig. 4.7c) suggesting that the cell engages the extracellular matrix with both shearing and normal force mechanisms in three dimensions.

The magnitude of the net force applied by the protrusion is also computed and plotted over time (Fig. 4.7d). Similar to the tractions, the force applied by the protrusion to the matrix appears uncorrelated with the growth of the protrusion. The greatest force occurs at $t = 2$ hr, which is just after the time point shown in Fig. 4.6b. During this timepoint, the protrusion growth rate slows slightly (observed by flat slope of plot in Fig. 4.7b at 2 hrs). Thus, it is likely that the protrusion has encountered a dense network of matrix fibers. The cell must apply large forces to rearrange and/or degrade these fibers before protrusion growth can continue. After ~ 20 min, the force drops, indicating that the matrix fibers have been rearranged sufficiently that the cell can continue to invade the matrix without applying large forces.

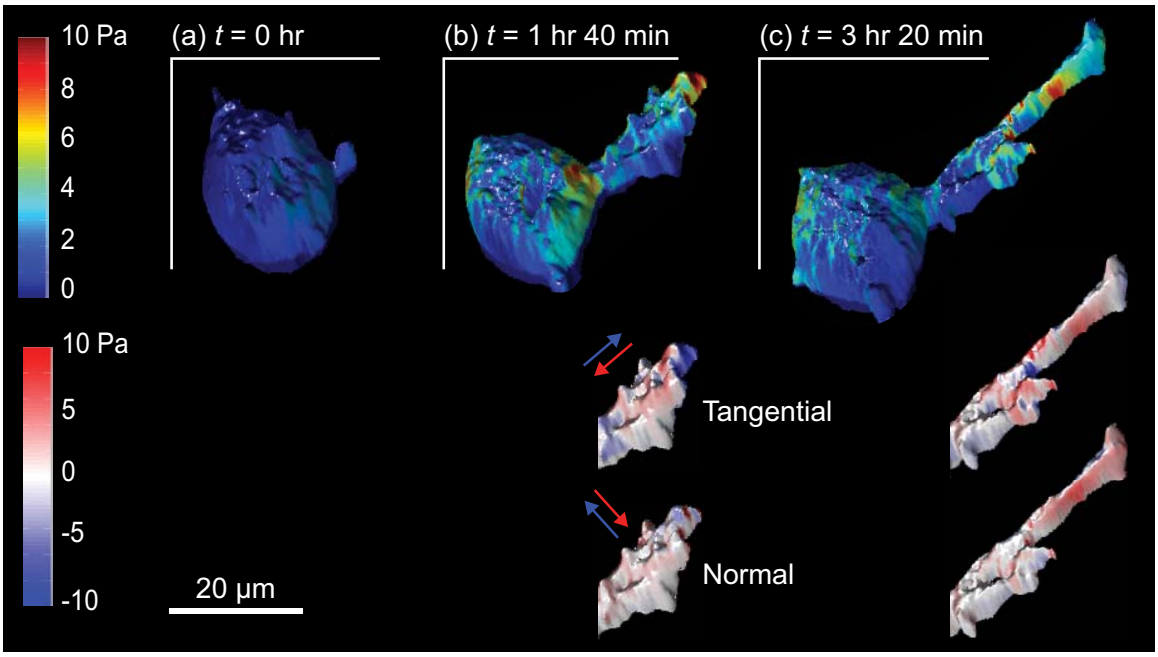

Figure 4.6: Measurement of 3D cell tractions while spreading into a fibrin matrix. Traction magnitudes are plotted using the top color scale. Traction directions along the cell protrusion are plotted in a red-to-blue contour map (bottom) in the direction along ("tangential") and perpendicular to ("normal") the protrusion. The positive direction (red) is defined as being toward the cell, and the negative direction (blue) as being away from it.

4.5 Discussion and Conclusions

4.5.1 Cell Invade at Locations Where They Apply Minimal Tractions

The tractions applied by a cell to the matrix are measured directly during the process of cell invasion into a 3D matrix. It is observed that an invading cell extends a thin protrusion into the matrix. Since the matrix has a fibrous structure, the cellular protrusion initially extends without the need to degrade or apply force to the matrix, in contrast to a previous study that suggested that cells degrade the matrix before they can spread or protrude [99]. However, this previous study [99] used a polyethylene glycol (PEG) hydrogel with a pore size of tens of nanometers, significantly smaller than the fibrous matrix used here, and therefore initial cell invasion took a longer time (~ 10 hrs). The fibrous morphology of the fibrin matrix used in this study allows the cell to begin to invade earlier (< 5 hrs) and without the need to degrade the matrix. During invasion, the protrusion grows at a nearly constant rate, and the cell increases

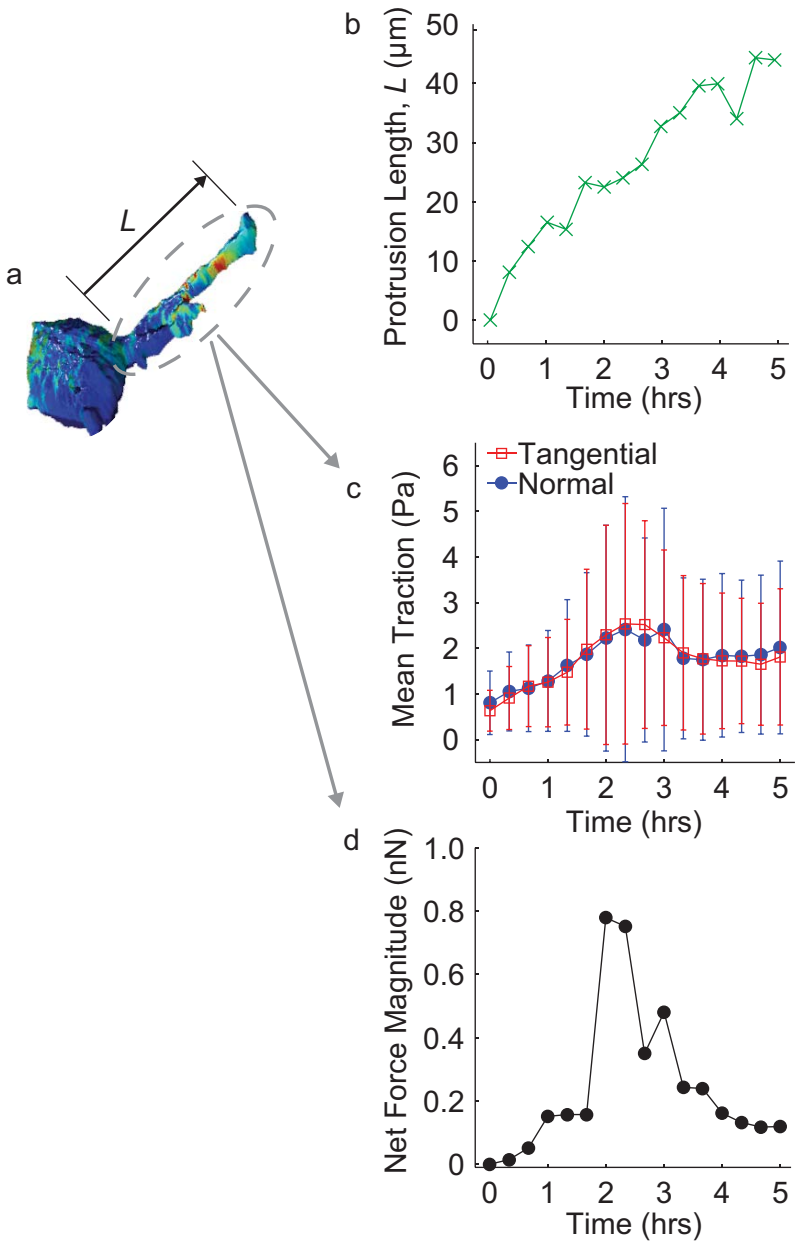

Figure 4.7: Dynamics of cell invasion. (a) The protrusion of the cell shown in Figs. 4.5 and 4.6 is analyzed to compute its length, mean traction magnitude, and net resultant force magnitude. (b) The plot of protrusion length over time indicates the cell invasion rate is nearly constant at $\sim$ 10 μm/hr. (c) Mean $\pm$ standard deviation of the magnitudes of tangential and normal traction components on the cell protrusion. The mean tractions increase as the cell begins to invade the matrix and then become constant as the cell continues to spread. (d) The resultant force applied by the protrusion to the matrix fluctuates drastically in time.

or decreases the force required to maintain a constant rate of protrusion growth. The net force magnitude applied by the protrusion to the matrix is initially small but increases when the protrusion encounters a collection of matrix fibers that inhibit its growth. Later, the force decreases again, and the cell continues to invade while applying smaller tractions.

The lack of correlation between growth rate and mean traction magnitudes indicates that the growth of the cell protrusion must be at least partially traction independent. Since protrusion growth can occur with no tractions applied to the matrix, an analogy can be drawn to climbing a ladder. The cell extends into the matrix by applying minimal force until it encounters a dense group of matrix fibers to which it can adhere. The cell then adheres, applies force, and continues to extend. Much like climbing a ladder, the cell sometimes applies maximal tractions to the matrix behind the protrusion's leading edge (Fig. 4.6c). When the cell protrusion encounters a new ladder rung—a dense collection of matrix fibers—it changes the location of maximal tractions to this new position. The observation that maximum tractions are not always located at the leading edge agrees with previous observations that matrix degradation often occurs near where the cell adheres to the matrix [93]. This study reported that the cell adheres behind the protrusion's tip so that it does not degrade the matrix at the leading edge resulting in a loss of contact between the cell and matrix.

4.5.2 Invading Cells Push Against Their Surroundings

A current open question is whether cells can push against their surrounding 3D matrix. One model for cell invasion highlights the potential importance of compression forces by describing how cells use compressive forces within the fibrous matrix to assist with degradation of the matrix [93]. These compressive forces put the matrix fibers in direct mechanical contact with proteolytic enzymes attached to the cell membrane [93]. Here a direct mechanical measurement is used to show that cells can push against their surroundings during invasion (Fig. 4.6b). The locations of maximum pushing forces appear to correlate with locations where the cell must rearrange or degrade matrix fibers to invade. The observation of cells pushing

against fibers while invading agrees with previous descriptions of cell invasion that predicted cells pushing against fibrous "belts" surrounding the invading cell [94]. In this work, ring-like structures are observed around the cellular protrusion (Fig. 4.2a) similar to these compression belts.

Besides showing that cells can apply compressive forces, the observation that cells push against the matrix while spreading gives insight to the cellular structure at the leading edge of the protrusion. The buckling load F of a single actin stress fiber can be approximated by the Euler buckling formula [100],

$$F = \frac{\pi^2 EI}{L^2} \tag{4.1}$$

where EI is the bending stiffness of the filament and L is its length. The bending stiffness EI can be approximated through the fiber's persistence length $L_p = EI/k_BT$, where k_B is Boltzmann's constant and T is temperature. The persistence length of actin stress fibers has been measured to be in the range of 10–20 μm [101]. Thus, a 10 μm stress fiber, capable of transmitting force over a distance of 10 μm (a typical length scale of a cell protrusion), would have a buckling load ~ 6 fN. The net compressive force supported by the protrusion, estimated from Fig. 4.6b is approximately 10 Pa $\times$ 5 μm^2 $= 50$ pN. Even a collection of multiple fibers would not support a load of 50 pN. However, a crosslinked fiber network with a short fiber length of < 100 nm between crosslinks would support a force of ~ 60 pN. Thus, the leading edge of the cell protrusion may contain a crosslinked network of actin fibers working together to support a compressive stress.

While the observation that cells push against the matrix while spreading diverges from a previous cell traction measurement by Legant et al. in a synthetic 3D gel [66], which did not observe outward pushing at the tips of cellular extensions, these two sets of results are not incompatible. The extracellular material used by Legant et al. was a PEG hydrogel, which did not have fibers for the cell to reorganize. Since a cell in a synthetic PEG hydrogel can only spread via chemical degradation without the ability to physically move matrix fibers, the observations by Legant et al. did not capture compressive cellular tractions. In this study, the

more biologically relevant fibrous matrix allows for observation of cellular mechanisms like the ability to support compression.

4.5.3 Summary of the Invasion Process

A summary of the invasion process is shown in Fig. 4.8. The cell initially invades by applying minimal force to the matrix. Taking this observation together with a previous study that predicted the cell protrusion begins to invade with minimal force [93], one can conclude that the cell chooses a location of low matrix fiber density to begin to invade (Fig. 4.8a, dotted circle), in agreement with a previous review [102]. The cell's decision to invade in the direction of minimal matrix resistance breaks the isotropy of the initial spherical shape of the cell and biases the cell to continue invading in one specific direction. After initial invasion in a region of low fiber density, the cell encounters obstacles in the fibrous mesh. The cell either applies a localized point-like force to rearrange a collection of matrix fibers (Fig. 4.8b), or pushes its way through a fibrous "belt" (Fig. 4.8c). These compression belts have been reported in other studies as well, and they are thought to assist in proteolytic fiber degradation [94]. Finally, the cell repeats the invasion process by spreading into new regions of low local matrix density (Fig. 4.8d). During this repeated spreading process, the cell maintains adhesions to the matrix behind the protrusion's leading edge, similar to how a ladder climber holds onto the rungs of the ladder while advancing upward.

4.6 Future Work

While this chapter has described the use of the 3D TFM technique to quantify cell tractions during invasion into a 3D fibrous matrix, further refinements to this approach could yield further insights in cell migration. For example, extending the technique to cells migrating within a 3D matrix could reveal the physical forces and energy expended by the cells during migration. Combining 3D TFM with more sophisticated cell and matrix labels could create an experimen-

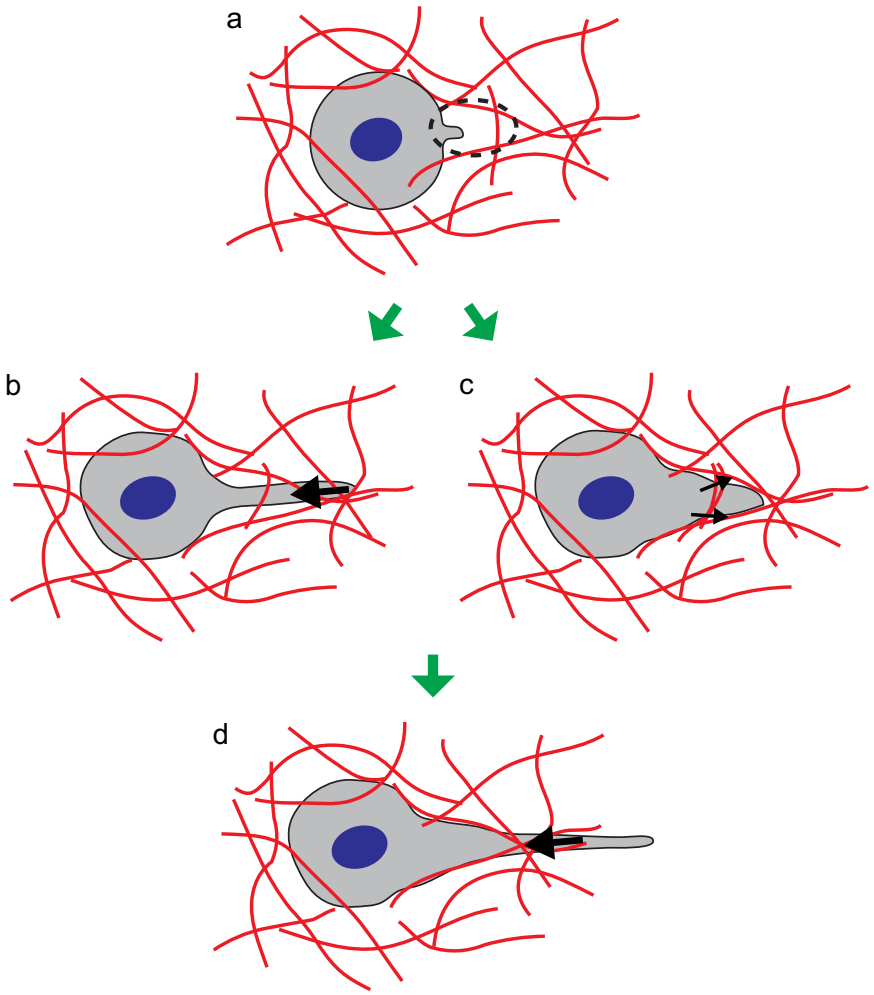

Figure 4.8: Summary of the cell invasion process. (a) The cell chooses a region where the matrix is locally less dense (dotted circle) to begin invasion. The cell then undergoes a variety of processes to continue invading. (b) Upon encountering a dense array of matrix fibers, the cell anchors itself to the matrix and pulls inward (arrow), rearranging the fibers and helping to pull the cell body forward. (c) When the cell encounters belt-like fibers that inhibit further invasion, it pushes against the fibers to reorganize and degrade them. (d) As the cell anchors itself to the matrix, it continues to extend further through a locally less dense region of ECM fibers, in a process similar to (a).

tal approach that combines microstructural, mechanical, and chemical readouts into one single approach. Finally, alternative imaging approaches like confocal reflection microscopy could be applied to develop quantitative experiments for cell invasion *in vivo*.

4.6.1 Cell-Induced Displacements During Migration

The findings on cell invasion described in this chapter help to further develop a quantitative mechanical–microstructural model for how a cell physically rearranges and chemicaly degrades a fibrous matrix to facilitate motility. Through repeated application of the 3D TFM approach, it has been found that it takes > 30 hours after seeding the cells in the fibrin matrix for the 3T3 fibroblast cells to sufficiently degrade the fibrin matrix (3 mg/mL fibrinogen) for migration. Here, preliminary experiments are performed to quantify 3D matrix displacements induced by migrating cells. Displacements are measured up to 30 hours after seeding the cells in the fibrin matrix. Blebbistatin (85 µM) is used to inhibit cell contraction, resulting in matrix recovery to a reference state for DVC. Cell-induced displacements during migration are computed (Fig. 4.9a), but tractions are not computed due to the unknown constitutive properties of the inhomogeneous matrix after proteolytic degradation (shown in Fig. 4.9b).

Throughout the cell migration experiment shown here, the cell occupies a void space in the matrix. While the cell body is primarily contained within the void space, thin cellular protrusions extend into the matrix fibers to connect the cell to the matrix in a similar manner to the dividing cells described in Chapter 3. Over a period of ~ 3 hours, the cell moves ~ 100 µm from one corner of the matrix void to another. While migrating, the cell applies matrix displacements at the leading edges of the protrusions that connect the cell to the matrix. While maximum displacement magnitudes are large (~ 3 µm), the displacements are localized to individual cell protrusions, indicating that the cell stores minimal strain energy in the matrix while migrating. This minimal strain energy observation is consistent with the previously described finding that cells only migrate within the matrix when void spaces through which the cell can maneuver are present. Other studies have made similar observations and have

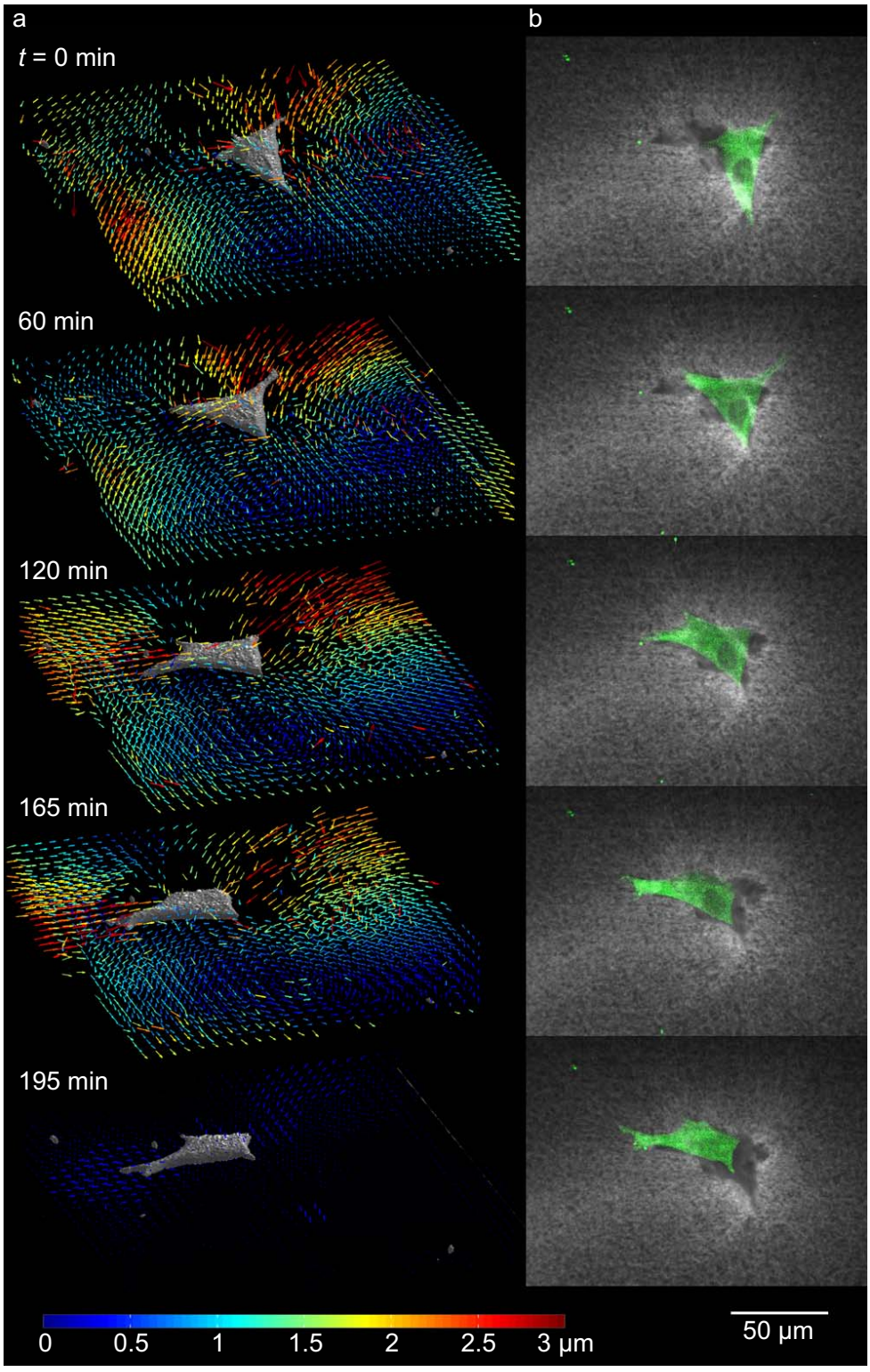

Figure 4.9: In a 3D matrix, a cell migrates through matrix void spaces. (a) The 3D displacements applied by the cell to the matrix are localized at the leading edges of cellular protrusions. (b) The movement of the cell (green) is within a matrix void space. The void is observed by a dark spot in the images of fluorescently labeled matrix (gray). The final set of displacements ($t = 195$ min) are computed after injection of blebbistatin to inhibit cell contraction.

concluded that cells prefer to migrate either through “tracks” formed by fiber degradation or through large matrix pores [93]. Future work could apply the 3D TFM technique developed here to quantify the tractions and strain energy applied by migrating cells to the matrix. Such a study could lead to conclusions on the matrix density and stiffness through which cells can migrate most (or least) efficiently.

4.6.2 Advanced Cell and Matrix Labels

With commercial confocal microscopes being sold today with up to six or more laser channels, imaging a combination of matrix and cell labels is possible. Multi-channel imaging would result in a vast array of chemical, structural, and mechanical information in a single experiment. In the experiments described in this chapter, the fibrin matrix was fluorescently labeled with a dye that covalently attached to fibrinogen. Fluorescence images of the matrix collected with confocal microscopy allowed for direct visualization of the matrix microstructure. In addition, the fluorescence images provided a random, high contrast pattern for displacement computation by DVC. Further information could be gained by employing different fluorescence labels. For example, fluorescent probes that report proteolytic degradation of matrix fibers have been developed and applied to cells invading a 3D collagen matrix [103]. Combining such probes with the 3D TFM approach described here would result in a single experiment capable of quantifying the matrix fiber displacement, alignment, and degradation during cell invasion.

These experiments used cells labeled with GFP attached to actin, resulting in fluorescence images of the actin stress fiber structures within the cells. Additional labels for proteins associated with cell invasion would yield more information about how the cell interacts with its surroundings during invasion. Proteins of interest could include cell-matrix adhesion proteins like vinculin, enzymes associated with matrix degradation like matrix metalloproteinases, or kinases associated with molecular pathways of stress fiber formation. Together with detailed matrix imaging and use of specific cell labels, 3D TFM has the potential to reveal the mechanisms associated with cell migration in an even greater level of detail.

Chapter 5

Constitutive Modeling of Cell Mechanosensing in a Three-Dimensional Matrix

A large number of studies have characterized a cell's response to the stiffness of its environment. It has been shown that substrate stiffness in part directs migration [39], stem cell differentiation [2], lamellipodia formation [104], regulation of the cell cycle [105], proliferation [106], adhesion [107], and more [3]. In addition to these biological behaviors, the stiffness of the environment controls mechanical cellular processes. For instance, cells have been shown to contract more when cultured on a stiff substrate as compared to a more compliant substrate [37, 39, 108], yet the mechanism for the change in contractile behavior remains unknown. Further examination of cellular response to forces may provide useful clues to the mechanical mechanisms associated with a cell's response to the stiffness of its environment.

While fewer studies have focused on sensing forces than sensing substrate stiffness, evidence exists for direct cellular sensing of physical forces. An early study demonstrated that physical forces influence migration by observing a change in the direction of a cell migrating on a flat substrate after inducing local deformation in the substrate [39]. Other work has cultured cells on compliant substrates with square protein layers to which the cells adhere. The resulting square cells apply the largest tractions to the substrate at the corners of the square shape, and these corners correspond to locations of increased proliferation [40] and lamellipodial activity [109]. Global (as opposed to local) stresses have also been shown to control cell

behavior. Cells cultured in an environment under cyclic tensile loading have been shown to align either parallel to [110] or normal to [111] the loading direction depending on the loading rate [112]. Because cells apply greater tractions to stiffer substrates [37, 39, 108], some have claimed cells can be thought of as "displacement controlled" machines that primarily sense and apply displacements. Various researchers have attempted to demonstrate the displacement control hypothesis [108, 113, 114], but no underlying mechanism for displacement control has yet been uncovered. Further studies on cell response to mechanical forces will answer fundamental questions related to mechanotransduction. Developing a better understanding for the mechanisms that control cell mechanosensing will require experimental and theoretical approaches designed to apply and detect displacement and stress fields near a cell. The three-dimensional (3D) traction force microscopy (TFM) approach described in Chapter 2 of this thesis forms a useful tool for studying displacement and stress fields near cells in a 3D matrix.

Here, the ability of cells to interact with one another by applying physical forces is studied. Previous work has predicted cell alignment along linear chains due to cell–cell mechanical interactions through a compliant substrate [115]. Additionally, a previous study used traction force microscopy to experimentally demonstrate cell mechanical interactions on a two-dimensional substrate [116]. However, no studies have investigated cell mechanical interactions through a biologically relevant 3D matrix. The objective of this chapter is to develop a constitutive model for the fibrous 3D matrix that is consistent with experimental data and creates a framework for future studies on cell mechanosensing. The constitutive model is used to describe mechanical cell–cell interactions in a 3D matrix, and it predicts a critical distance for cell mechanosensing. The chapter starts with experimental observations of cells sensing their neighbors through physical forces applied to the matrix. The distance over which cell-induced matrix displacements propagate is then measured from experimental data obtained with 3D TFM. A finite element (FE) model is developed to describe the experimentally observed constitutive behavior of the fibrin matrix. Finally, the FE model is applied to predict a critical

distance for cell sensing.

5.1 Examples of 3D Cell Mechanosensing

When cultured in a 3D matrix, cells respond to their mechanical environment by sensing both the matrix stiffness and neighboring cells that apply forces to the matrix. Chapter 4 describes how single cells begin to invade a 3D matrix by locating a region where minimal tractions are required for spreading. The minimal traction invasion mechanism assumes no other cells are present in the matrix, and therefore it depends only on the local density and modulus of the matrix. Since cells have been shown to sense and respond to physical forces, it is hypothesized here that the transmission of force through the matrix also controls cell spreading. Experimental examples of cell mechanosensing during spreading in a 3D matrix are given in this section.

Experiments to investigate cell spreading were conducted in a 3D fibrin matrix (3 mg/mL fluorescently labeled fibrinogen mixed with 20 U/mL thrombin, prepared as described in Chapter 2) using 3T3 fibroblast cells at a concentration of 3000 cells per 20 µL fibrin. Volume stacks of the cells and fibrin matrix were collected using a Swept Field confocal microscope (Nikon Instruments, Melville, NY) with a $40\times$ water immersion objective as described in Chapter 2. Imaging began one hour after seeding the cells in the matrix and continued every hour for $\sim$ 20 hours. Maximum intensity projection images of a pair of cells from a typical spreading experiment are shown in Fig. 5.1. Spreading begins $\sim$ 6 hours after polymerization of the fibrin matrix. The rounded cells, with an initial diameter of $\sim$ 20 µm and separation of $\sim$ 100 µm, spread by extending protrusions toward one another until the protrusion of one cell contacts the neighboring cell (Fig. 5.1, $t = 12$ hr). Since the centers of these spreading cells are separated by a distance of only 5 cell diameters, it is feasible that the cells spread toward one another by following mechanical cues—forces—from their neighbors.

Mechanical interactions between neighboring cells do not always involve cells spreading

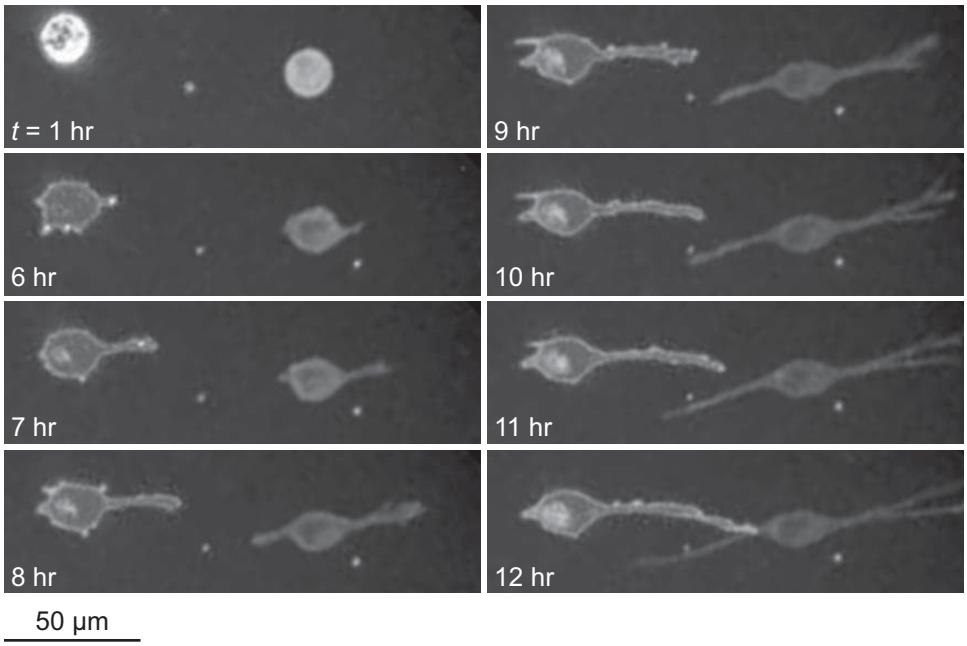

Figure 5.1: Fibroblasts are imaged over time during spreading in a 3D fibrin matrix. The matrix was polymerized at $t = 0$ hr, and confocal imaging began at $t = 1$ hr. Maximum intensity projection images of a pair of spreading fibroblast cells labeled with GFP–actin are shown. Spreading is observed to begin ~ 6 hr after fibrin matrix polymerization, and a pair of neighboring cells, separated by < 100 μm, extend protrusions toward one another.

until they contact one another as in Fig. 5.1. By applying mechanical forces and excreting proteolytic enzymes, spread cells rearrange their surrounding matrix [93, 94]. If a pair of cells applies opposite tensile forces to the matrix, each along a line connecting the cells, the matrix undergoes local deformation with fibrous "tethers" forming between the cells (Fig. 5.2). Such tethers, observed with confocal microscopy of a labeled fibrin gel as described in Chapter 2, can propagate over long distances of nearly 10 cell diameters (Fig. 5.2b). Since tether formation requires that the cells apply force to the matrix, these tethers may be a mechanism by which cells interact with one another mechanically in a 3D fibrous matrix.

The examples of cell spreading (Fig. 5.1) and tether formation (Fig. 5.2) in a 3D matrix motivate the need for a constitutive model that captures the properties of the matrix at the length scale sensed by the cell. The description in Chapter 4 that cells invade at locally less dense regions in the matrix requires matrix inhomogeneities for invasion to commence. Additionally, the matrix tethers formed between neighboring cells require nonlinear, localized deformations.

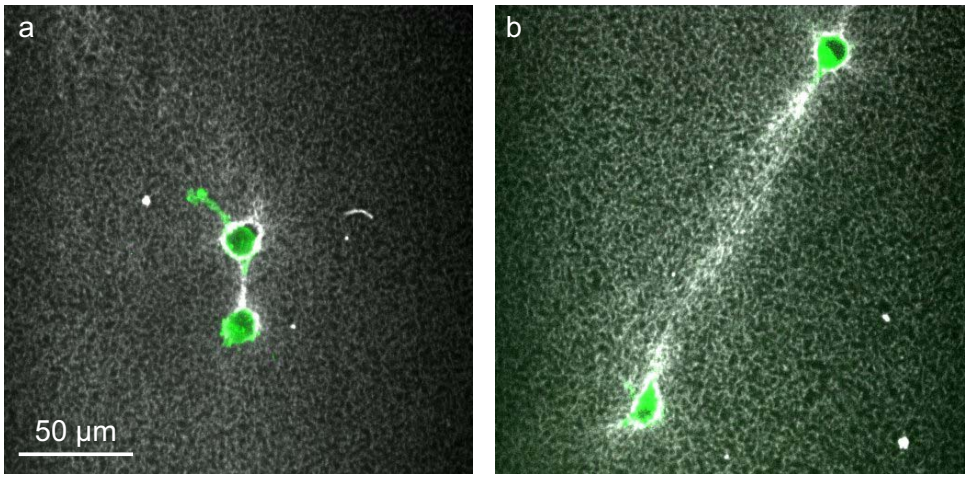

Figure 5.2: Pairs of 3T3 fibroblasts cells (fluorescently labeled with GFP–actin) form tethers in the matrix (gray) after spreading. The cells are imaged ~ 24 hr after seeding in the fibrin matrix to allow time for spreading and rearranging of matrix fibers. The tethers can act over a short ranges of ~ 2 cell diameters (a) or over longer ranges of ~ 9 cell diameters (b).

Thus, a nonlinear, inhomogeneous constitutive model is required to capture the mechanics of cell invasion and mechanosensing in a fibrous matrix.

5.2 Propagation of Displacements Through the Matrix

Developing a constitutive model for cell–matrix interactions first requires analysis of how cell-induced displacements, strains, and stresses propagate through the matrix. To simulate how a cell applies displacements to the surrounding matrix, a simple model is created (Fig. 5.3). The model primarily analyzes the scaling of displacements through the matrix. Strains and stresses can easily be computed from the model by computing the gradient of the displacements. The model treats the cell body as a contracting ellipsoid that induces displacements in the surrounding matrix according to Eshelby's solution for an inclusion under a transformation strain in a homogeneous, linear, elastic continuum [117]. For a spherical inclusion of radius a under isotropic, volumetric transformation strain, the nonzero components of the strain tensor are written $\varepsilon_{ij}^T = \varepsilon^T \delta_{ij}$. For this case, the displacement components u_i in the surrounding

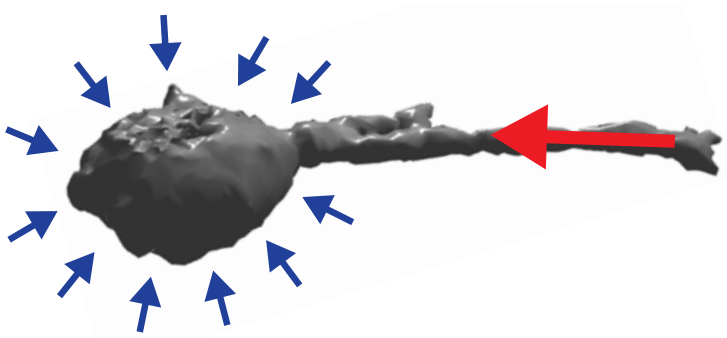

Figure 5.3: A simple model for a cell contracting in a 3D matrix. The cell body is treated as an ellipsoid undergoing a contractile eigenstrain (blue arrows, left). Displacements around the cell body are computed from Eshelby's solution (Eq. (5.1)) and scale as $u \sim 1/r^2$. The leading edge of a cellular extension is approximated as a point force applied by the cell to the matrix (red arrow, right). Displacements for a point force (Eq. (5.2)) scale as $u \sim 1/r$.

continuum induced by the transformation strain ε^T simplify to

$$u_i = \frac{1+\nu}{1-\nu} a^3 \varepsilon^T \frac{x_i}{3r^3}, \tag{5.1}$$

where ν is Poisson's ratio and $r = (x_i x_i)^{1/2}$. In Eq. (5.1) displacements scale with position as $1/r^2$. For non-spherical ellipsoids and non-uniform contractions, the scaling between displacements and position remains the same, $u \sim 1/r^2$.

In addition to applying displacements to the matrix around its body, the cell applies point-like forces at the tips of thin extensions. The displacements u_i due to a point force F_i in an infinite, linear, elastic continuum are given by [118]

$$u_i = \frac{1+\nu}{8\pi E\,(1-\nu)\,r} \left[\frac{F_k x_k x_i}{r^2} + (3-4\nu)\,F_i \right]. \tag{5.2}$$

For a point force the displacements scale differently than the $1/r^2$ scaling in the Eshelby problem. Instead, the displacements induced by a point force scale according to $u \sim 1/r$. Note however that for a dipole with equal and opposite forces near to one another in a continuum, the principle of superposition can be used to show that far from the dipole displacements scale as $u \sim 1/r^2$, which is consistent with the fact that a contracting sphere is mechanically equiv-

alent to three contracting dipoles orthogonal to one another.

The propagation of displacements through a 3D matrix is quantified by analyzing experimental data. 3D displacements induced by cells spreading in a fibrin matrix (3 mg/mL fibrinogen) are measured as described in Chapter 2 and plotted in Fig. 5.4a,c. The scaling of the matrix displacements over distance is quantified by choosing linear paths away from the cell and plotting displacements along these paths. Since the cell body is predicted to induce a displacement field similar to a contracting spheroid, displacements along a path starting at the center of the cell body are plotted for further analysis (Fig. 5.4b). Similarly, displacements induced by a cellular extension, which is predicted to apply a point-like force to the matrix, are plotted along paths originating from the leading edge of the extension (Fig. 5.4d). To assess how displacements propagate through the matrix, displacements induced by both the cell body and extension are fit to the curves $u = A/r + B$ and $u = C/r^2 + D$ where A, B, C, and D are constant fitting parameters. From the fitting it is found that displacements scale as $u \sim 1/r$ near both the cell body and the cellular protrusion.

The scaling of displacements with increasing distance is further evaluated by analyzing the displacement data along linear paths away from either a cell body or cell extension using data from multiple different experiments and time points. For all experiments described here, cell-induced matrix displacements are measured as described in Chapter 2 for fibrinogen concentrations of 3–4.5 mg/mL. Displacements induced by six different cells were analyzed here. To increase the sample size, up to three different linear paths are chosen for displacements measured at various different time points. Displacement magnitudes are fit to the curves $u = A/r + B$ and $u = C/r^2 + D$, and the mean square error between the experimental data and the fitting curves, $\varepsilon_{1/r}$ and ε_{1/r^2} is computed. The ratio of the errors, $\varepsilon_{1/r}/\varepsilon_{1/r^2}$, is computed for each linear path, and results are shown in the histograms in Fig. 5.5 and summarized in Table 5.1. An error ratio less than unity indicates that the data fits better to $u \sim 1/r$. For displacements induced by either the cell body or a cell protrusion, mean error ratios are under 0.8, indicating the data agrees with the trend observed in Fig. 5.4 that displacements scale as

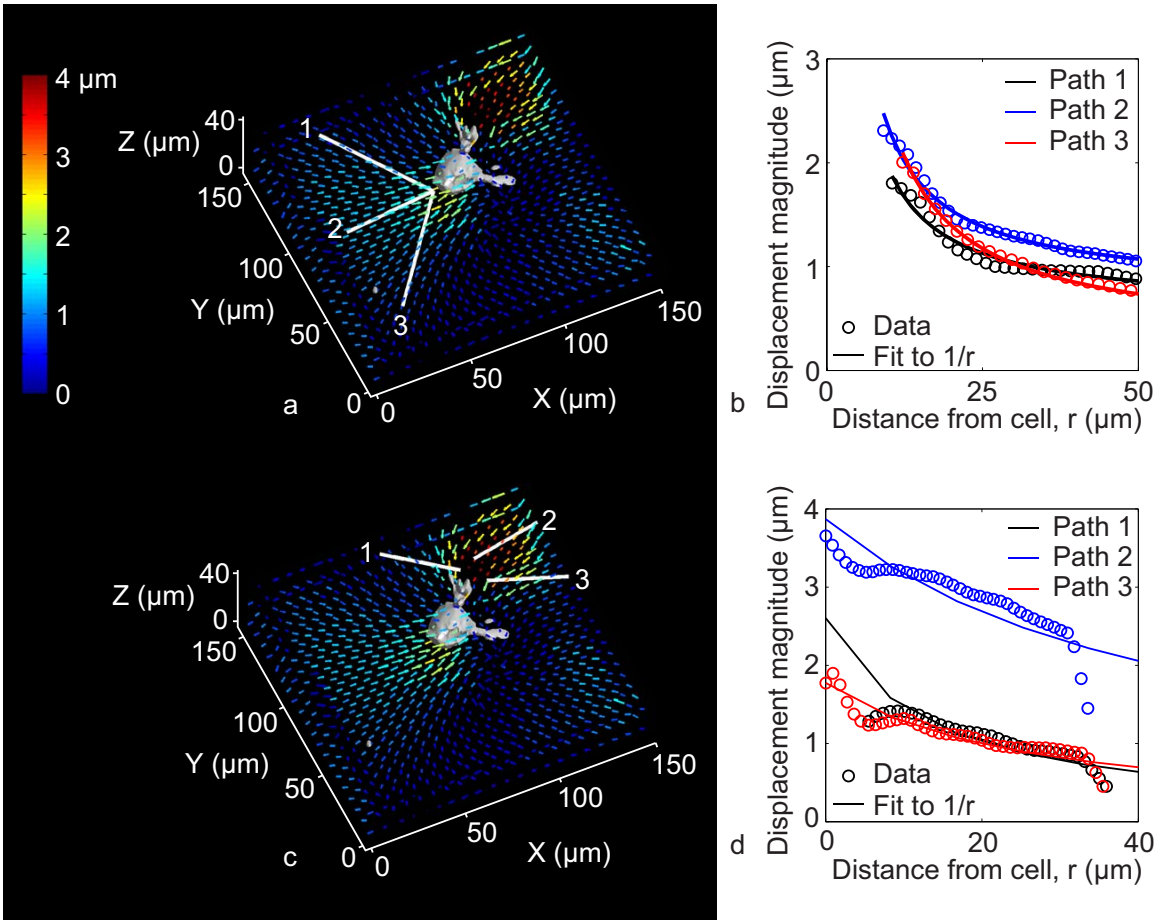

Figure 5.4: The scaling of cell-induced matrix displacements is quantified by plotting displacements along a linear path away from the cell. (a) To quantify displacements near the cell body, three paths are chosen proceeding outward from the center of the spherical cell body. The 3D matrix displacements (arrows) are plotted along the three paths in (b). The data is fit to the curve $u \sim 1/r$ with good agreement. (c) Paths are also chosen near a cellular protrusion for analysis. Displacements along the three paths near the cell protrusion are shown in (d), again with a fit to $u \sim 1/r$.

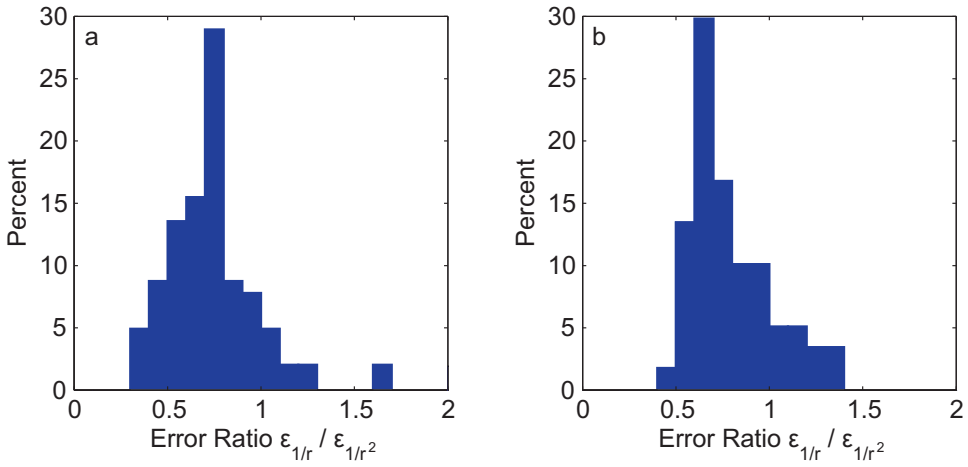

Figure 5.5: Displacement magnitudes along linear paths near the cell body and the leading edge of a cellular protrusion are fit to the curves $u = A/r + B$ and $u = C/r^2 + D$. Mean square errors between the experimental data and the fits, $\varepsilon_{1/r}$ and ε_{1/r^2} are computed. Histograms of the dimensionless error ratio $\varepsilon_{1/r}/\varepsilon_{1/r^2}$ are plotted for displacements near the cell body (a) and protrusion (b). The number of paths n for which the error ratio is computed is $n = 104$ for displacements induced by a cell body (a) and $n = 59$ for displacements induced by a cell protrusion (b).

Table 5.1: Summary of the error ratio in fitting the scaling of cell-induced displacements, $\varepsilon_{1/r}/\varepsilon_{1/r^2}$. "% < 1" indicates the percentage of the error ratios less than 1.

Error Ratio, $\varepsilon_{1/r}/\varepsilon_{1/r^2}$	Mean	Stand Dev	% < 1	n
Cell Body	0.76	0.30	88%	104
Cell Protrusion	0.79	0.22	83%	59

$u \sim 1/r$. As indicated in Table 5.1 and Fig. 5.5, over 80 percent of the error ratios are below 1, further emphasizing the $u \sim 1/r$ scaling.

The $1/r$ scaling for displacements surrounding the cell body contradicts the prediction that the Eshelby solution for a contracting ellipsoid in a linear, elastic continuum appropriately models the cell body. There are two possible mechanical explanations for the discrepancy between the Eshelby solution and the experimental data. The first possible explanation is that the cell body does not contract uniformly, resulting in local fluctuations of tractions over the cell body. While inhomogeneous tractions are possible—and even likely (see Fig. 4.5 in Chapter 4)—force equilibrium dictates that tractions applied by a rounded cell must sum to zero.

Therefore, even when the cell applies inhomogeneous tractions to the matrix, the tractions are applied in opposite directions and separated by a small distance (the cell diameter), similar to a force dipole. As previously described, a force dipole gives the relationship $u \sim 1/r^2$, and not the $u \sim 1/r$ observed here. Thus, a more likely explanation for the discrepancy comes from the assumption that the matrix is homogeneous, linear, and elastic.

The observation that cell-induced displacements in the fibrin matrix do not scale according to theories developed for a homogeneous, linear, elastic material motivates the need to develop a more accurate mechanical model for the matrix. Moreover, the alignment of matrix fibers to form tethers between neighboring cells (Fig. 5.2) requires nonuniform, localized matrix displacements that cannot be captured with a homogeneous, linear, and elastic constitutive model. The goal of developing a constitutive model for the fibrin matrix extends beyond mechanically describing the deformations within the matrix. A more accurate model will predict the local matrix stiffness sensed by the cell, leading to a more complete understanding of processes that depend on matrix stiffness such as migration, differentiation, morphology, and mechanotransduction [3].

5.3 A Finite Element Model for the Fibrin Matrix

While the fibrin matrix is initially modeled in Chapter 4 as a homogeneous, isotropic, linear, elastic continuum, the large strains applied by the cell to the matrix ($\sim 10\%$) create nonlinearities. In addition, the fibrous structure of the fibrin matrix creates anisotropic aligned fibers and other inhomogeneities. Thus, the fibrin matrix fails to meet the assumptions required to apply linear elasticity. The inability of linear elasticity to match the constitutive properties of the matrix is the cause for the observation that displacements induced by a rounded cell scale as $u \sim 1/r$ instead of $u \sim 1/r^2$ (Fig. 5.4). Thus, nonlinear continuum material models are initially applied. Appendix A gives details on two particular models, the Neo-Hookean model (used for rubbery materials) and the Blatz–Ko model (used to simulate compressible foams).

Both of these models fail to capture the $1/r$ scaling, and they further do not allow for the localized displacements required for matrix tethers to develop between pairs of cells (Fig. 5.2). More complicated strain energy functions that better capture the behavior of rubbers like the Mooney–Rivlin model [119] or the Arruda–Boyce model [120] do not change the $1/r^2$ scaling (data not shown). Similarly, forms of the Blatz–Ko strain energy that use a summation of additional fitting terms do not change the displacement scaling (data not shown). Thus, while more complex strain energy functions could potentially mimic the $1/r$ scaling of displacements, the fibrin matrix cannot be simulated with previous well-established strain energy functions for a homogeneous continuum.

A mechanical model that uses a structure of links would better simulate the microstructure of the fibrin matrix studied here. A structural model could account for reorganization and alignment of individual fibers, allow for stress to be carried along a chain of fibers, and accommodate statistical fluctuation of fiber length and stiffness. Additionally, a structural model is highly visual and connects the length scale of the microstructure to the length scale of the cell. While fiber models previously have been developed, they have primarily predicted the response to a simple uniaxial [121] or shear [122, 123, 124] loading. While one study modeled a structure of spring-like elements around a contracting sphere, it did not account for inhomogeneities in element length, material stiffness, or nodal locations [125]. Here, a 2D structural model is created in the commercial FE software Abaqus (Dassault Systemes, Waltham, MA) using structural truss elements. The elements are connected to one another in a "boxed x" pattern as shown in Fig. 5.6. The "boxed x" connectivity is chosen because it offers a nearly isotropic response of the bulk material to an applied force. Similar to a thin fiber of fibrinogen in a fibrin matrix, the truss elements support only axial forces with no resistance to bending.

To match the fibrin matrix, constitutive properties for the truss elements should match the stress–stretch relationship of an individual fibrinogen fiber. While much previous work has studied the constitutive properties of bulk material, relatively little work has focused on the stress–stretch relationship of a single fiber. For bulk collagen, it has been shown that stress

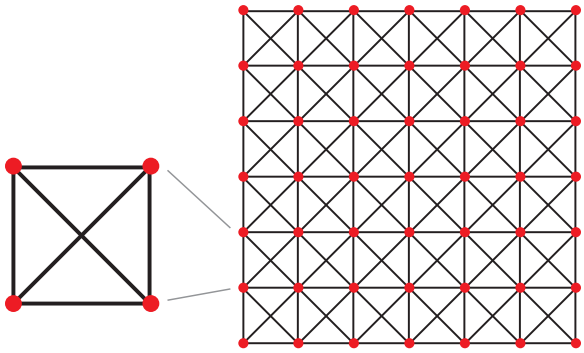

Figure 5.6: An array of nodes (red circles) are connected using truss elements (black lines) as shown to form a structural model for the fibrin matrix.

increases as the square of strain [126], and similar quadratic stress stiffening has been demonstrated for bulk networks of actin, fibrin, and vimentin [127]. The constitutive properties of individual fibers are more difficult to measure, but some previous work has applied linear, elastic beam theory to estimate Young's modulus of a single fiber in a crosslinked fibrin matrix to be ~ 15 MPa [128]. This measurement of Young's modulus is only an approximation, however, because the use of linear beam theory for a long polymer fiber may not be appropriate. A potentially better model would be a wire or rope which resists transverse deformation only through axial tension. In addition, the measurement of Young's modulus reported force and displacement only at a single point and did not fit the data to a curve, preventing further analysis such as whether linear beam theory is appropriate or whether strain stiffening occurs.

With the lack of direct experimental data, previous studies on fibrin networks have assumed the individual fibers behave according to the worm-like chain (WLC) model [124, 127]. In the WLC model, strain stiffening occurs as a result of straightening fibers that are initially bent due to entropic forces. As the individual fibers straighten, their resistance to elongation increases, resulting in apparent strain stiffening. Indirect experimental evidence for WLC-like behavior in individual fibrin fibers comes from an experiment that measured the modulus of a fibrin gel under large strains [129]. The authors argued that under a large strain, the fibers fully aligned parallel to one another, resulting in a direct correlation between the constitutive properties of the bulk material and the individual fibers. In this experiment, it was found that

individual fibers match the force–extension relationship given by the WLC model. It has previously been shown [130] that for the WLC model the force F is related to the displacement x by the following approximate equation:

$$\frac{FL_p}{k_BT} = \frac{x}{L} + \frac{1}{4}\left[\left(1 - \frac{x}{L}\right)^{-2} - 1\right], \tag{5.3}$$

where L_p is the persistence length, k_BT is the thermal energy, and L is the fully straightened chain length. As $x \to L$, the force goes to infinity. Thus, the WLC model assumes the fiber cannot extend past the fully straightened length. Eq. (5.3) can be rewritten in terms of a stretch ratio λ by defining $\tilde{x} = x/L$ and writing the stretch ratio as follows:

$$\lambda = \frac{\tilde{x}_{\text{current}}}{\tilde{x}_{\text{initial}}}. \tag{5.4}$$

Also note that the maximum stretch ratio $\lambda_{\max}$ can be written

$$\lambda_{\max} = \frac{1}{\tilde{x}_{\text{initial}}}. \tag{5.5}$$

Combining Eqs. (5.3), (5.4), and (5.5) gives

$$\frac{FL_p}{k_BT} = \frac{\lambda}{\lambda_{\max}} + \frac{1}{4}\left[\left(1 - \frac{\lambda}{\lambda_{\max}}\right)^{-2} - 1\right]. \tag{5.6}$$

Application of the WLC model requires knowledge of two constants, the persistence length L_p and the maximum possible stretch ratio $\lambda_{\max}$. Depending on the initial fiber length, the WLC force–distance curve can change significantly. For example, changing $\lambda_{\max}$ by a factor of 2 from 5 to 2.5 can result in a factor of ~ 5 increase in the resulting force (Fig. 5.7a). For single fibrin fibers, stretch ratios > 4 have been reported [131], so a $\lambda_{\max}$ of ~ 5 is an appropriate choice.

The constitutive properties of the individual fibers are incorporated into the structural FE model by inputting the nominal (engineering) uniaxial stress–strain data using the Marlow

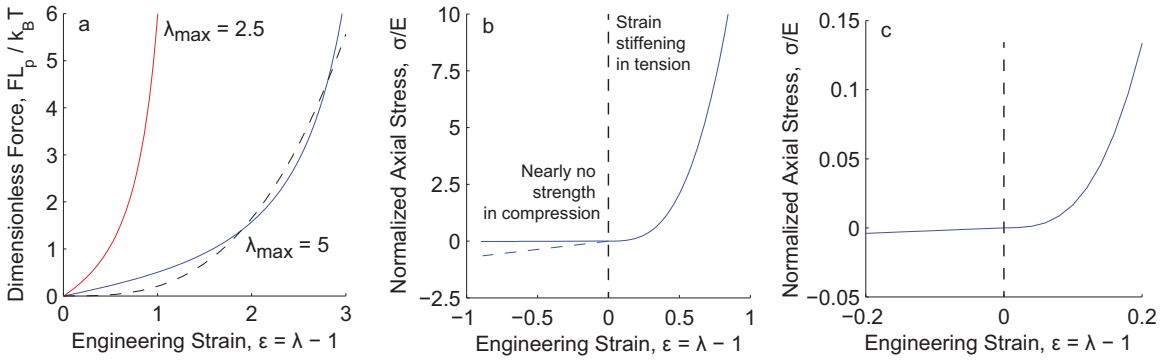

Figure 5.7: (a) The force–stretch relationship given by the worm-like chain model (Eq. (5.6)) is plotted for $\lambda_{\max} = 2.5$ and 5 (solid lines). The curve for $\lambda_{\max} = 5$ is fit to $F = C\varepsilon^3$ (dotted line), where C is a constant and ε is the engineering strain, $\varepsilon = \lambda - 1$. (b) Each element in the FE model has a tensile stress–strain relationship that increases according to $\sigma \sim \varepsilon^3$. To simulate the effect of fiber buckling, the elements have almost no strength in compression ($\varepsilon < 0$, solid line). For some studies, compression strength is included using a linear stress-strain relationship with constant slope ($\varepsilon < 0$, dotted line). (c) The stress–strain relationship of (b) is plotted for engineering strains ranging from -0.2 to 0.2, which are typical strains encountered in the simulations.

material model in Abaqus. While the Marlow model in principle allows for inputting any stress–strain relationship, smoothness is required for convergence. To increase the smoothness of the Marlow model, a cubic function replaces the WLC model in tension (5.7b,c). As shown in Fig. 5.7a (dotted line), the cubic function fits to the WLC model for $\lambda_{\max} = 5$ fairly well, except near the origin where the slope is closer to zero to increase the smoothness when approaching the origin from the right. Preliminary studies showed that using linear, WLC, or a polynomial (quadratic or cubic) stress–strain relationship in tension had minimal effect on the resulting displacements. The insensitivity to the stress stiffening behavior agrees with a previous study that used a structural model of a contracting circle that showed no difference between a linear and stress stiffening constitutive relationship [125].

Under compression, the fibers are expected to buckle, and previous studies have highlighted the importance of considering fiber buckling by showing buckling of fibrous networks can cause negative effective shear stiffnesses [122] and negative normal strains [124] under shear loading. To simulate fiber buckling under compression, the elements in the FE model are chosen to have nearly no resistance to compression. The lack of compression resistance is implemented

into the model by assigning a linear stress–strain behavior in compression with a slope equal to the slope in tension at $\varepsilon = 1\%$ (Fig. 5.7c, $\varepsilon < 0$). Thus, for any tensile strains greater than 1%, the material appears significantly stiffer in tension than in compression, which computationally mimics the effect of stress fiber buckling under compression. While the value of 1% is chosen arbitrarily, increasing or decreasing the slope in compression results in a negligible difference in displacement and strain computation. The stress scales linearly with both the normalization parameter E and the cross-sectional area of each element A. Since only kinematics (displacements and strains) are investigated through displacement boundary conditions only, the choice of the constants E and A have no effect on the results.

The model is designed to allow for randomness in the location of the nodes and the relative modulus of the fibers by multiplying the stress–strain relationship for each element by some random number. Preliminary simulations are performed to quantify the effect of randomness in the nodal positions and element moduli. Since the model uses structural elements that support only uniaxial forces, an axisymmetric geometry cannot be used; instead a 2D geometry is considered here as a model system. A $100d \times 100d$ region consisting of 101×101 nodes separated by a distance d connected with truss elements using the "boxed x" geometry described previously is used (Fig. 5.8a). A group of nodes in the center of the model is translated upward a distance $3d$ to simulate a point-like force applied by a cell. A symmetry boundary is placed at the bottom of the domain to mimic two cells separated by $100d$ applying equal and opposite forces. Positive logarithmic strains in each element—computed by taking the logarithm of the stretch ratio λ—are a useful strain measure for these elements which support only uniaxial tension. Logarithmic strains are plotted in Fig. 5.8. For a distribution of nodes with uniform spacing (Fig. 5.8b), tensile strains in each element with a magnitude of $\sim 5\%$ propagate to the symmetric bottom boundary, a distance of $50d$ away. The propagation distance of $50d$ is large compared to the $3d$ translation applied to the $2d \times 3d$ group of nodes. Maximum strains are found to be $\sim 20\%$ at the point of loading. Above the loading position the elements are under compression. Because the elements have almost no strength in compression (see Fig. 5.7b),

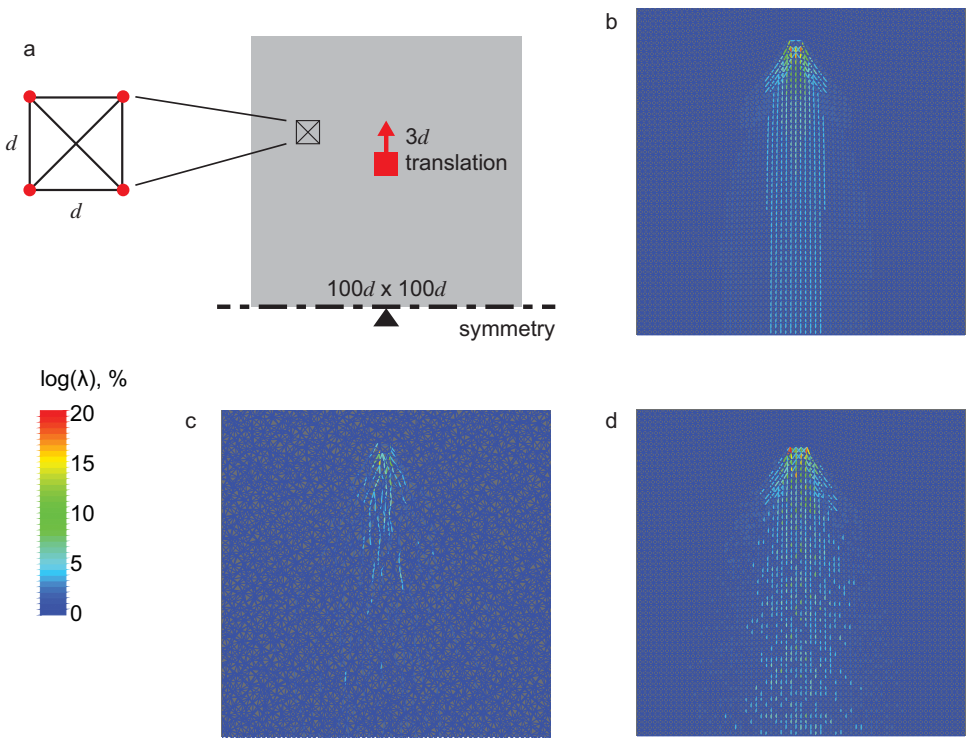

Figure 5.8: (a) A structural model is created to simulate each fiber of the fibrin matrix. The "boxed x" geometry is used to connect nodes in a $100d \times 100d$ square region, where d is the nodal spacing. A symmetry boundary condition is used at the bottom of the region with the central bottom node pinned to prevent rigid body translation. A group of 6 nodes in the center of the model is translated upward $3d$. Logarithmic strains in each element are plotted in a $60d \times 60d$ region at the bottom and center of the model. Three "randomness" conditions are considered. The first condition (b) uses no randomness in either the node positions or element stiffnesses; the second condition (c) adds randomness to the position of each node to simulate a random mesh of fibers; and the third condition (d) adds randomness in the stiffness of each element.

compressive strains are not plotted here.

Randomness in the nodal positions and the element stiffnesses can more realistically mimic the random fibrin matrix. Randomness in the nodal positions is included by adding a random variable taken from a uniform distribution between $-d/2$ and $d/2$. The same boundary conditions are applied as shown in Fig. 5.8a, and logarithmic strains are shown in Fig. 5.8c. The randomness in the nodal positions creates a meshwork (observe the blue fiber network in Fig. 5.8c) that is more representative of the fibrin matrix than a uniform mesh (Fig. 5.8b). However, strains propagate in a more random, less aligned pattern, due to the fact that before loading fibers are not aligned with the loading direction. Nevertheless, nonzero strains of $\sim 2\%$ are observed at the lower symmetric boundary, indicating that the strains propagate

over a long range of $50d$. In the fibrin matrix, in addition to randomness in the nodal positions, each fibrin fiber would likely have a slightly different stiffness. Randomness in the stiffness of each fiber is implemented by creating a different material model for each element. Every material model follows the stress–stretch curve in Fig. 5.7b, but the relative stiffness of each element is modified by multiplying the stress–stretch by a uniform random variable between 0.5 and 1.5, representing a change in elemental stiffness, between 50% and 150%. The resulting strains of the random element stiffness simulation (Fig. 5.8d) shows a behavior similar to the simulation with constant element stiffness (Fig. 5.8b). Displacements propagate along the fibers and carry strains of $\sim 5\%$ to the lower boundary, a distance $50d$ away. As expected, random element stiffnesses induce some fluctuation of the strain in each element, but the magnitude and spatial extent of the fluctuations is smaller than for the random nodal positions (Fig. 5.8c). Using a combination of randomized nodal locations and random element stiffnesses results in elemental strains similar to those shown for randomized nodal locations only (Fig. 5.8c), indicating that nodal randomness has the most significant effect on the strain within the individual elements. Elemental randomness was further simulated by removing a small percentage (~ 5–10%) of the elements and solving for the strains in each element. Again, there was little difference compared to Fig. 5.8c.

5.3.1 Displacements around a Contracting Circle

Similar to the continuum models in Appendix A, the structural model for the fibrin matrix is used to simulate contraction of a circle (Fig. 5.9a) for comparison to the 3D TFM data around a rounded cell (Fig. 5.4). The model uses a circle of radius a in the center of a $20a \times 20a$ square region. 200×200 nodes within the region are connected using the "boxed x" connectivity (Fig. 5.6), with the exception that no elements exist inside the circle. To simulate the contraction of a circular cell, an inward displacement of $0.15a$ is applied to each node along the boundary of the circle. Periodic boundary conditions are applied at the edges of the square region. The model is solved in Abaqus, and displacement magnitudes are shown in Fig. 5.9b. Maximum

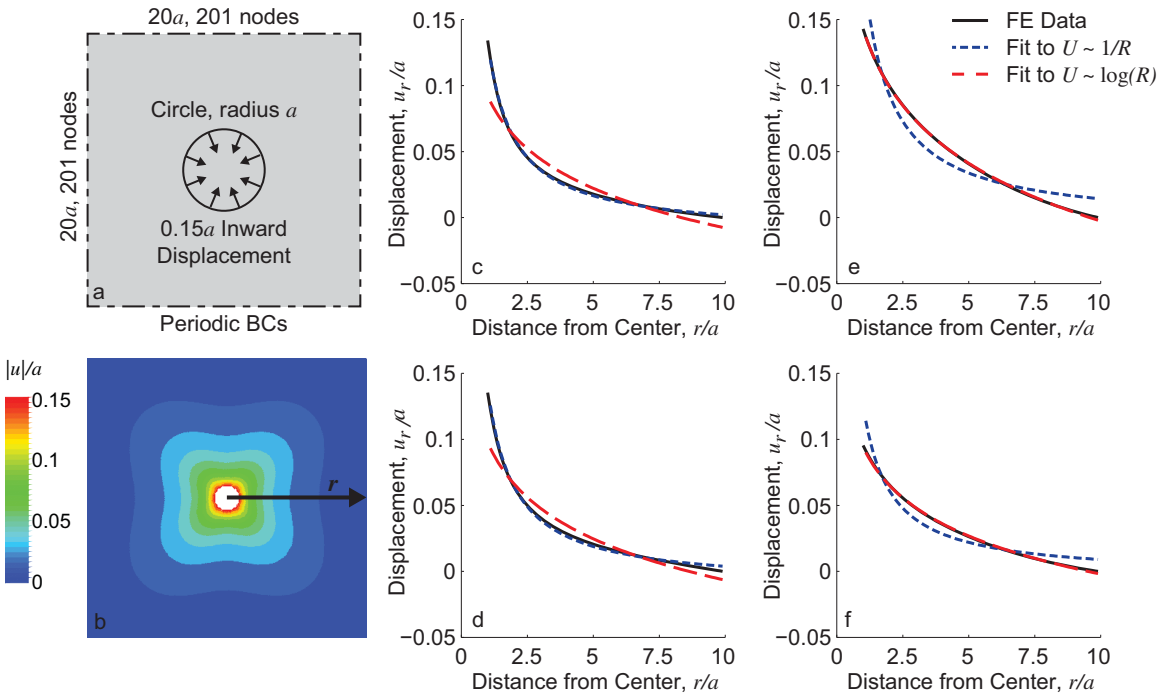

Figure 5.9: (a) The structural FE model with the "boxed x" element connectivity is used to measure the displacements surrounding a contracting circular region. A circle in the center of the model with a radius a is used to simulate a contracting cell by applying a $0.15a$ inward displacement to each node on the boundary on the circle. Periodic boundary conditions are used, resulting in a symmetric displacement field. 201×201 nodes are used to simulate the $20a \times 20a$ square region. (b) Displacement magnitudes show a maximum displacement of $0.15a$ at the center of the circle with displacements decreasing with distance away from the center. The dimensionless radial displacement component u_r/a is plotted against dimensionless distance from the center of the circle r/a for various material models. Displacements computed using linear and strain stiffening models that support compressive forces are shown in (c) and (d), respectively. Displacements computed using linear and strain stiffening models that do not support compression are shown in (e) and (f), respectively. The data from the FE model is fit to both $U \sim 1/R$ and $U \sim \log(R)$ where $U = u_r/a$ and $R = r/a$ are the dimensionless radial displacement and distance, respectively.

displacements of $0.15a$ occur at the boundaries of the contracting circle with a decrease in displacements away from the circle. Even though symmetric contraction of the circular region occurs, the resulting displacements are not axisymmetric, because the "boxed x" connectivity is not isotropic. The contour plot of displacement magnitudes (Fig. 5.9b) has symmetry in the horizontal and vertical directions, and additional symmetry is present along the diagonals. These directions of symmetry correspond to the directions of the elements in the "boxed x" configuration.

To evaluate the choice of elemental constitutive model, the scaling of the displacements

with distance from the center of the contractile circle is analyzed. For a linear, elastic continuum, the solution for a contracting circle can be derived from the Lamé solution for a 2D axisymmetric material [132]. The radial component of displacement u_r for a 2D axisymmetric material with a circular hole is given by

$$u_r = Ar + \frac{B}{r}, \tag{5.7}$$

where r is the radial distance to the center of the circle and A and B are constants. Since the displacements must remain finite, the constant A is equal to zero here. Thus, for a linear, elastic continuum, $u_r \sim 1/r$.

Before applying the strain stiffening constitutive relationship shown in Fig. 5.7b, the scaling of displacements in the structural model is first investigated using a linear stress–strain relationship but accounting for changes in geometry due to finite deformations. While a linear approximation would normally not be appropriate for the large deformation models like the one used in this study, the linear relationship can give useful initial insight. Dimensionless displacements $U = u_r/a$ taken from the structural finite element model with a linear constitutive model are plotted against dimensionless distance $R = r/a$ in Fig. 5.9c (solid line). The data is fit to $U \sim 1/R$, and inspection of the fit shows good agreement, indicating that the structural model behaves similar to a linear, elastic continuum. There is slight deviation at $R = 10$ between the data and the fit to $U \sim 1/R$, due to the fact that the fit assumes an infinite structure, unlike the symmetric boundary condition in the FE model. To simulate a reduction in stiffness due to fiber buckling, the model is solved again with a linear stress–strain relationship but no strength in compression (i.e., stress equals zero for any compressive strain), and results are shown in Fig. 5.9e. For the case where there is no strength in compression, the displacements deviate from the linear, elastic solution, scaling as $U \sim \log(R)$ instead of $U \sim 1/R$.

The contracting sphere is also simulated using a strain stiffening material behavior. Displacements are first computed for a strain stiffening constitutive relationship with resistance

to compression (Fig. 5.7b, dotted line). Like when using the linear relationship, the displacements scale as $U \sim 1/R$ for the strain stiffening material with strength in compression (Fig. 5.9d). However, for the strain stiffening material with nearly no strength in compression (Fig. 5.7b, solid line), the displacements scale as $U \sim \log(R)$. This result remains unchanged when choosing a path along a diagonal from the circle to the corner of the square region instead of a path along the middle of the square region. The observation that reducing the strength in compression causes the displacement scaling to diverge from the linear, elastic solution appears to be independent of other variables in the simulation. The periodic boundaries at a distance of $10a$ from the center of the contracting circle were increased to $25a$ with no change in the effect of resistance to compression. Additionally, increasing the displacement magnitude from $0.15a$ to $0.75a$ did not change the displacement scaling when using the constitutive model with or without strength in compression. Choosing a different stress–strain relationship than $\sigma \sim \varepsilon^3$ as shown in Fig. 5.7b such as $\sigma \sim \varepsilon^2$ or the WLC model similarly has no effect on the scaling of displacements. Finally, changing the randomness in the nodal positions also does not affect how the displacements scale with distance from the center of the contracting circle.

5.3.2 Displacements due to a Localized Force

Since cells apply point-like forces at the ends of thin extensions, another model for cell–matrix interaction is a point force. The 2D linear, elastic solution for the displacements $\boldsymbol{u}$ due to an upward point force of magnitude $\boldsymbol{F}$ applied at the origin of an infinite solid under plane strain conditions can be written [118]

$$\begin{aligned} u_x &= -\frac{(1+\nu)\,F_x}{8\pi E\,(1-\nu)}\left[2\,(3-4\nu)\log(r)+\cos(\theta)\right]-\frac{(1+\nu)\,F_y}{8\pi E\,(1-\nu)}\sin(\theta)\,, \\ u_y &= -\frac{(1+\nu)\,F_y}{8\pi E\,(1-\nu)}\left[2\,(3-4\nu)\log(r)-\sin(\theta)\right]-\frac{(1+\nu)\,F_x}{8\pi E\,(1-\nu)}\cos(\theta)\,, \end{aligned} \tag{5.8}$$

where $\boldsymbol{F} = [F_x, F_y]^T$, $\boldsymbol{u} = [u_x, u_y]^T$, and r and θ are standard polar coordinates with θ measured from the positive x axis. For a vertical point force (i.e., $F_x = 0$) the displacements along the

vertical line given by $x = 0$ simplify to

$$u_y = -\frac{(1+\nu)\,F_y}{8\pi E\,(1-\nu)}\left[1 - 2\,(3-4\nu)\log\left(|y|\right)\right] \tag{5.9}$$

where u_y is the displacement, and y is the upward positive distance from the point force. The displacements induced by a point force are simulated using the structural FE model. A square region using the "boxed x" connectivity with 201×201 nodes is used in the simulation. The region size is $200d \times 200d$ where d is the spacing between the nodes. An upward displacement of $1d$ is applied to the central node in the square region. Similar to the model for the contracting circle, a comparison is made between a constitutive relationship that supports compression and one that does not. Contours of displacements for the elements that support compression and do not support compression are shown in Fig. 5.10a and c, respectively. The lack of symmetry in Fig. 5.10c is a result of the choice of constitutive behavior. Since the displacement applied in the FE simulation is upward, the material above the applied displacement (i.e., for $y > 0$) is under compression. Since the elements used in the simulation shown in Fig. 5.10c do not support compression, displacements decrease more quickly than they otherwise would, resulting in displacements acting over a shorter range.

The scaling of displacements can be more easily observed by inspecting the plots of displacements along the line $x = 0$ (Fig. 5.10b,d). For the elements that support compression, the displacements below ($y < 0$) and above ($y > 0$) the origin are nearly symmetric, indicating that the material resists the applied displacement using tension and compression nearly equally. For both $y < 0$ (tension) and $y > 0$ (compression) the dimensionless displacements u_y/d fit to a logarithmic function similar to Eq. (5.9), indicating that the material behaves similar to a linear, elastic continuum. A slight lack in agreement between the data and the fit to Eq. (5.9) for $y < 0$ (and especially near $y/d = -100$) results from the fact that the constitutive model chosen stiffens in tension, and this strain stiffening has a slight effect on the results for the strains induced in this simulation ($\sim 10\%$). In contrast, for $y > 0$ the constitutive relationship

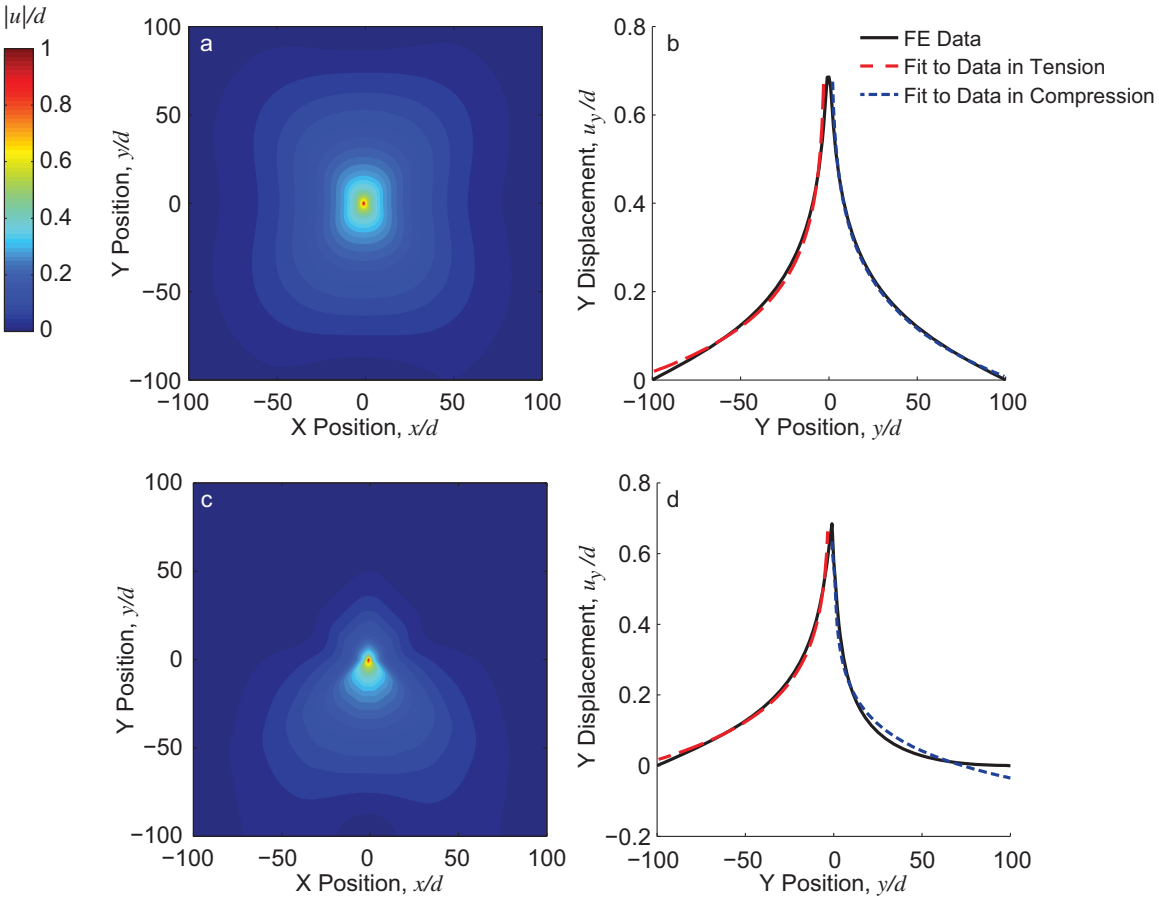

Figure 5.10: The structural FE model is used to simulate displacements induced by a point displacement in a fibrous material. 201×201 nodes with a nodal spacing of d are used to simulate a $200d \times 200d$ square region. A point displacement of $1d$ is applied at the center of the square. Using a constitutive relationship that supports compression, displacement magnitudes (a) and the vertical component of displacement u_y along the line $x = 0$ (b) are computed. Displacement magnitudes (c) and the vertical component of displacement u_y (d) are also plotted using elements that do not support compression. The line plots in (b) and (d) are fit to the function $u_y = A\log(|y|) + B$ for $y < 0$ (red dashed line) and $y > 0$ (blue dotted line) to compare to the result in Eq. (5.9).

for compression is linear, resulting in better agreement between the FE data and the fit to Eq. (5.9). For the simulation with elements that do not support compression (Fig. 5.10d), a similar match is observed between the displacements computed in the FE simulation and the fit to Eq. (5.9) for $y < 0$. However, for $y > 0$, the elements are under compression, and the displacements decrease faster than predicted by Eq. (5.9), in agreement with the faster displacement decay in Fig. 5.10c.

As in the FE simulations of the contracting circle, the simulations of the localized displacement are repeated for different conditions encountered in real fibrous matrices. Introducing nodal randomness, applying a different stress–strain relationship such as the WLC model, using a larger region (501×501 nodes to simulate a $500d \times 500d$ square) and applying a larger displacement of $5d$ instead of $1d$ were all found to not change the results of this section. Therefore, it is determined that simulating fiber buckling using elements that do not resist compression is the cause for longer range displacement propagation through the matrix.

5.3.3 Extending the Model to Three Dimensions

In two dimensions, it is found that for a contracting sphere the structural FE model predicts displacements that scale as $U \sim \log(R)$, which is the integral of scaling for a linear, elastic continuum, $U \sim 1/R$ (Eq. (5.7)). A similar relationship is expected for three dimensions, meaning that the FE model should predict displacements around a contracting sphere to scale as $U \sim 1/R$ instead of the linear, elastic solution scaling of $U \sim 1/R^2$ (Eq. (5.1)). The $U \sim 1/R$ scaling predicted here matches the scaling of displacements around a rounded cell in a fibrin matrix (Figs. 5.4 and 5.5, Table 5.1).

A thorough study in three dimensions is not feasible due to the high computational cost of a 3D model. For example, a model with similar nodal spacing as used for the 2D studies would require $201 \times 201 \times 201$ nodes, corresponding to approximately 50 million elements. While such a large simulation is unfeasible here, a preliminary 3D model is created here to demonstrate the scaling of displacements in a 3D matrix. In the 3D model, $49 \times 49 \times 49$ nodes are used to

simulate contraction of a sphere of radius a in a $20a \times 20a \times 20a$ region. Elements connect a cubic shape of nodes with additional elements connecting diagonal nodes of the cube as shown in Fig. 5.11a. Since the model has $49 \times 49 \times 49$ nodes, there are $48 \times 48 \times 48$ cubes in the model. Elements within a sphere of radius a in the center of the model are removed, and an inward displacement of $0.1a$ is applied to each node on the boundary of the sphere. Preliminary FE studies showed that in the 3D model displacements propagate over distances greater than $10a$. Since the model has a size of $20a \times 20a \times 20a$, the scaling of displacements is influenced by the boundaries. To eliminate the influence of the boundaries, either more nodes would have to be added to the model (with an additional computational cost) or the nodal spacing would have to increase. Here, the nodal spacing is already four times the nodal spacing in the 2D model, so it is determined that further increasing the nodal spacing would fail to simulate the fibrous network encountered by a cell. Instead of adding more nodes or increasing the nodal spacing, a symmetric boundary is applied to the bottom of the region ($z = -10a$) only. Since the remaining sides of the region are free to move, the scaling of displacements is only minimally affected by the small size of the model.

Similar to the 2D model, the truss elements each have the strain stiffening constitutive relationship shown in Fig. 5.7b. Also like the 2D model the importance of resistance to compression is assessed by creating models with elements that do and do not support compression. When elements do not support compression, the displacements around the sphere scale as $U \sim 1/R$ (Fig. 5.11b), which disagrees with the Eshelby solution for a linear, elastic continuum. In Fig. 5.11b, the displacements do not approach zero with increasing distance from the center, because the direction along which displacements are plotted is away from the symmetric boundary at the bottom of the model ($z = -10a$). Since the displacements are plotted in the direction of the free edge, displacements approach a constant value of $\sim 0.05a$ instead of zero. When the elements do support compression, the $U \sim 1/R^2$ scaling of the Eshelby solution holds (Fig. 5.11c). Thus, the scaling of displacements in the 3D model follows the trend observed in two dimensions—when the elements do not support compression, displacements

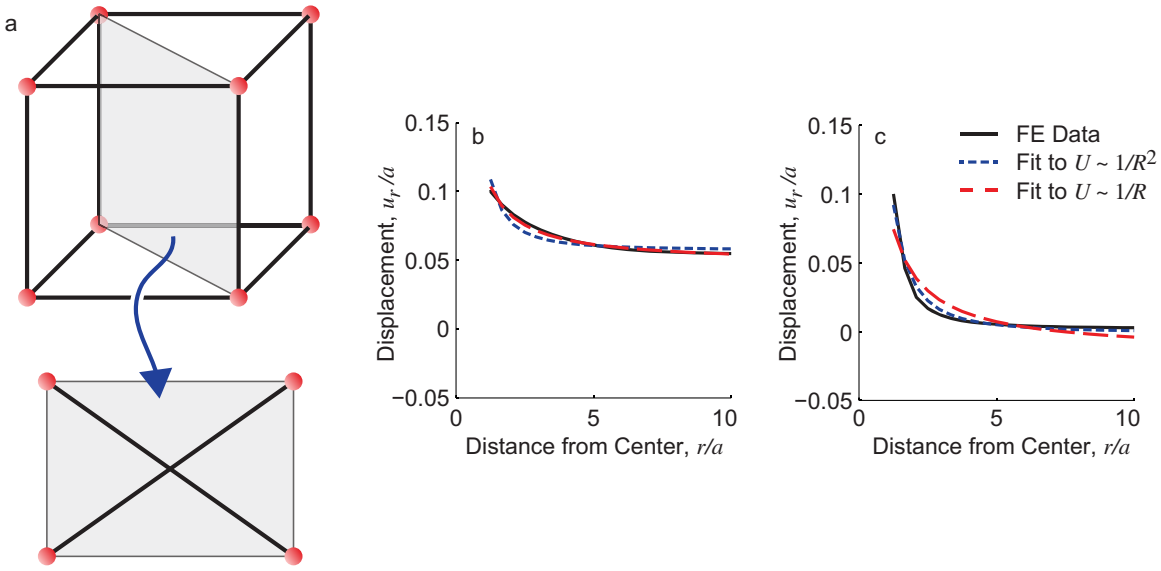

Figure 5.11: The displacements induced by a contracting sphere in a fibrous matrix are analyzed by creating a 3D FE model. $49 \times 49 \times 49$ nodes are used to simulate contraction of a sphere of radius a in a $20a \times 20a \times 20a$ region. A symmetric boundary is placed at the bottom of the cubic region ($z = -10a$), and an inward displacement of $0.1a$ is applied to the nodes located on the edge of the sphere of radius a. (a) Each cube of 8 nodes is connected by truss elements along the edges of the cube. In addition, elements connect the 4 diagonals of the cube as shown in the sketch for 2 of the 4 diagonals. (b) Displacements are computed for elements that do not support compression. The resulting dimensionless radial displacements $U = u_r/a$ along an upward path (away from the symmetric boundary) are plotted and fit to $U \sim 1/R^2$ and $U \sim 1/R$ where $R = r/a$ is the dimensionless distance between the center of the sphere and the position of interest. (c) Displacements are computed for elements that do support compression and are plotted with fits to $U \sim 1/R^2$ and $U \sim 1/R$.

propagate over a longer range with displacements scaling as the integral of the linear, elastic solution. The $U \sim 1/R$ scaling also agrees with the experimental observations for the scaling of displacements induced by a rounded cell (Figs. 5.4 and 5.5, Table 5.1).

Displacements induced by a point force in 3D are next simulated using the 3D structural model. Elements are connected as described previously and as shown in Fig. 5.11a. $49 \times 49 \times 49$ nodes are used to form a $40d \times 40d \times 40d$ cubic region, where d is the nodal spacing. An upward point displacement of magnitude $0.1d$ is applied at the center of the region, and—similar to the 3D model of the contracting sphere—a symmetric boundary is placed at the top of the region. Displacements are first computed using elements that do not support compression (Fig. 5.12a). Similar to the 2D model, the displacement scaling in tension matches the linear, elastic solution, $U \sim 1/R$. Similar to the 3D model of the contracting sphere, displacements do not decay to zero, because the boundary at $z = -20d$ is free to translate. Also similar to the 2D model, the scaling in compression does not match the linear, elastic solution, with displacements scaling according to $U \sim \log(R)$ instead of $U \sim 1/R$. When the elements in the 3D model do support compression (Fig. 5.12b), displacements match the linear, elastic solution whether due to tension or compression.

A comparison between the structural models and the linear, elastic models is shown in Table 5.2. The key result of the structural model is that it explains why displacements induced by a rounded cell scale as $U \sim 1/R$: the matrix fibers do not support compression, and therefore the linear, elastic scaling, $U \sim 1/R^2$ does not hold. In contrast, the linear, elastic solution for a point force applied to the matrix $U \sim 1/R$ does match the displacements induced by a cellular extension, because the displacements induced by a cellular extension are associated with tensile strains, which are not affected by the lack of compression resistance. This result is captured in the simpler 2D model as well but with different scalings. Like for the 3D model, when elements in the FE model do not support compression, displacements propagate over longer distances than predicted by the linear, elastic solution. Also in agreement with the 3D model, the 2D model shows displacement scaling associated with tensile strains agree with the

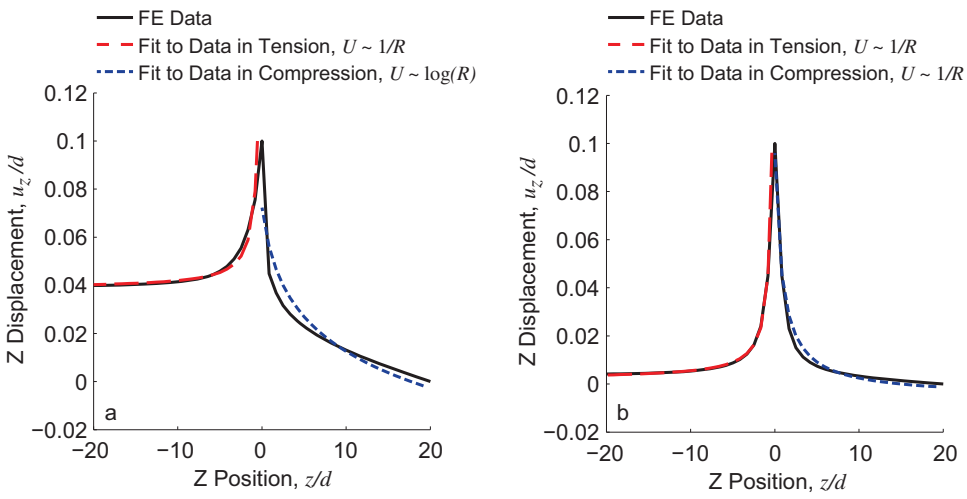

Figure 5.12: The 3D FE model is used to compute displacements induced by a point displacement. $49 \times 49 \times 49$ nodes with a nodal spacing d are used to simulate a $40d \times 40d \times 40d$ cubic region. A symmetric boundary is placed at the top of the region, and a $0.1d$ upward point displacement is applied at the center of the cubic region. (a) Displacements are first computed for elements that do not support compression and are plotted along the line $x = y = 0$. The displacement data associated with tension is found to fit to $U \sim 1/R$, and the data associated with compression fits to $U \sim \log(R)$, where $U = u_z/d$ is the dimensionless displacement and $R = |z/d|$ is the dimensionless distance from the applied point displacement. (b) Displacements are also computed for elements that do support compression. Displacements along $x = y = 0$ in both tension and compression fit to $U \sim 1/R$.

linear, elastic solution. Both the 2D and 3D structural models capture the trends observed experimentally. Furthermore, the contours of displacements and strains for both the contracting circle/sphere and point displacement appear similar for the 2D and 3D models. Thus, either model would be appropriate for further analysis.

5.4 Comparison to Previous Experimental Work

The large number of previous studies on bulk properties of fibrous networks serves as a point of calibration for the structural FE model described in this chapter. One pair of previous studies measured the uniaxial stress–stretch relationship for fibrin clots and revealed a "negative compressibility"—an effective bulk modulus less than zero [133, 134]. While homogeneous materials cannot have a bulk modulus less than zero, negative compressibility of a structure is feasible. For example, it has previously been shown that foams under hydrostatic

Table 5.2: A summary of scaling of displacements U with distance R for a contracting circle/sphere and a point displacement. Summaries for both 2D and 3D models are given here.

2D Model	Contracting Circle	Point Displacement Tension	Point Displacement Compression
Linear, Elastic Solution	$1/R$	$\log(R)$	$\log(R)$
Structural Model with Compression Resistance	$1/R$	$\log(R)$	$\log(R)$
Structural Model without Compression Resistance	$\log(R)$	$\log(R)$	sub–$\log(R)$

3D Model	Contracting Sphere	Point Displacement Tension	Point Displacement Compression
Linear, Elastic Solution	$1/R^2$	$1/R$	$1/R$
Structural Model with Compression Resistance	$1/R^2$	$1/R$	$1/R$
Structural Model without Compression Resistance	$1/R$	$1/R$	$\log(R)$

pressure can undergo negative compressibility due to buckling of individual cells within the foam [135, 136], and other structures have been designed that exhibit negative compressibility [137]. In infinitesimal strain theory, bulk modulus K is related to Poisson's ratio ν through the equation $K = E/[3(1-\nu)]$, where E is Young's modulus [100]. Assuming a positive Young's modulus, a negative effective bulk modulus indicates an effective Poisson's ratio greater than 0.5. While the Poisson's ratio is not directly applicable to large deformations, values of effective Poisson's ratio significantly larger than 0.5 indicate negative compressibility. Inspection of the uniaxial tension data in Ref. [133] indicates the effective Poisson's ratio measured for a fibrin clot is ~ 1.4. The negative compressibility is modeled in Refs. [133, 134] using a special strain energy function that combines a simplified 8 chain Arruda–Boyce model [120] with an empirical term that constrains the material volume through the Jacobian, $J = \det(\boldsymbol{F})$ with $\boldsymbol{F}$ the deformation gradient tensor, to match the negative compressibility observed in the uniaxial tension experiments. The negative compressibility observation appears to depend only on the

additional empirical volume constraining term in the strain energy function, because negative compressibility was also shown for both a 3 chain model and a fibrous network model [133].

To compare the model described in this chapter to the fibrin experiments showing negative compressibility [133, 134], simulations of uniform axial loading are performed in the structural FE model with the "boxed x" element connectivity. Upward displacements are applied to the nodes lying on the top boundary of a square region consisting of 51×51 nodes, and a symmetric boundary is applied to the nodes at the bottom of the square region. The effective Poisson's ratio is computed according to $\nu = -\varepsilon_{\text{lateral}}/\varepsilon_{\text{axial}}$, where the strains ε are the logarithmic strains, $\varepsilon = \log(\lambda)$, with λ equal to the average stretch ratio of the bulk material. When the elements resist compression, the resulting effective Poisson's ratio is in the range of $\nu = 0 - 0.3$ (Fig. 5.13a, solid red line), in agreement with homogeneous materials, which cannot have a Poisson's ratio greater than 0.5. In contrast, when the elements do not resist buckling, the effective Poisson's ratio for large axial stretches is 1.3 (Fig. 5.13a, dotted blue line), in agreement with the effective Poisson's ratio of ~ 1.4 observed previously for fibrin [133, 134]. Also in agreement with previously reported experimental observations [133] and experimental observations reported in Chapter 4 (Fig. 4.3) is the fact that the effective Poisson's ratio for small stretches ($\lambda < 1.1$) is ~ 0.5, consistent with fibrin being nearly incompressible for small deformations. Further FE simulations using an even lower resistance to compression or adding randomness in the nodal positions increased the computed values of Poisson's ratio. Nevertheless, the effective Poisson's ratio for elements that do not support compression was found to range from 0.5 to 2 for all simulations, which gives sufficient agreement with the previous uniaxial experiments on fibrin [133].

In addition to negative compressibility, fibrin has been shown to exhibit negative normal strains under shear loading [138], in agreement with predictions for a fibrous mesh [124]. The negative normal strains are the opposite of the Poynting effect [139], which is associated with positive axial strain in rods under torsion. To test whether the structural FE model captures the negative normal strains, shear is applied to the top face of an elongated region consisting of

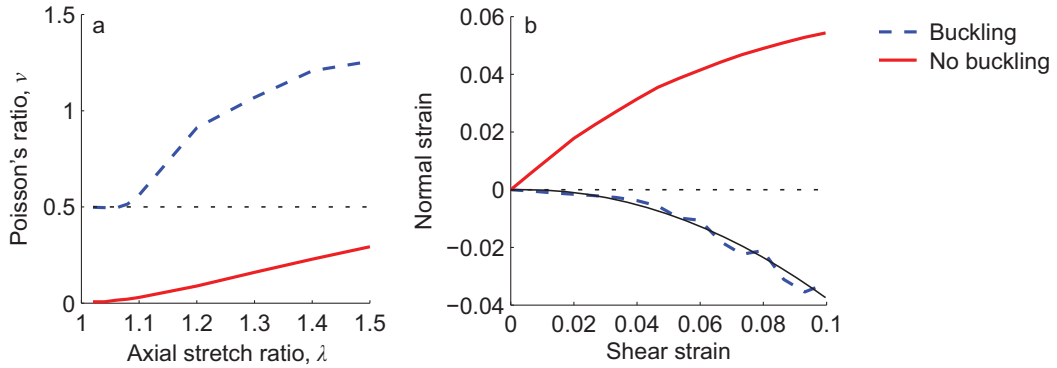

Figure 5.13: Global loading is applied to the fibrous FE model to compare to other work on polymer gels. (a) Uniaxial tension is applied with a displacement boundary condition to a square model consisting of 101×101 nodes. When the elements do not support compression (buckling), the effective Poisson's ratio reaches a maximum value of ~ 1.5. The dotted line is drawn to indicate the upper limit for a linear, elastic continuum, $\nu = 0.5$. (b) Simple shear is applied with a displacement boundary condition to a flattened 501×51 node region. When fibers buckle as a result of the shear loading, negative normal strains are observed. The curve of negative normal strains are fit to a quadratic function (thin black line) with good agreement. For reference, a dotted line is drawn for a normal strain equal to zero.

501×51 nodes using a horizontal displacement boundary condition. Nodes are connected using the "boxed x" connectivity, and a fixed boundary condition is placed on the side opposite to the horizontal displacement boundary condition. When the elements resist compression, a positive normal strain is observed under shear loading (Fig. 5.13b, solid red line), consistent with the Poynting effect. However, elements that simulate buckling by having no resistance to compression create negative normal strains under loading the matrix in shear (Fig. 5.13b, dotted blue line), in agreement with experimental observations for fibrin [138]. Previous work that simulated negative normal strains using a filament network reported a quadratic dependence of negative normal strain on applied shear strain [124]. Thus the negative normal strains are fit to a quadratic function (Fig. 5.13b, thin black line). The good agreement between the simulated negative normal strains and the quadratic fit further confirms that the structural FE model described in this chapter agrees with previous work on polymer networks, particularly fibrin.

5.5 Mechanism for Tether Formation

The observation that displacements propagate further in the structural model with elements that do not support compression gives a hint as to how tethers form in the matrix between neighboring cells (Fig. 5.2). These tethers likely require the cells to induce directed, long range displacements into the matrix. The propagation of cell-induced displacements through the matrix is investigated here by using the structural FE model to simulate a contracting circular region, which simulates a rounded cell beginning to spread. Fig. 5.9 shows that when the elements in the FE model do not support compression, displacements propagate a longer range through the matrix than for elements that do support compression, and the displacements scale as $U \sim \log(R)$. The logarithmic scaling has the property that displacements do not decay to zero as $R \to \infty$. This observation is further investigated by creating a model of a contracting sphere with free boundary conditions. The model is solved using elements that do and do not support compression (Fig. 5.14a and b, respectively). For elements that support compression even with free boundary conditions on the edges of the region, displacements decay to zero at the region edges. In contrast, when elements do not support compression, displacements remain finite at all locations in the simulated region. The largest displacements propagate along the horizontal, vertical, and diagonal directions, which correspond to the directions of the elements in the "boxed x" element connectivity (Fig. 5.6).

While, for the model that does not support compression, displacements propagate along the horizontal, vertical, and diagonal directions, the propagation of displacements in these directions is an artifact of the model. To more accurately capture the long range displacement propagation observed in the fibrous matrix tethers, the displacements between a pair of contracting circles is analyzed. The contracting circles are geometrically similar to a pair of spherical cells beginning to spread. A model is created with a circle of radius a positioned a distance $10a$ above a symmetric boundary. The model uses 501×351 nodes to simulate a $50a \times 35a$ region. Horizontal (x) and vertical (y) displacement components are computed for elements that do and do not support compression (Fig. 5.15). The displacements for elements

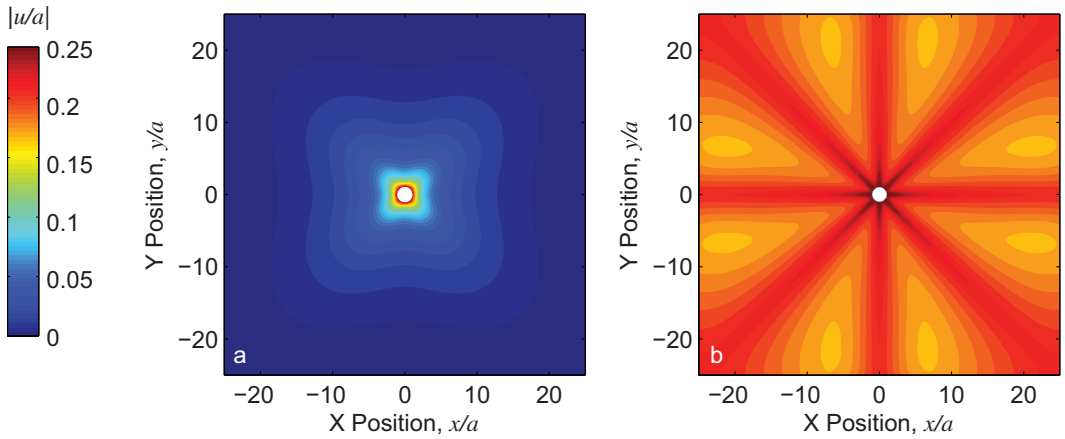

Figure 5.14: The "boxed x" 2D connectivity is used to simulate a contracting circle or radius a in a $50a \times 50a$ square region composed of 501×501 nodes. The circle contracts with radial displacements of $0.25a$. No boundary conditions are applied at the edges of the square region. Contours of the resulting displacements are plotted for (a) elements that support compression and (b) elements that do not support compression.

that do support compression act locally and over a shorter range than for elements that do not support compression, in agreement with the previous conclusion that displacements propagate over a longer range when the elements do not support compression. For elements that do not support compression, the displacements propagate over a long range, with large vertical displacements between the contracting circle and the symmetric boundary (Fig. 5.15d). Most striking is the fact that for elements that do not support compression, displacements horizontal to the symmetric boundary are large and act over nearly one third of the modeled region (Fig. 5.15c). These displacements act inward, toward the line $x = 0$, indicating that a pair of contracting spheres induces large-scale motion in the fibrin matrix. Inward motion of the matrix near a cell has been observed experimentally (Fig. 5.16), with the cell contracting and applying large-scale inward displacements similar to those observed in Fig. 5.15c.

The inward matrix displacements perpendicular to the axis connecting a pair of neighboring cells that are observed experimentally (Fig. 5.16) and in the FE model (Fig. 5.15c) result in highly compacted regions of matrix fibers. In turn, the compacted fibers support tensile stresses along the line connecting the centers of the neighboring cells. These tensile stresses are a mechanism by which a cell could mechanically sense its neighbor. The structural model

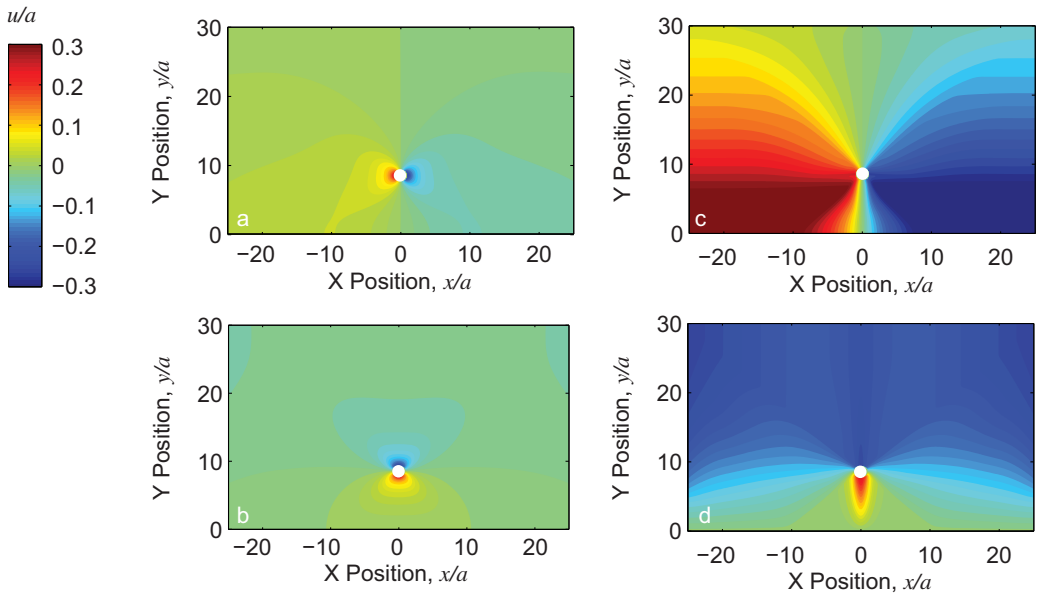

Figure 5.15: The interaction of a pair of contracting circles is simulated with the structural matrix model. The displacements of a pair of circles of radius a in the model are computed by simulating only half the geometry with a symmetric boundary condition at $y = 0$. The contracting circle undergoes a displacement of $0.25a$ along its boundary. Displacement components in the x (a) and y (b) direction are plotted for elements that support compression. The model is also solved using elements that do not support compression with contour plots shown for displacements in the x (c) and y (d) directions.

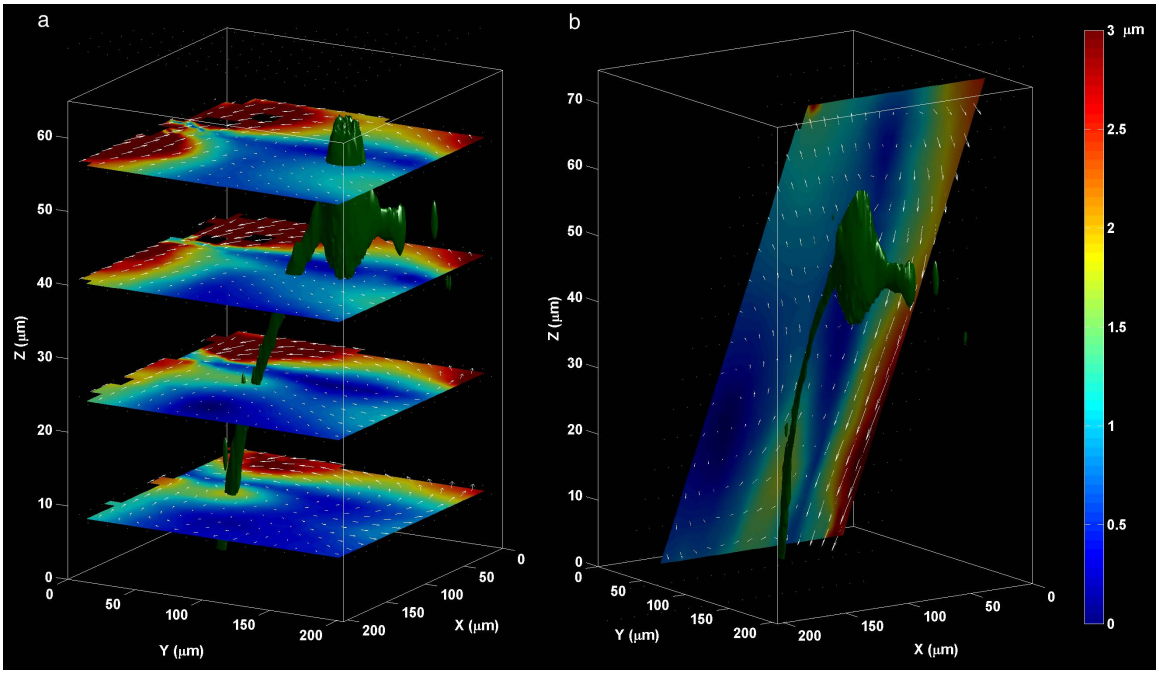

Figure 5.16: 3D TFM as described in Chapter 2 is used to measure cell-induced fibrin matrix displacements. Contours of the displacements are plotted on different planes with white quivers indicating the direction of displacements within the planes shown. Planes are shown in the horizontal (a) and nearly vertical (b) directions. The cell (green) applies displacements of $\sim$ 1.5 μm directly to the matrix at the leading edge of a protrusion. Large-scale inward displacements of 3 μm—similar to the inward displacements in Fig. 5.15c—are present near $x = 0, y = 0$. These displacements are likely the result of tractions applied by the cell shown here and another cell outside of the imaging region.

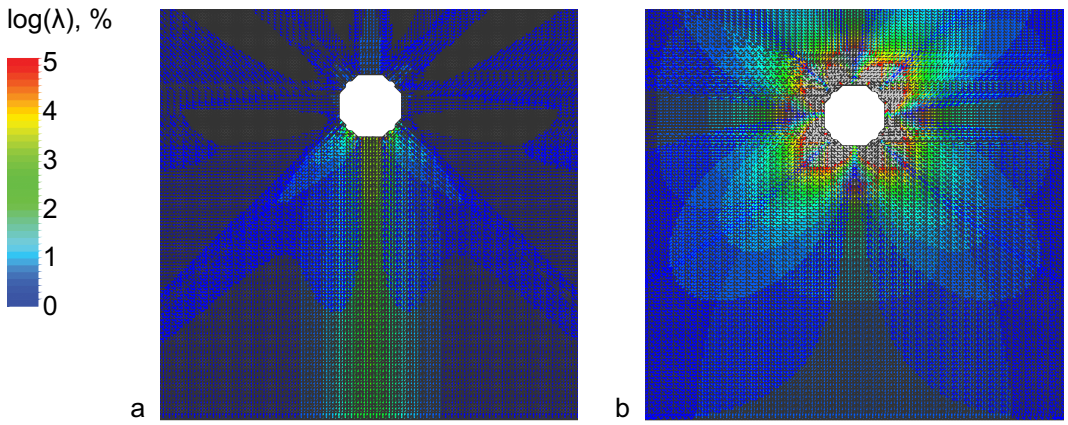

Figure 5.17: Matrix strains between a pair of contracting cells are modeled with the 2D structural FE model using the "boxed x" element connectivity. Displacements of $0.25a$ are applied at the boundary of a circle of radius a in a $500a \times 350a$ region with 501×351 nodes. The center of the circle is placed $D = 10a$ above symmetric boundary. (a) When the elements do not support compression, axial logarithmic strains in each element, $\log(\lambda)$, localize between the contracting circle and the symmetric boundary along directional tethers. The strains have a nearly constant magnitude of $\sim 2.5\%$ as they propagate all the way to the symmetric boundary. Since the elements do not support compression, only tensile strains are shown. (b) When the elements resist compression, logarithmic strains remain localized around the contracting circle. The symmetric boundary at a distance $10a$ from the center of the circle has no effect on the resulting strains.

captures these tensile stresses when the elements do not support compression (Fig. 5.17a) and not when the elements resist compression (Fig. 5.17b). For elements that do not support compression—which have been shown to better capture the mechanics of the fibrin matrix—strains propagate with a slowly decaying magnitude over a long distance of $D = 10a$ (Fig. 5.17a). In this simulation, the inward displacement applied at the boundary of the circle of radius a is $0.25a$. Using the Lamé solution (given in Eq. (5.7)) the displacement inside a contracting circle varies linearly with radial distance from the center, and therefore the strain in the circle is a constant value of $\varepsilon_0 = u/r = 0.25$. The logarithmic strains at the symmetric boundary have a magnitude of $\sim 2.5\%$, which is about $1/10$ of the strain within the contractile circle ε_0. Repeated FE simulations with different levels of contractile strain ε_0 showed the matrix strains scale nearly linearly with the input strain ε_0. For example, if the strain in the circular region is $\varepsilon_0 = 0.1$, the resulting strain on the symmetric boundary a distance $10a$ away is $\sim 1\%$.

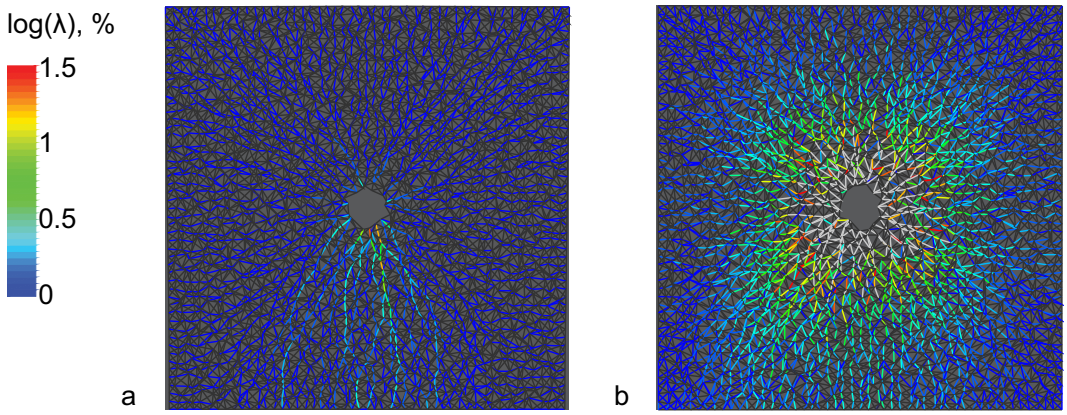

Figure 5.18: Tether formation depends only on fiber buckling. 51×51 nodes are used to simulate a circle of radius a contracting with a contractile strain of $0.2a$ at the center of a $20a \times 20a$ square region with a symmetric boundary at the bottom. This is a reduction of the nodal density as compared with Fig. 5.17. Randomness in node locations is included in the model by adding a different uniform random variable to the position of each node. The plots of positive logarithmic strain $\varepsilon = \log(\lambda)$ show that strains propagate along directional paths to the symmetric boundary at the bottom only when the elements do not support compression (a) and not when the elements do support compression (b), in agreement with Fig. 5.17.

The mechanism for tether formation between a simulated contracting cell and the boundary is independent of the matrix fiber density, randomness in the positioning of matrix nodes, and the distance between the sphere and the boundary. For example, when fewer nodes, 51×51, are used to simulate contraction of a circle of radius a in a $20a \times 20a$ region, the strains propagate along tethers only when the elements do not support compression (Fig. 5.18a). When the elements resist compression (Fig. 5.18b) strains localize around the contracting circle and form a nearly symmetric strain distribution around the circle. Consistent with the previous observation that tether formation requires large inward displacements between the contracting circular region and the symmetric boundary (Fig. 5.15), contour plots of compressive strains in matrix tethers (Fig. 5.19b) show large horizontal, compressive strains with a magnitude $> 10\times$ the magnitude of the tensile strains (Fig. 5.19a) in the tether region. This result is consistent with the direct images of matrix tethers (Fig. 5.2), which show increased matrix intensity in the tether region, indicating matrix densification.

When the distance between the circular region and the symmetric boundary D is changed, matrix strains still propagate to the boundary, with a change in only the magnitude. The

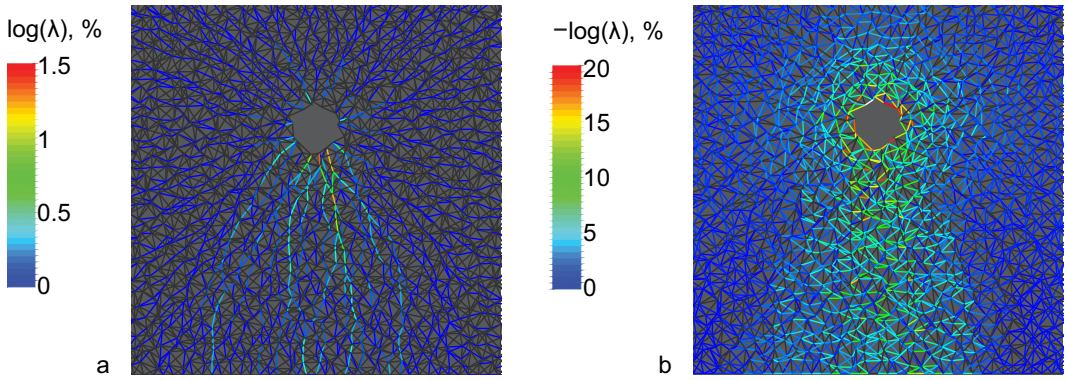

Figure 5.19: Tensile and compressive strains are plotted for the same model as shown in Fig. 5.18a. (a) Tensile strain components are nearly vertical and along a series of lines connecting the contracting circular region to the symmetric boundary. (b) Compressive strains are an order of magnitude larger than tensile strains, and they are in directions perpendicular to the tensile strains. The plots are zoomed in on the region between the contracting circular region and the symmetric boundary for clarity.

effect the distance to the boundary has on the strains in the material at the boundary is evaluated using the structural FE model. The same model as is used for Fig. 5.17 is run multiple times with different distances D between the center of the contracting circle and the symmetric boundary. To compute the simulated matrix strains at the midpoint between a pair of contracting cells, the logarithmic strain at the symmetric boundary is plotted in Fig. 5.20 for varying distances between the contracting circle and the boundary. The strains ε decrease with increasing distance from the boundary D according to $\varepsilon \sim 1/D$. The $1/D$ scaling is consistent with the logarithmic scaling of displacements observed in the 2D FE model, because strains should scale as the derivative of displacements. Taken together these results demonstrate that fiber buckling—and not fiber density or node location randomness—controls the formation of stress carrying tethers in the matrix.

The results shown in Figs. 5.15, 5.17 and 5.20 use the "boxed x" element connectivity with no randomness in the nodal locations. While including nodal location randomness is possible in this model, randomness creates difficulties in model convergence, and therefore it was not included in this analysis. As shown in Fig. 5.8, node location randomness appears to decrease the distance over which strains propagate. Nevertheless, it was previously found that randomness does not change the logarithmic scaling of displacements. Thus, the scaling of strains

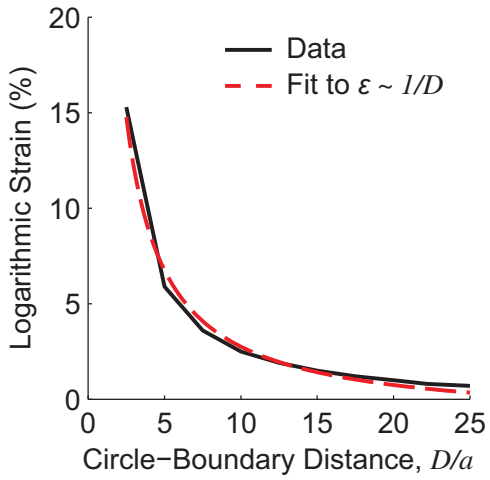

Figure 5.20: The propagation of strains between a pair of neighboring cells is investigated by using a symmetric boundary. The same model as that used in Fig. 5.17 is used with different distances D between the circle of radius a and the symmetric boundary. The circle undergoes contraction with a contractile strain of 0.25. Logarithmic strains ε on the symmetric boundary are plotted and fit to $\varepsilon \sim 1/D$. Note that the dimensionless distance from the center of the sphere to the symmetric boundary D/a is equal to the ratio of the distance between a pair of neighboring cells to the cell diameters.

between a pair of interacting cells is expected not to depend on node location randomness.

5.6 Effect of Matrix Fiber Density

In 3D TFM experiments with a fibrous matrix, the matrix fiber density can be easily changed by adjusting the concentration of fibrinogen when polymerizing the matrix (e.g., see the images in Chapter 2, Fig. 2.9). An increase (decrease) in matrix fiber density effectively increases (decreases) the stiffness the cell senses, which can lead to a change in the cell behavior [3]. However, a change in fiber density also changes the number of locations a cell can adhere and interact with its surroundings, resulting in a change in the cell's chemical and physical environment. Thus, the experimentally simple approach of modulating the fiber density is a poorly controlled study that requires careful analysis. Fortunately, the structural FE model can be employed to simulate the change in the mechanical and physical environment caused by increasing or decreasing the fibrin matrix density.

To simulate cell-induced matrix displacements, the familiar contracting circle of radius a

is again employed in a $20a \times 20a$ square region with elements connected with the "boxed x" connectivity. Inward displacements of $0.2a$ are applied to the nodes on the edges of the circle, corresponding to a contractile strain of 0.2 in the circular region. A symmetric boundary is used at the bottom of the region to simulate the interaction of a pair of cells, and the elements do not support compression. The model is first solved with no randomness in the nodal positions, and then randomness is included by adding random variables taken from a uniform distribution ranging from $-0.5d$ to $0.5d$ to the horizontal (x) and vertical (y) positions of each node.

For simulations with and without randomness and with nodal densities ranging from 51×51 to 251×251, the computed displacements appear nearly identical to the displacements given in Fig. 5.15c,d. Horizontal (x) displacements between the contracting circle and the symmetric boundary are zero along the line $x = 0$ (drawn from the center of the circle to the boundary), but large inward displacements are observed on either side of the line $x = 0$. These displacements have a magnitude similar to the displacements applied by the contracting circle to the matrix, and occur over a long range—several times the radius of the cell. Vertical (y) displacements are observed above and below the cell, with a decrease in magnitude along a path from the center of the cell to the symmetric boundary. Strains between the contracting circle and the symmetric boundary can be computed either by differentiating the displacements or by plotting strains within each element. Either strain computation approach results in strains that scale as $\varepsilon \sim 1/R$, consistent with the previous finding that the displacements scale as $U \sim \log(R)$ (Table 5.2).

Further consideration of the strains shows the highly heterogeneous nature of the FE model. Tensile strains in each element using either 251×251 nodes or 51×51 nodes are plotted in Figs. 5.21a and 5.21b, respectively. The magnitudes and locations of tensile strains for both 251×251 and 51×51 nodes appear similar. Strains are largest in the center of the region and between the contracting sphere and the symmetric boundary. Strains with magnitudes of 2%–3% are present in vertically aligned elements between the contracting sphere and the symmetric boundary, and they scale as $\varepsilon \sim 1/R$. The observation that strains are carried

through the fibrous structure along linear, aligned elements is a direct result of the fact that the elements in the model are linearly aligned before implementing contraction of the circular region. The fibrin matrices studied here have a more random structure, and thus randomness is included in the nodal positions.

When randomness is added to the model, tensile strains propagate differently through the matrix for either 251×251 or 51×51 nodes (Fig. 5.21c,d). Strain magnitudes are smaller (1%–1.5% instead of 2–3%), and the strains are slightly less localized around the vertical line $x = 0$. More noticeable—especially for 51×51 elements (Fig. 5.21d)—is the fact that strains appear to propagate along specific paths from the edge of the contracting circle to the symmetric boundary. These paths carry most of the tensile load between the sphere and the boundary, and they resemble the tethers observed in the experiments (Fig. 5.2). As the number of nodes increases from 51×51 to 251×251, the number of nodes across the diameter of the contracting circle increases from 5 to 25. Thus, the simulation with 251×251 nodes nearly becomes a continuum, and the stress-bearing tethers are no longer observed. As previously described, when no randomness is included in the simulation, strains scale as $\varepsilon \sim 1/R$. The strain scaling with node position randomness is analyzed by following individual tethers, like those observed in Fig. 5.21d. Strains are plotted against distance along individual fibers for a model using 51×51 nodes (Fig. 5.22). While the strains fluctuate along a tether, the mean strains scale as $\varepsilon \sim 1/R$, in agreement with the scaling of strains when no randomness is applied.

5.7 Discussion and Conclusions

This chapter describes the development of a structural constitutive model for cell-induced deformations in a 3D fibrous matrix. The model applies the FE method using truss elements that support only axial forces. The random distribution of nodal positions and element lengths in the structural model matches the fibrous microstructure of the matrix. The model can simulate local matrix inhomogeneities, matrix fiber alignment, different matrix densities, and

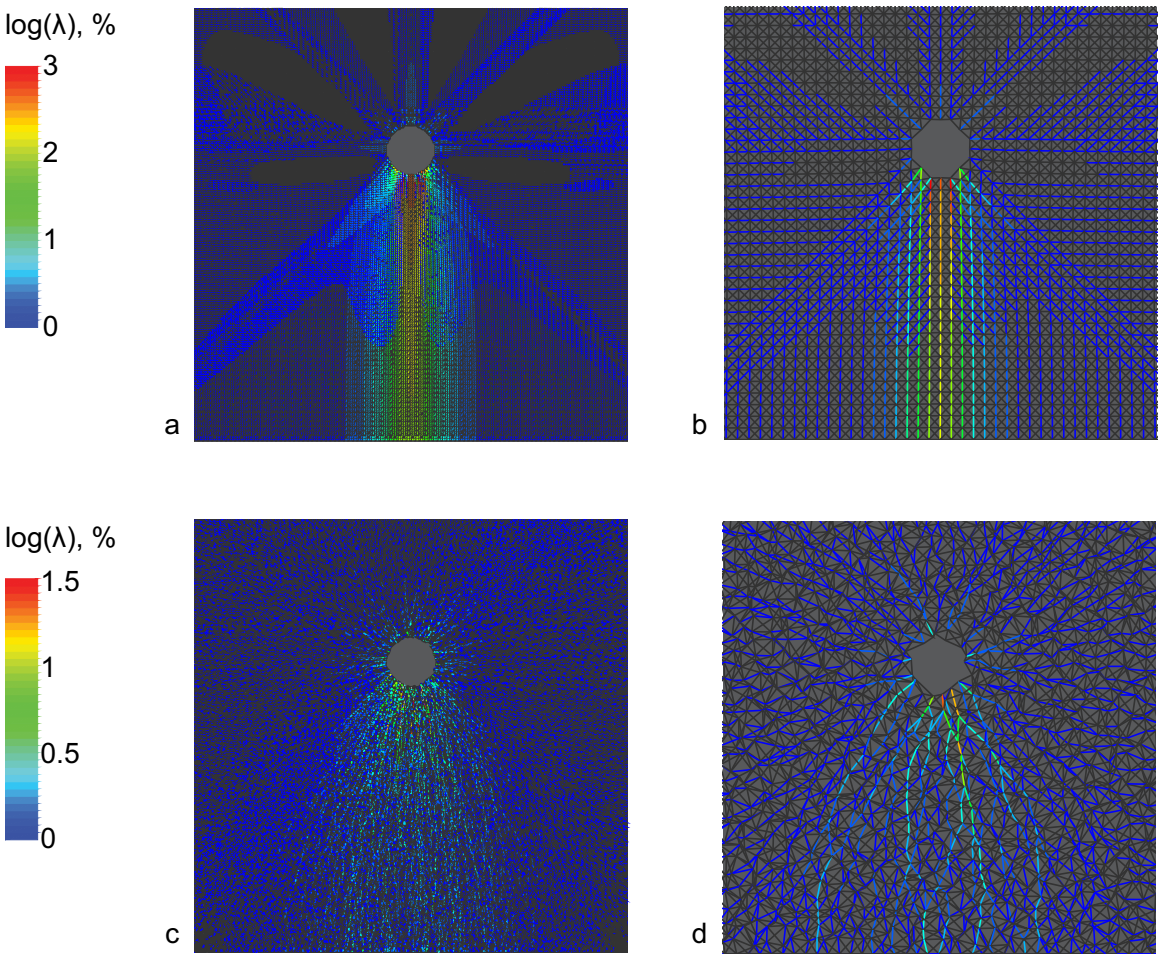

Figure 5.21: The effect of matrix fiber density on the propagation of cell-induced displacements is assessed by modeling a contracting circle of radius a in the center of a $20a \times 20a$ square region. Inward displacements of $0.2a$ are applied to the nodes on the edge of the circle. A symmetric boundary is applied at the bottom of the region. The model is solved first using no randomness in the nodal locations using (a) 251×251 nodes and (b) 51×51 nodes. Randomness was then included in the nodal locations (see text for more information), and the model was again solved with (c) 251×251 nodes and (d) 51×51 nodes. Logarithmic strains, $\varepsilon = \log(\lambda)$, where λ is the stretch ratio, are plotted for each element in a zoomed-in region that includes the contracting sphere (offset from center in plots) and the symmetric boundary (bottom). For (a) and (b), the color scale represents 0–3% strain; for (c) and (d), 0–1.5%.

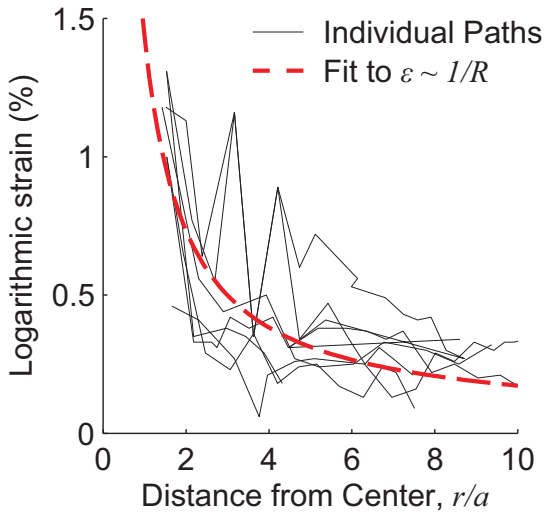

Figure 5.22: Logarithmic strains, $\varepsilon = \log(\lambda)$, are computed along various individual tethers shown in Fig. 5.21d and plotted against distance $R = r/a$ from the center of the contracting circular region. The mean strain–distance curve fits to $\varepsilon \sim 1/R$ with good agreement.

non-affine deformations at the scale of the single fiber. Most importantly, the structural FE model can simulate buckling of individual fibrin fibers by using a stress–strain relationship that has negligible resistance to compression. Fiber buckling appears to be a key mechanical process in fibrin matrices, as it describes the experimentally observed scaling of cell-induced matrix displacements.

Also resulting from fiber buckling are the tethers of localized matrix deformation. These tethers carry stresses along directional paths between neighboring cells (Fig. 5.2). Matrix fibers perpendicular to the tethers undergo compression as a result of the Poisson effect. When the elements in the 2D FE model simulate buckling, the matrix strains remain localized to the tethers and propagate over a long distance ($\varepsilon \sim 1/R$, Fig. 5.22). In contrast, when the elements do not buckle, tethers do not form (Figs. 5.17 and 5.18), because the Poisson-induced compression distributes the strain energy over a wider and therefore shorter distance ($\varepsilon \sim 1/R^2$). Thus, tether formation requires fiber buckling to propagate strains over a narrow, directed path.

The fluctuations observed in strain along the individual tether paths in Fig. 5.22 are localized to individual elements within the FE model. A measurement of strain using digital volume correlation (DVC) (as described in Chapter 2) would not reveal these highly localized

strains due to the fact DVC correlates subsets of finite size and therefore lacks the spatial resolution to measure strains in a single fiber. Instead, displacements measured by DVC would match those shown in Fig. 5.15c,d. Computation of strain from these displacements would result in a smooth, slowly varying strain field. Fluorescent labeling of fibers (e.g., Fig. 5.2) provides an alternative experimental approach to directly visualize strain localization. While fiber labeling is a qualitative approach, combining the fiber visualization with a quantitative FE model as described in this chapter yields new insights in the displacements applied by a cell to the matrix.

Buckling of a fiber network has been analyzed previously, with a model for individual fibers that included both axial and bending stresses [124]. While this study mentioned fiber buckling's role in material nonlinearities such as softening in compression and negative normal strains in shear, the model was only designed to simulate axial and shear loadings. The use of a FE framework as described in this chapter offers the advantage that any kinematically admissible loading can be applied directly to the nodes in the FE model. The use of truss elements that do not resist bending or compression offers a simple means to simulate the nonlinear behavior of the fiber network. The FE model circumvents the mathematical singularities associated with buckling by using a stress–stretch relationship for the truss elements that has negligible resistance to compression. Previous work by Janmey et al. has shown that nonlinear material behaviors such as negative normal stresses in shear similarly do not require modeling fiber buckling through a mathematical instability [138]. Janmey et al. simply use a strain stiffening stress–stretch curve that has a much greater slope in tension as compared to compression. While the model of Janmey et al. includes a WLC-like microstructural argument for choosing the stress–stretch relationship, the end result is a stress–stretch curve that is similar to the curve used in the structural FE model described here (Fig. 5.7b,c). Therefore, the FE model's simulation of fiber buckling by using a consitutive model with negligible resistance to compression is consistent with previous work. Since direct input of a stress–stretch relationship into FE software is straightforward, this work can easily be adapted to further

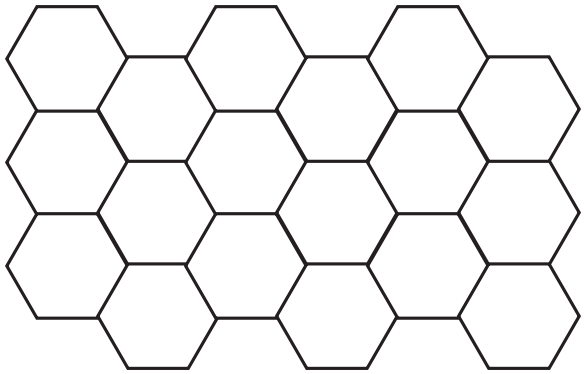

Figure 5.23: A sketch of the hexagonal network structure used in Ref. [125]. Elements support only axial force and are connected by pin joints.

studies.

Several other studies have investigated the mechanical properties of a random distribution of fibers. For example, several previous reports have simulated global normal and shear loading on a random fibrous array [121, 122, 123, 124]. However, such studies have primarily focused on predicting the macroscale properties of the bulk material. One previous study did apply a 2D structural network model to describe the displacements around a contracting circular region in a simulation of lung tissue [125], but this study did not account for buckling of individual structural elements. In this study, the authors observed that displacements propagated over a longer range in a structural model that used a hexagonal network of elements (Fig. 5.23), as compared with a structural model with elements in a triangular network or a continuum. While the authors of this study fit the data to $U \sim 1/R$ instead of $U \sim \log(R)$, a qualitative inspection of their data reveals that $U \sim \log(R)$ would provide a better fit. Thus the displacements induced by a contracting circle in a hexagonal network scale in the same way as the displacements in the structural FE model described in this chapter. This result comes from the fact that similar to the structural model that accounts for fiber buckling, a hexagonal network with pinned connections between elements does not resist compression due to a structural instability similar to buckling.

The structural FE model is consistent with previous continuum models for fibrin [133, 134]. The previous models for fibrin, which use continuum mechanics and provide solutions that can

be computed analytically, would likely result in the same scaling of cell-induced displacements in a fibrin matrix. However, the continuum mechanics model uses a homonegenization of representative volume elements and therefore cannot account for inhomgeneity, anisotropy, a changing matrix density, or non-affine deforations. The structural FE model presented in this chapter does not have the limitations of a continuum approach, and it additionally offers the advantage that deformations and stresses within the structural elements can be compared directly to the microstructural images of the fibrin matrix. Thus the structural FE model adds additional analysis capabilities to the previous continuum models.

The ability of the FE model to capture the displacements and strains in a fibrous matrix has implications on the mechanical interactions between neighboring cells. A previous 2D study using a fibrin gel showed that cells plated on a fibrin substrate exert displacements that influence the behavior of neighboring cells hundreds of microns away [140]. While Ref. [140] attributed the long range cell–cell mechanical interactions to strain stiffening of the fibrin matrix, it is more likely that the long range displacement propagation was a direct result of the negative compressibility observed previously for fibrin [133, 134] and described in this chapter with a FE model that simulates fiber buckling. The displacements observed in the FE model can predict a critical distance for cell–cell mechanosensing. In three dimensions, a contracting cell induces displacements that scale as $U \sim 1/R$. Cells have been shown to sense chemical gradients with high sensitivity: chemical gradients of $< 1\%$ of a total chemical concentration can direct cell migration [141, 142]. Assuming cells can sense mechanical gradients with similar sensitivity makes it possible to predict a critical distance for cell–cell mechanical interaction. While it is known that cells sense gradients, it is unknown if cells sense displacement gradients or stress (strain) gradients. Both possibilities are examined here. A spherical cell of radius a contracting by some fixed amount ε_0 will induce a strain field in a 3D matrix given by $\varepsilon = \varepsilon_0/R^2$ where $R = r/a$ is the normalized distance from the center of the cell. Since a neighboring cell is predicted to sense a strain of $\varepsilon = 0.01\varepsilon_0$, this scaling predicts that a cell can sense a neighboring cell a distance $10a$ away if cells sense a displacement gradient. If cells

instead sense a stress (or strain) gradient, the scaling becomes $\varepsilon = \varepsilon_0/R^3$, and the scaling predicts cells sense one another when they are within a distance of $4.6a$ from one another. Future experiments could apply the scaling relationships discovered in the chapter to further analyze cell mechanosensing in a 3D matrix.

The model developed here could motivate future work related to cell–matrix interactions. Specifically, similar models could predict the local, inhomogeneous, anisotropic "stiffness" that a cell senses in a 3D fibrous matrix. The FE-based constitutive model developed here could serve as a starting point for researchers that require accurate characterization of a 3D fibrous matrix. Furthermore, this chapter has described analysis of cell–cell mechanical interactions through a 3D fibrin matrix. Analysis using the framework for cell mechanosensing outlined in this chapter will lead to further insights in the feedback loop between matrix mechanical properties, cell contractile activity, and mechanotransduction.

Chapter 6

Conclusions and Outlook

This thesis has described a combination experimental and theoretical approaches to quantify physical interactions between cells and a biologically relevant three-dimensional (3D) fibrous matrix. The 3D traction force microscopy (TFM) approach developed here for a fibrous matrix and described in Chapter 2 represents a new experimental technique that goes beyond the commonly used traction measurement approaches on synthetic, flat substrates. Digital volume correlation (DVC) was combined with confocal microscopy to measure displacements of the fibrin matrix with a precision of ~ 0.1 μm. The strain tensor was computed by numerically differentiating the displacement data, and the stress tensor was computed by applying the incompressible form of Hooke's Law. Finally, tractions were computed directly from the stress tensor by applying the Cauchy relation. This direct approach of traction computation is simpler than a previously reported inverse approach [66], and the computation of tractions in a fibrous matrix represents a new technical achievement. Additionally, the use of DVC has allowed for particle free TFM, which uses fluorescent labeling of the fibrin matrix as a random high contrast pattern for correlation instead of synthetic fluorescent particles. The direct matrix labeling provides both a speckle pattern for DVC and direct microstructural imaging for further analysis.

The 3D TFM technique developed here is applied to study cell division and spreading in a 3D fibrous matrix. Dividing cells anchor themselves to the matrix and exert tensile forces through long protrusions that are not present in two dimensions. The protrusions direct the

axis of cell division and the subsequent positioning of the daughter cells. Cells spreading in a 3D matrix begin to invade where they can apply minimal tractions to the matrix. As invasion continues, the cell both pushes and pulls on the matrix, resulting in rearrangement of matrix fibers and a subsequent change in local matrix mechanical properties. After rearranging matrix fibers, the cell continues to invade in regions that require minimal tractions.

A structural finite element (FE) model consisting of truss elements supporting axial force describes the scaling of displacements induced by a contracting cell. While a linear, elastic model predicts displacements U induced by a contracting cell scale with distance R as $U \sim 1/R^2$, the TFM experiments show the scaling to match $U \sim 1/R$. The FE model resolves this discrepancy by considering buckling of individual matrix fibers. When the fibers do not support compression as a result of buckling, cell-induced displacements propagate a longer range through the matrix with scaling that agrees with the TFM data of $U \sim 1/R$. In addition to agreeing with the scaling of cell-induced displacements, the fiber buckling in the structural FE model is consistent with previous experiments and continuum models for a fibrin clot that observe a negative compressibility [133, 134].

In addition to matching the experimental observations of negative compressibility and long range displacement propagation, the FE model simulates the experimentally observed "tethers" that connect pairs of neighboring cells in the fibrous matrix. The tethers, which support forces between neighboring cells, result from matrix deformations that are localized to the linear tether paths. The tethers require fiber buckling to form. Without fiber buckling, Poisson-induced compressive stresses propagate normal to the tether directions and distribute the strain energy over a wider area. Fiber buckling directs tensile deformations along linear paths within the fibrous matrix, resulting in the stress-supporting fibrin tethers observed experimentally between pairs of cells. The stresses supported by these tethers offer a mechanism for long range mechanical cell–cell interactions, and therefore the negative compressibility of the fibrin matrix enables long range cell–cell mechanosensing. Since the stresses within an individual tether are not resolvable with the 3D TFM approach described here, future work will

have to apply alternate experimental techniques to measure the stresses within these matrix tethers.

6.1 Future Work in 3D Traction Force Microscopy

This thesis describes the development of an approach for measuring 3D cell tractions in a 3D fibrous matrix. Additional refinement of the experimental technique is required to expand 3D TFM for general use in the biology community. Possibly the largest source of error in the traction computations reported here comes from the assumption that the fibrin matrix is homogeneous, isotropic, linear, and elastic. More refined mechanical models for a fibrous network would help to better determine the constitutive properties of the matrix. While various theories exist on the mechanics of polymer networks and open cell foams, these theories have yet to be applied to predict the extracellular matrix stiffness at the localized length scale of the cell. Thus, there remains a need for models that predict the local matrix properties sensed by a cell in three dimensions. Chapter 5 of this thesis describes a FE based approach to simulate a nonlinear, inhomogeneous fiber network.

Further refinement of matrix constitutive models will not only reduce error in traction computation in a 3D matrix but will lead to new understandings of cell behavior. The structural FE model together with previous continuum models for a fibrin matrix [133, 134] reveal a rich set of constitutive behaviors including a large effective Poisson's ratio (> 0.5) and propagation of cell-induced displacements along highly localized linear paths within the fibrin matrix. These observations motivate future studies on constitutive properties of biologically relevant 3D matrices. For example, further matrix analysis through similar mechanical models will prove useful for quantifying the effects of inhomogeneity and anisotropy on the effective matrix stiffness sensed by a cell. The fiber alignment observed at the leading edge of a spreading cell likely increases the effective matrix stiffness sensed by the cell, and therefore alignment of fibers could play a significant role in mechanotransduction. Additionally, the FE model could

be further extended to account for matrix viscoelasticity and plasticity to better understand how cells rearrange their local surroundings. To what extent nonlinear processes like fiber alignment, negative compressibility, viscoelasticity, and plasticity control cell behavior in a 3D matrix remains unknown. Further analysis of predictive constitutive models like the one described in Chapter 5 will answer these fundamental questions and yield valuable insights into how a cell senses and responds to its external environment.

In addition to models for a fibrous matrix, experimental approaches that can quantify the elastic (and viscoelastic) properties of the extracellular matrix would improve the accuracy of the traction computation. Besides cell-induced fiber reorganization, many cell types are known to excrete extracellular matrix proteins, thereby changing the local mechanical environment. Particle microrheology can quantify constitutive properties by relating Brownian motion of sub-micron-sized particles in a fibrous gel to elastic or viscoelastic moduli [143]. While particle tracking microrheology techniques can accurately measure particle displacements of $\sim$ nanometers, the modulus of most biologically relevant fibrous gels requires a higher precision than the nanometer scale, and thus passive microrheology has not yet been applied to measure the constitutive properties of a 3D matrix near a cell. Actively displacing particles using an optical or magnetic tweezers shows some promise. A previous study used active microrheology to quantify local matrix mechanical properties near a live cell [144], but the time consuming optical tweezers apparatus limited the number of possible positions to measure matrix constitutive properties. Thus there is a need for development of fast full-field approaches to measure the constitutive properties of an inhomogeneous fibrous matrix. One such approach could use an inverse technique like the Virtual Fields Method (VFM) [145, 146] combined with DVC to measure full-field constitutive properties of a cell-embedded extracellular matrix. The VFM approach has previously been applied to measure constitutive properties of a spherical inclusion in a 3D gel [147], so extending it to a cell-embedded 3D matrix may be feasible. The primary difficulty in applying the VFM to quantify matrix properties for 3D TFM is that the VFM-based constitutive property measurement has the largest uncertainty

on material interfaces. Since cells senses the matrix at the cell–matrix interface, a biologically relevant constitutive property measurement near a cell would remain challenging.

As is highlighted by the difficulty of using the VFM to quantify matrix constitutive properties near a cell, any approach to quantify matrix properties needs to consider the properties sensed by the cell. While a typical cell has a large diameter (~ 10–50 μm) compared to the pore size of a typical matrix (~ 1 μm), the cell also extends thin processes into the matrix with a typical diameter equal to the pore size of the fibrous matrix. Thus, the cell senses the matrix on multiple length scales, and multiscale constitutive approaches spanning from a single fiber to a network of fibers are required to best determine the matrix constitutive properties sensed by the cell. Computational approaches may have an advantage over experimental techniques in multiscale constitutive analysis, because computational approaches can readily take into account the properties of both a single fiber and the structural behavior of a fiber network. The FE model described in Chapter 5 provides a useful starting point for 3D matrix constitutive modeling, and future work could extend on the model to better understand cellular interactions with a 3D matrix.

6.2 Future Trends in Traction Force Microscopy

Besides the technical challenges associated with 3D TFM, a broad range of problems in making traction measurements remain to be addressed. Biological processes are often dynamic and time dependent, meaning that high speed traction force microscopy could yield valuable new insights into biological processes. With the continuous development of higher speed confocal microscopes and cameras, the dynamic imaging capabilities of both 2D and 3D TFM are likely to increase. Spatial resolution can also limit the usefulness of traction measurements. Cells exert tractions to the matrix through cell–matrix adhesion complexes of ~ 1 μm in size. Thus, to truly quantify cell–matrix mechanical interactions, the spatial resolution of a traction measurement should be refined to < 1 μm. With optical microscopy, resolutions much less than

1 μm are not feasible, and therefore developing a new traction measurement approach may be required to quantify the molecular level force transduction within the cell. One example of a new semi-quantitative approach uses a Förster resonance energy transfer (FRET) sensor that signals when the molecular sensor is under tension [148, 149, 150], and research is currently underway to develop these FRET sensors into quantitative tools.

Since controlling all variables in biological experiments is often impossible, biological conclusions must be backed by repeatable statistical data. Currently, TFM is a time consuming experiment, and efforts to increase the rate of data collection ("high throughput traction force microscopy") will enhance the ability of researchers to make biologically relevant statistical conclusions based on TFM experiments. Further biological relevance comes from a better matching between a cell's chemical and physical environment between *in vitro* experiments and *in vivo* conditions. The use of a 3D fibrous matrix for TFM as described here represents a step forward in measuring tractions in a biologically relevant environment. Further progress in this area may include TFM in more complicated 3D cultures or even traction measurements in vivo.

Beyond biology, traction measurements are important in any system that involves interfaces. Thus, the field of tribology, which involves adhesion, friction, and wear, may benefit from the TFM approach developed here. A stress intensity factor in a drying colloidal film has been quantified previously using TFM [151]. A similar approach could be applied to study delamination of films from a substrate. Finally, DVC [54] is currently being applied to investigate tractions between different phases in lithium ion batteries with the goal of preventing fracture between these phases. With the wide range of mechanical problems addressable by TFM, further developments and applications in traction measurements will surely continue in the future.

Appendix A

Continuum Models for a Fibrin Matrix

This appendix describes modeling the fibrin matrix as a homogeneous continuum using previously developed nonlinear strain energy functions. Modeling the fibrin matrix as a continuum offers a simple way of quantifying the deformation in the matrix. Since the matrix tethers (Fig. 5.2) require significant rearrangement of matrix fibers and the experimentally measured strains approach 10%, a constitutive model for large deformation elasticity must be analyzed here. Two strain energy functions based on the Neo-Hookean and Blatz–Ko material models are analyzed here. The results will show that these simple continuum models fail to capture the deformations typically observed in the fibrin matrix. Thus the structural model used in Chapter 5 is more useful for modeling a fibrous matrix.

A.1 Neo-Hookean Material Model

The simplest finite strain constitutive model, the Neo-Hookean model [118], uses a single elastic constant μ in forming the strain energy function Φ,

$$\Phi = \frac{\mu}{2}\left(I_1 - 3\right), \tag{A.1}$$

where I_1 is the first invariant of the left Cauchy–Green deformation tensor $\boldsymbol{B}$. $\boldsymbol{B}$ is related to the deformation gradient tensor $\boldsymbol{F}$ by $\boldsymbol{B} = \boldsymbol{F} \cdot \boldsymbol{F}^T$. It is often convenient to express the

invariant I_1 in terms of the principal stretch ratios $\lambda_i, i = 1, 2, 3$:

$$I_1 = \lambda_1^2 + \lambda_2^2 + \lambda_3^2. \tag{A.2}$$

Here, λ_i is the square root of the i-th eigenvalue of $\boldsymbol{B}$. As written in Eq. (A.1), the Neo-Hookean strain energy assumes the material is incompressible. To account for compressibility, a generalized Neo-Hookean model has been developed [118],

$$\Phi = \frac{\mu}{2}\left(\overline{I}_1 - 3\right) + \frac{K}{2}\left(J - 1\right)^2, \tag{A.3}$$

where $\overline{I}_1 = \overline{\lambda}_1^2 + \overline{\lambda}_2^2 + \overline{\lambda}_3^2$ and $\overline{\lambda}_i = J^{-1/3}\lambda_i$ with $J = \det(\boldsymbol{B})^{1/2} = \lambda_1\lambda_2\lambda_3$. Under small deformations, the constants μ and K in Eq. (A.3) are equal to the shear and bulk moduli of the material, respectively. The use of $\overline{I}_1$ instead of I_1 in Eq. (A.3) is chosen because the term $\overline{I}_1 - 3$ remains unchanged during a purely volumetric deformation. Therefore, Eq. (A.3) separates the shear and volumetric components of the strain energy into two separate parts as can be done for infinitesimal deformation elasticity.

The stress–stretch relationship for a generalized Neo-Hookean material is solved here. Consider a material under uniaxial stress, with principal stretch λ_1 aligned with the stretching direction. Due to symmetry, $\lambda_2 = \lambda_3$. It is useful to write λ_2 in terms of the Jacobian J given by $J = \lambda_1\lambda_2\lambda_3$:

$$\lambda_2 = \sqrt{J/\lambda_1}. \tag{A.4}$$

Eq. (A.3) can be written in terms of principal stretch λ_1 and the Jacobian J:

$$\Phi = \frac{\mu}{2}\left[J^{-2/3}\left(\lambda_1^2 + 2\frac{J}{\lambda_1}\right) - 3\right] + \frac{K}{2}\left(J - 1\right)^2. \tag{A.5}$$

It can be shown [118] that the Cauchy principal stresses are related to the principal stretches

by

$$\sigma_i = \frac{\lambda_i}{J}\frac{\partial U}{\partial \lambda_i}. \tag{A.6}$$

Thus by taking derivatives and rearranging terms,

$$\sigma_1 = \frac{\lambda_1}{J}\frac{\partial U}{\partial \lambda_1} = \frac{2\mu}{3J^{5/3}}\left(\lambda_1^2 - \frac{J}{\lambda_1}\right) + K\left(J-1\right), \tag{A.7}$$

$$\sigma_2 = \frac{\lambda_2}{J}\frac{\partial U}{\partial \sqrt{J/\lambda_1}} = \frac{2\mu}{3J^{5/3}}\left(\frac{J}{\lambda_1} - \lambda_1^2\right) + 2K\left(J-1\right). \tag{A.8}$$

Since in uniaxial tension, $\sigma_2 = 0$, Eq. (A.8) can be rearranged,

$$K\left(J-1\right) = \frac{\mu}{3J^{5/3}}\left(\lambda_1^2 - \frac{J}{\lambda_1}\right), \tag{A.9}$$

and combined with Eq. (A.7) to yield

$$\sigma_1 = \frac{\mu}{J^{5/3}}\left(\lambda_1^2 - \frac{J}{\lambda_1}\right). \tag{A.10}$$

Combining Eqs. (A.7) and (A.10) gives

$$0 = 3KJ^{8/3} - 3KJ^{5/3} + \mu\frac{J}{\lambda_1} - \mu\lambda_1^2. \tag{A.11}$$

To compute the uniaxial stress–stretch relationship for a Neo-Hookean material, the Jacobian J can be computed for any value of stretch λ_1 by numerically solving Eq. (A.11). Then Eq. (A.10) can be solved to determine the stress.

The stress–stretch relationship for the generalized Neo-Hookean model is plotted in Fig. A.1. The "incompressible" curve (for $\nu = 0.5$) shows stiffening with increasing stretch as a result of the Poisson effect. The stretch stiffening is undesirable to simulate longer range propagation of displacements in the matrix, because as stress increases, the material's resistance to stress increases, resulting in more localized deformations. Stretch stiffening does not occur when $\nu = 0$, so lower values of Poisson's ratio would better match the localized fiber

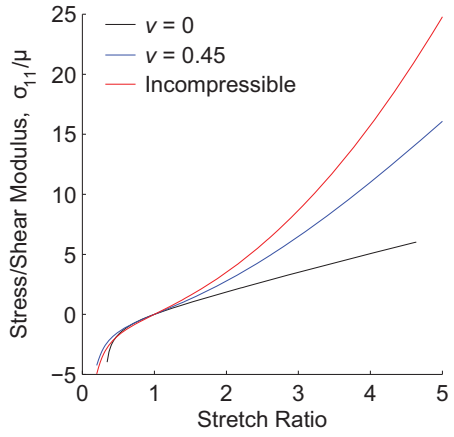

Figure A.1: Stress–stretch curves for the generalized Neo-Hookean model are computed from Eqs. (A.10) and (A.11). Since the stress scales linearly with the shear modulus μ, the data is nondimensionalized. Curves are shown for different values of the small strain Poisson's ratio ν where ν is defined by $\nu = (3K - 2\mu)/2(3K + \mu)$ with K and μ equal to the constants given in Eq. (A.3).

deformation. However, small values of Poisson's ratio fail to match the axial compression experiments described in Chapter 4. In the compression experiments, the matrix tensile stresses on the equator of a rigid sphere (Fig. 4.3) indicate that the Poisson's ratio of the fibrin matrix is > 0.4. In compression, the Neo-Hookean model stiffens drastically when stretch ratios drop below ~ 0.7. Although a stretch ratio of 0.7 represents large deformations, the increased stiffness in compression is probably not representative of the fibrin matrix which would display fiber buckling under compression, and therefore a lower stiffness in compression.

A.2 Blatz–Ko Material Model

A potentially more useful constitutive model than the Neo-Hookean model, which is primarily used for nearly incompressible rubbers, is a model for foams, which have a porous microstructure similar to the fibrin gels studied here. The Blatz–Ko model [152] can be applied to foams by writing the strain energy function in the form

$$\Phi = \frac{\mu}{2}\left(\frac{I_2}{I_3} + 2\sqrt{I_3} - 5\right), \tag{A.12}$$

where I_2 and I_3 are the second and third invariants of the left Cauchy–Green tensor $\boldsymbol{B}$. Again, it is often useful to write the strain energy in terms of the principal stretches:

$$\Phi = \frac{\mu}{2}\left(\frac{1}{\lambda_1^2} + \frac{1}{\lambda_2^2} + \frac{1}{\lambda_3^2} + 2J - 5\right). \tag{A.13}$$

Eq. (A.13) can be generalized to account for different values of Poisson's ratio by including an extra term for volumetric expansion/contraction, similar to the generalized Neo-Hookean model (Eq. (A.3)):

$$\Phi = \frac{2\mu}{\alpha^2}\left[\lambda_1^\alpha + \lambda_2^\alpha + \lambda_3^\alpha + \frac{1}{\beta}\left(J^{-\alpha\beta} - 1\right)\right] \tag{A.14}$$

The uniaxial stress–stretch relationship for the Blatz–Ko material is considered here. Consider a material in uniaxial stress along the 1 direction. The principal stretches are λ_1 and $\lambda_2 = \lambda_3$ in the axial and transverse directions, respectively. Again, the Jacobian $J = \lambda_1\lambda_2\lambda_3$ will be used here. The principal stress–principal stretch relationships can be computed by applying Eq. (A.6) to Eq. (A.14):

$$\sigma_1 = \frac{\lambda_1}{J}\frac{\partial U}{\partial \lambda_1} = \frac{2\mu}{\alpha J}\left(\lambda_1^\alpha - J^{-\alpha\beta}\right), \tag{A.15}$$

$$\sigma_2 = \frac{\lambda_2}{J}\frac{\partial U}{\partial \lambda_2} = \frac{2\mu}{\alpha J}\left(\lambda_2^\alpha - J^{-\alpha\beta}\right). \tag{A.16}$$

Since $\sigma_2 = 0$, setting Eq. (A.16) to zero and solving for λ_2 gives

$$\lambda_2 = \lambda_1^{\frac{-\beta}{1+2\beta}}. \tag{A.17}$$

Finally, substituting Eq. (A.17) into Eq. (A.15) gives the stress-strain relation:

$$\sigma_1 = \frac{2\mu}{\alpha}\left(\lambda_1^{-\frac{\alpha\beta+1}{1+2\beta}} - \lambda_1^{\frac{2\alpha\beta+\alpha-1}{1+2\beta}}\right). \tag{A.18}$$

While Poisson's ratio ν is generally defined only for small strains, the generalized Blatz–Ko model maintains a constant Poisson's ratio for any uniaxial stretch. This can be shown by

defining strain as the logarithm of the stretch ratio, $\epsilon_i = \log(\lambda_i)$, and computing the ratio ϵ_2/ϵ_1:

$$\nu = -\frac{\epsilon_2}{\epsilon_1}, \tag{A.19}$$

$$= -\frac{\log(\lambda_2)}{\log(\lambda_1)}. \tag{A.20}$$

Using the relationship between the principal stretches in Eq. (A.17),

$$\nu = -\frac{\log\left(\lambda_1^{\frac{-\beta}{1+2\beta}}\right)}{\log(\lambda_1)}, \tag{A.21}$$

$$= \frac{\beta}{1+2\beta}\frac{\log(\lambda_1)}{\log(\lambda_1)}, \tag{A.22}$$

$$= \frac{\beta}{1+2\beta}. \tag{A.23}$$

In addition to accounting for different values of Poisson's ratio, the generalized model can account for different exponents on the λ_i terms. For $\alpha = -2$, $\beta = 1/2$, the generalized model reduces to a form similar to the standard Blatz–Ko model. Uniaxial stress–stretch curves for different values of α and Poisson's ratio ν are given in Fig. A.2. Similar to the Neo-Hookean model, stretch stiffening is observed for $\alpha = -5$ when Poisson's ratio is large (Fig. A.2c). For lower values of Poisson's ratio, the generalized Blatz–Ko model shows stress softening and in some cases stress decreases with increasing stretch. The stress softening of the Blatz–Ko model would result in more localized deformation, which would match the constitutive behavior of the fibrin matrix better than the Neo-Hookean model. Furthermore, the generalized Blatz–Ko model does not exhibit stiffening in compression like the Neo-Hookean model. However, traditional models for foams show a plateau region in compression where stress stays constant with increasing compressive strain as a result of buckling of the foam walls [153]. This buckling behavior is not captured in the generalized Blatz–Ko model.

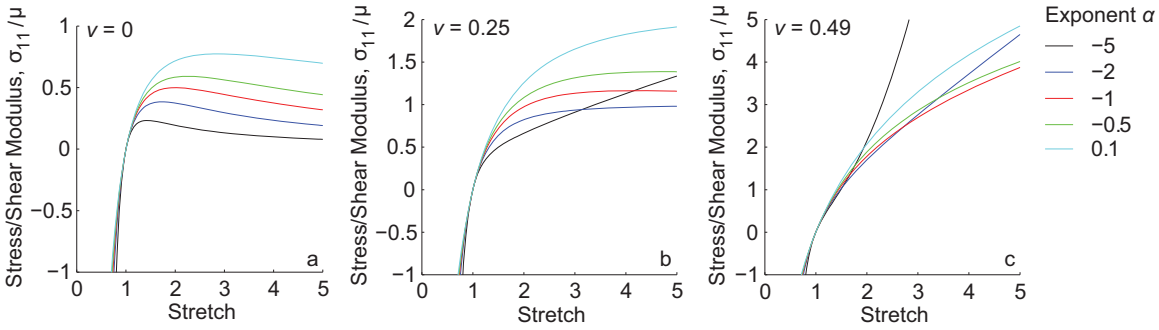

Figure A.2: Stress–stretch curves are computed for the generalized Blatz–Ko material model (Eq. (A.14)) for different values of the exponent α and Poisson's ratio ν. Stress data is nondimensionalized by dividing by shear modulus μ before plotting. The standard Blatz–Ko relationship is given by the curve plotted for $\alpha = -2$, $\nu = 0.25$.

A.3 Displacements in the Continuum Models

While closed form solutions can be written for simple loading conditions like uniaxial stress, more complicated loadings must be simulated using the finite element (FE) method. To model the effect of a localized force applied to the fibrin matrix, a FE model is created (Fig. A.3a) using Abaqus (Dassault Systemes, Waltham, MA). The model uses 200×200 two-dimensional, axisymmetric, 4-node, linear elements with a spacing d to model a square region. A fixed boundary is applied at the bottom of the region, and an upward translation of $4d$ is applied to a single node at the location shown in Fig. A.3a. Contour plots of displacement magnitudes using the generalized Neo-Hookean constitutive model with a Poisson's ratio ν of 0 is shown in Fig. A.3b. While the data shown in Fig. A.3 uses the generalized Neo-Hookean constitutive relationship with $\nu = 0$, the figures look similar and the conclusions are the same for both the generalized Neo-Hookean and generalized Blatz–Ko material models with various values of Poisson's ratio.

The scaling of displacements with distance away from the point force is analyzed by plotting the vertical component of displacement u_y against position along the line $x = 0$ (Fig. A.3c). From Eq. (5.2), the mechanical solution for the dimensionless displacement U induced by a point force in a linear, elastic, infinite continuum scales as $U \sim 1/R$, where R is the dimensionless distance from the point force. The displacements in Fig. A.3c are fit to $U \sim 1/R$,

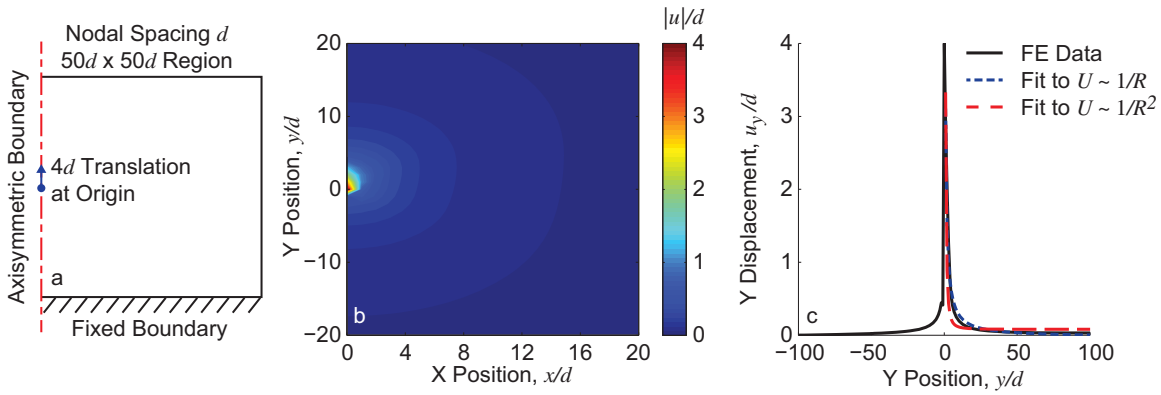

Figure A.3: A FE model is created to simulate a localized force applied by a cell to a hyperelastic continuum. (a) The finite element model uses 200×200 axisymmetric elements with a nodal spacing d to simulate a square region. The square has a fixed boundary at the bottom, and a $4d$ point displacement is applied at the position shown. (b) A contour plot of displacement magnitudes in a localized region around the applied displacement is plotted for the generalized Neo-Hookean model with $\nu = 0$. (c) The scaling of displacements is quantified by fitting the displacements along the line $x = 0$ to $U \sim 1/R$ and $U \sim 1/R^2$, where $U = u_y/d$ and $R = y/d$ are the dimensionless displacement and position.

and for reference they are also fit to $U \sim 1/R^2$. Better agreement is found for the fit to $1/R$ indicating that the hyperelastic model described here behaves similar to a linear, elastic continuum. The $1/R$ relationship also captures the scaling of displacements induced by a cell protrusion, demonstrating that the hyperelastic continuum model has the potential to capture the displacements applied by a cell protrusion to the fibrin matrix.

To compare the continuum models for the matrix to the displacements measured around a rounded cell, an axisymmetric model of a contracting quarter circle of radius a is created in Abaqus (Fig. A.4a). Contraction of a cell is modeled by applying magnitude $0.2a$ inward displacements to the nodes along the edge of the circle. The FE model uses a $20a \times 10a$ region with 400×200 elements. Like for the point force in Fig. A.3, a symmetric boundary is applied at the bottom of the region. Both the generalized Neo-Hookean and generalized Blatz–Ko constitutive relationships are used to solve for the displacements in the square region. Typical results, shown in Fig. A.4b, show a maximum displacement of $0.2a$ at the boundary of the circle that quickly decreases with distance from the circle r.

To quantify the scaling of displacements, the radial displacements are fit to analytical

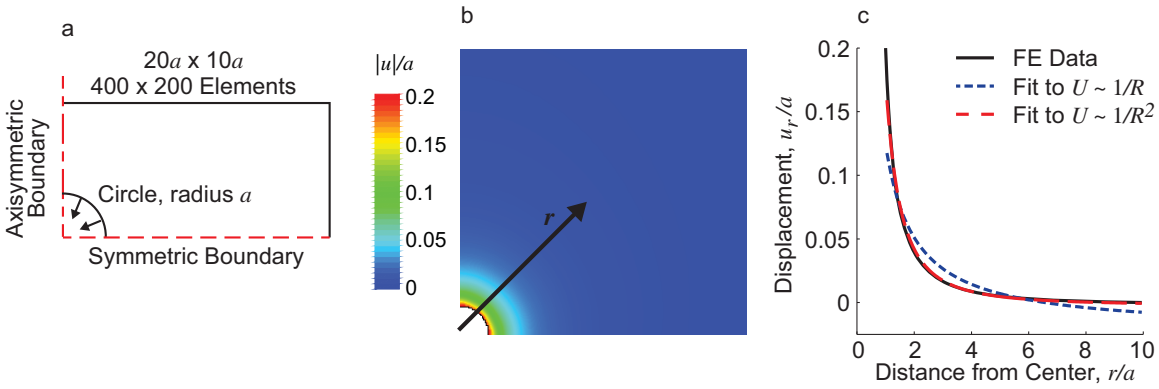

Figure A.4: Contraction of a spherical cell is modeled using a FE simulation. (a) The model uses a quarter circle of radius a in a $20a \times 10a$ axisymmetric region consisting of 400×200 elements with a symmetric bottom boundary. Contraction of the circle is simulated by applying a $0.2a$ inward displacement on the boundary nodes of the circle. (b) Contours of displacements (zoomed in to show detail near the quarter circle) show the scaling of displacements in all directions away from the circle. (c) The dimensionless radial displacement component $U = u_r/a$ is plotted against dimensionless distance from the center of the circle r/a and fit to both $U \sim 1/R$ and $U \sim 1/R^2$.

curves (Fig. A.4c). The linear, elastic solution for a contracting circle given in Eq. (5.1) predicts that displacements scale according to $U \sim 1/R^2$ where U is the radial displacement, and R is the distance from the center of the sphere. In contrast, the displacements measured around a spherical cell scale as $U \sim 1/R$. Here, the displacements fit best to $U \sim 1/R^2$ as clearly seen in Fig. A.4c. While the data shown in Fig. A.4c is for a generalized Neo-Hookean material with Poisson's ratio of $\nu = 0$, the $1/R^2$ scaling holds for both the generalized Neo-Hookean and generalized Blatz–Ko materials with Poisson's ratios varying from 0 to 0.5. Other material models for rubbers (such as the Mooney–Rivlin model [119] or the Arruda–Boyce model [120]) or foams (such as forms of the Blatz–Ko model that use a summation of additional fitting terms) do not change the $1/R^2$ scaling of displacements induced by a contracting sphere. Even a previous more complicated stress-stiffening constitutive model for a continuum that predicted compressive strains near a contracting sphere predicted a displacement scaling of $U \sim 1/R^2$ [154]. Since previously developed continuum models fail to match the experimental displacement scaling of $U \sim 1/R$ around a sphere, a new model is developed as described in Chapter 5.

References

[1] Butcher, D. T., Alliston, T. & Weaver, V. M. A tense situation: forcing tumour progression. *Nature Reviews Cancer* **9**, 108–122 (2009).

[2] Engler, A. J., Sen, S., Sweeney, H. L. & Discher, D. E. Matrix elasticity directs stem cell lineage specification. *Cell* **126**, 677–689 (2006).

[3] Discher, D., Janmey, P. & Wang, Y.-L. Tissue cells feel and respond to the stiffness of their substrate. *Science* **310**, 1139–1143 (2005).

[4] Delcommenne, M. & Streuli, C. H. Control of integrin expression by extracellular-matrix. *Journal of Biological Chemistry* **270**, 26794–26801 (1995).

[5] Bao, G. & Suresh, S. Cell and molecular mechanics of biological materials. *Nature Materials* **2**, 715–725 (2003).

[6] Ingber, D. E. Cellular mechanotransduction: putting all the pieces together again. *FASEB Journal* **20**, 811–827 (2006).

[7] Harris, A. K., Wild, P. & Stopak, D. Silicone-rubber substrata—new wrinkle in the study of cell locomotion. *Science* **208**, 177–179 (1980).

[8] Lee, J., Leonard, M., Oliver, T., Ishihara, A. & Jacobson, K. Traction forces generated by locomoting keratocytes. *Journal of Cell Biology* **127**, 1957–1964 (1994).

[9] Oliver, T., Dembo, M. & Jacobson, K. Traction forces in locomoting cells. *Cell Motility and the Cytoskeleton* **31**, 225–240 (1995).

[10] Dembo, M., Oliver, T., Ishihara, A. & Jacobson, K. Imaging the traction stresses exerted by locomoting cells with the elastic substratum method. *Biophysical Journal* **70**, 2008–2022 (1996).

[11] Dembo, M. & Wang, Y. L. Stresses at the cell-to-substrate interface during locomotion of fibroblasts. *Biophysical Journal* **76**, 2307–2316 (1999).

[12] Crocker, J. C. & Grier, D. G. Methods of digital video microscopy for colloidal studies. *Journal of Colloid and Interface Science* **179**, 298–310 (1996).

[13] Savin, T. & Doyle, P. S. Static and dynamic errors in particle tracking microrheology. *Biophysical Journal* **88**, 623–638 (2005).

[14] Cheezum, M. K., Walker, W. F. & Guilford, W. H. Quantitative comparison of algorithms for tracking single fluorescent particles. *Biophysical Journal* **81**, 2378–2388 (2001).

[15] Sutton, M. Digital image correlation for shape and deformation measurements. In Sharpe, W. (ed.) *Springer Handbook of Experimental Solid Mechanics*, chap. 20, 565–600 (Springer, New York, 2008).

[16] Dally, J. & Riley, W. *Experimental Stress Analysis* (College House Enterprises, Knoxville, TN, 2005), 4 edn.

[17] Wang, N., Ostuni, E., Whitesides, G. M. & Ingber, D. E. Micropatterning tractional forces in living cells. *Cell Motility and the Cytoskeleton* **52**, 97–106 (2002).

[18] Marganski, W. A., Dembo, M. & Wang, Y. L. Measurements of cell-generated deformations on flexible substrata using correlation-based optical flow. *Methods in Enzymology* **361**, 197–211 (2003).

[19] Butler, J. P., Tolic-Norrelykke, I. M., Fabry, B. & Fredberg, J. J. Traction fields, moments, and strain energy that cells exert on their surroundings. *American Journal of Physiology–Cell Physiology* **282**, C595–C605 (2002).

[20] Landau, L. & Lifshitz, E. *Theory of Elasticity* (Butterworth-Heinemann, Oxford, 1986), 3 edn.

[21] Sabass, B., Gardel, M. L., Waterman, C. M. & Schwarz, U. S. High resolution traction force microscopy based on experimental and computational advances. *Biophysical Journal* **94**, 207–220 (2008).

[22] Kraning-Rush, C. M., Carey, S. P., Califano, J. P. & Reinhart-King, C. A. Quantifying traction stresses in adherent cells. In *Computational Methods in Cell Biology*, vol. 110 of *Methods in Cell Biology*, 139–178 (2012).

[23] Tambe, D. T. *et al.* Monolayer stress microscopy: Limitations, artifacts, and accuracy of recovered intercellular stresses. *PLoS One* **8**, e55172 (2013).

[24] Tan, J. L. *et al.* Cells lying on a bed of microneedles: An approach to isolate mechanical force. *Proceedings of the National Academy of Sciences of the United States of America* **100**, 1484–1489 (2003).

[25] del Alamo, J. C. *et al.* Spatio-temporal analysis of eukaryotic cell motility by improved force cytometry. *Proceedings of the National Academy of Sciences of the United States of America* **104**, 13343–13348 (2007).

[26] Yang, Z. C., Lin, J. S., Chen, J. X. & Wang, J. H. C. Determining substrate displacement and cell traction fields—a new approach. *Journal of Theoretical Biology* **242**, 607–616 (2006).

[27] Maloney, J. M., Walton, E. B., Bruce, C. M. & Van Vliet, K. J. Influence of finite thickness and stiffness on cellular adhesion-induced deformation of compliant substrata. *Physical Review E* **78**, 15 (2008).

[28] Sen, S., Engler, A. J. & Discher, D. E. Matrix strains induced by cells: Computing how far cells can feel. *Cellular and Molecular Bioengineering* **2**, 39–48 (2009).

[29] Lin, Y. C. *et al.* Mechanosensing of substrate thickness. *Physical Review E* **82**, 6 (2010).

[30] Boudou, T., Ohayon, J., Picart, C. & Tracqui, P. An extended relationship for the characterization of Young's modulus and Poisson's ratio of tunable polyacrylamide gels. *Biorheology* **43**, 721–728 (2006).

[31] Kandow, C., Georges, P., Janmey, P. & Beningo, K. Polyacrylamide hydrogels for cell mechanics: steps toward optimization and alternative uses. In Wang, Y. & Discher, D. (eds.) *Cell Mechanics*, vol. 83 of *Methods in Cell Biology*, 29–46 (2007).

[32] Maruthamuthu, V., Sabass, B., Schwarz, U. S. & Gardel, M. L. Cell-ECM traction force modulates endogenous tension at cell-cell contacts. *Proceedings of the National Academy of Sciences of the United States of America* **108**, 4708–4713 (2011).

[33] Legant, W. R. *et al.* Multidimensional traction force microscopy reveals out-of-plane rotational moments about focal adhesions. *Proceedings of the National Academy of Sciences of the United States of America* **110**, 881–886 (2013).

[34] Schwarz, U. S. *et al.* Calculation of forces at focal adhesions from elastic substrate data: The effect of localized force and the need for regularization. *Biophysical Journal* **83**, 1380–1394 (2002).

[35] Huang, J. Y. *et al.* Cellular traction force recovery: An optimal filtering approach in two-dimensional Fourier space. *Journal of Theoretical Biology* **259**, 811–819 (2009).

[36] Hur, S. S., Zhao, Y. H., Li, Y. S., Botvinick, E. & Chien, S. Live cells exert 3-dimensional traction forces on their substrata. *Cellular and Molecular Bioengineering* **2**, 425–436 (2009).

[37] Maskarinec, S. A., Franck, C., Tirrell, D. A. & Ravichandran, G. Quantifying cellular traction forces in three dimensions. *Proceedings of the National Academy of Sciences of the United States of America* **106**, 22108–22113 (2009).

[38] Notbohm, J., Kim, J. H., Asthagiri, A. R. & Ravichandran, G. Three-dimensional analysis of the effect of epidermal growth factor on cell-cell adhesion in epithelial cell clusters. *Biophysical Journal* **102**, 1323–1330 (2012).

[39] Lo, C. M., Wang, H. B., Dembo, M. & Wang, Y. L. Cell movement is guided by the rigidity of the substrate. *Biophysical Journal* **79**, 144–152 (2000).

[40] Nelson, C. M. *et al.* Emergent patterns of growth controlled by multicellular form and mechanics. *Proceedings of the National Academy of Sciences of the United States of America* **102**, 11594–11599 (2005).

[41] Yeung, T. *et al.* Effects of substrate stiffness on cell morphology, cytoskeletal structure, and adhesion. *Cell Motility and the Cytoskeleton* **60**, 24–34 (2005).

[42] Griffith, L. G. & Swartz, M. A. Capturing complex 3D tissue physiology in vitro. *Nature Reviews Molecular Cell Biology* **7**, 211–224 (2006).

[43] Juliano, R. L. & Haskill, S. Signal transduction from the extracellular matrix. *Journal of Cell Biology* **120**, 577–585 (1993).

[44] Minsky, M. Microscopy Apparatus, US Patent 3013467 (1957).

[45] Sandison, D. R., Piston, D. W. & Webb, W. W. Background rejection and optimization of signal to noise in confocal microscopy. In Stevens, J. K., Mills, L. R. & Trogadis, J. E. (eds.) *Three-Dimensional Confocal Microscopy: Volume Investigation of Biological Systems*, chap. 2, 29–46 (Academic Press, San Diego, 1994).

[46] Wilson, T. Resolution and optical sectioning in the confocal microscope. *Journal of Microscopy* **244**, 113–121 (2011).

[47] Toomre, D. & Pawley, J. Disk-scanning confocal microscopy. In Pawley, J. (ed.) *Handbook of Biological Confocal Microscopy*, chap. 10, 20–42 (Springer, New York, 2006), 3 edn.

[48] Boyde, A. & Jones, S. J. Mapping and measuring surfaces using reflection confocal microscopy. In Pawley, J. B. (ed.) *Handbook of Biological Confocal Microscopy*, 255–266 (Plenum Press, New York, 1995), 2 edn.

[49] Pawley, J. Fundamental limits in confocal microscopy. In Pawley, J. (ed.) *Handbook of Biological Confocal Microscopy*, chap. 2, 20–42 (Springer, New York, 2006), 3 edn.

[50] Jawerth, L. M., Munster, S., Vader, D. A., Fabry, B. & Weitz, D. A. A blind spot in confocal reflection microscopy: the dependence of fiber brightness on fiber orientation in imaging biopolymer networks. *Biophysical Journal* **98**, L1–L3 (2010).

[51] Yang, C. H. & Mertz, J. Transmission confocal laser scanning microscopy with a virtual pinhole based on nonlinear detection. *Optics Letters* **28**, 224–226 (2003).

[52] Sutton, M., Orteu, J. & Schreier, H. *Image Correlation for Shape, Motion and Deformation Measurements: Basic Concepts, Theory and Applications* (Springer, New York, 2009).

[53] Bay, B. K., Smith, T. S., Fyhrie, D. P. & Saad, M. Digital volume correlation: Three-dimensional strain mapping using X-ray tomography. *Experimental Mechanics* **39**, 217–226 (1999).

[54] Gates, M., Lambros, J. & Heath, M. Towards high performance digital volume correlation. *Experimental Mechanics* **51**, 491–507 (2011).

[55] Forsberg, F., Mooser, R., Arnold, M., Hack, E. & Wyss, P. 3D micro-scale deformations of wood in bending: Synchrotron radiation μCT data analyzed with digital volume correlation. *Journal of Structural Biology* **164**, 255–262 (2008).

[56] Forsberg, F., Sjodahl, M., Mooser, R., Hack, E. & Wyss, P. Full three-dimensional strain measurements on wood exposed to three-point bending: Analysis by use of digital volume correlation applied to synchrotron radiation micro-computed tomography image data. *Strain* **46**, 47–60 (2010).

[57] Hilger, A. *et al.* Revealing microstructural inhomogeneities with dark-field neutron imaging. *Journal of Applied Physics* **107** (2010).

[58] Gilchrist, C., Xia, J., Setton, L. & Hsu, E. High-resolution determination of soft tissue deformations using MRI and first-order texture correlation. *IEEE Transactions on Medical Imaging* **23**, 546–553 (2004).

[59] Franck, C., Hong, S., Maskarinec, S. A., Tirrell, D. A. & Ravichandran, G. Three-dimensional full-field measurements of large deformations in soft materials using confocal microscopy and digital volume correlation. *Experimental Mechanics* **47**, 427–438 (2007).

[60] Liu, L. & Morgan, E. F. Accuracy and precision of digital volume correlation in quantifying displacements and strains in trabecular bone. *Journal of Biomechanics* **40**, 3516–3520 (2007).

[61] Roux, S., Hild, F., Viot, P. & Bernard, D. Three-dimensional image correlation from X-ray computed tomography of solid foam. *Composites Part A–Applied Science and Manufacturing* **39**, 1253–1265 (2008).

[62] Leclerc, H., Perie, J. N., Roux, S. & Hild, F. Voxel-scale digital volume correlation. *Experimental Mechanics* **51**, 479–490 (2011).

[63] Franck, C., Maskarinec, S. A., Tirrell, D. A. & Ravichandran, G. Three-dimensional traction force microscopy: A new tool for quantifying cell-matrix interactions. *PLoS One* **6**, 15 (2011).

[64] Hakkinen, K. M., Harunaga, J. S., Doyle, A. D. & Yamada, K. M. Direct comparisons of the morphology, migration, cell adhesions, and actin cytoskeleton of fibroblasts in four different three-dimensional extracellular matrices. *Tissue Engineering Part A* **17**, 713–724 (2011).

[65] Grinnell, F. Fibroblast biology in three-dimensional collagen matrices. *Trends in Cell Biology* **13**, 264–269 (2003).

[66] Legant, W. R. *et al.* Measurement of mechanical tractions exerted by cells in three-dimensional matrices. *Nature Methods* **7**, 969–971 (2010).

[67] Vitale, G., Preziosi, L. & Ambrosi, D. A numerical method for the inverse problem of cell traction in 3D. *Inverse Problems* **28** (2012).

[68] Koch, T. M., Munster, S., Bonakdar, N., Butler, J. P. & Fabry, B. 3D traction forces in cancer cell invasion. *PLoS One* **7** (2012).

[69] Lesman, A. *et al.* Engineering vessel-like networks within multicellular fibrin-based constructs. *Biomaterials* **32**, 7856–7869 (2011).

[70] Janmey, P. A., Winer, J. P. & Weisel, J. W. Fibrin gels and their clinical and bioengineering applications. *Journal of the Royal Society Interface* **6**, 1–10 (2009).

[71] Kovacs, M., Toth, J., Hetenyi, C., Malnasi-Csizmadia, A. & Sellers, J. Mechanism of blebbistatin inhibition of myosin II. *Journal of Biological Chemistry* **279**, 35557–35563 (2004).

[72] Lucy, L. B. Iterative technique for rectification of observed distributions. *The Astronomical Journal* **79**, 745754 (1974).

[73] di Scalea, F. L., Hong, S. S. & Cloud, G. L. Whole-field strain measurement in a pin-loaded plate by electronic speckle pattern interferometry and the finite element method. *Experimental Mechanics* **38**, 55–60 (1998).

[74] Wolf, K. *et al.* Multi-step pericellular proteolysis controls the transition from individual to collective cancer cell invasion. *Nature Cell Biology* **9**, 893–904 (2007).

[75] Roeder, B. A., Kokini, K., Robinson, J. P. & Voytik-Harbin, S. L. Local, three-dimensional strain measurements within largely deformed extracellular matrix constructs. *Journal of Biomechanical Engineering–Transactions of the ASME* **126**, 699–708 (2004).

[76] Kraning-Rush, C. M., Carey, S. P., Califano, J. P., Smith, B. N. & Reinhart-King, C. A. The role of the cytoskeleton in cellular force generation in 2D and 3D environments. *Physical Biology* **8**, 015009 (2011).

[77] Thery, M. *et al.* The extracellular matrix guides the orientation of the cell division axis. *Nature Cell Biology* **7**, 947–953 (2005).

[78] Fink, J. *et al.* External forces control mitotic spindle positioning. *Nature Cell Biology* **13**, 771–778 (2011).

[79] Burton, K. & Taylor, D. L. Traction forces of cytokinesis measured with optically modified elastic substrata. *Nature* **385**, 450–454 (1997).

[80] Alexandre, P., Reugels, A. M., Barker, D., Blanc, E. & Clarke, J. D. W. Neurons derive from the more apical daughter in asymmetric divisions in the zebrafish neural tube. *Nature Neuroscience* **13**, 673–379 (2010).

[81] Fraley, S. I. *et al.* A distinctive role for focal adhesion proteins in three-dimensional cell motility. *Nature Cell Biology* **12**, 598–604 (2010).

[82] Hirschi, K. K., Rohovsky, S. A., Beck, L. H., Smith, S. R. & D'Amore, P. A. Endothelial cells modulate the proliferation of mural cell precursors via platelet-derived growth factor-bb and heterotypic cell contact. *Circulation Research* **84**, 298–305 (1999).

[83] Paszek, M. J. *et al.* Tensional homeostasis and the malignant phenotype. *Cancer Cell* **8**, 241–254 (2005).

[84] Ridley, A. J. *et al.* Cell migration: integrating signals from front to back. *Science* **302**, 1704–1709 (2003).

[85] Zaman, M. H. *et al.* Migration of tumor cells in 3D matrices is governed by matrix stiffness along with cell-matrix adhesion and proteolysis. *Proceedings of the National Academy of Sciences of the United States of America* **103**, 10889–10894 (2006).

[86] Even-Ram, S. & Yamada, K. M. Cell migration in 3D matrix. *Current Opinion in Cell Biology* **17**, 524–532 (2005).

[87] Doyle, A. D., Wang, F. W., Matsumoto, K. & Yamada, K. M. One-dimensional topography underlies three-dimensional fibrillar cell migration. *Journal of Cell Biology* **184**, 481–90 (2009).

[88] Friedl, P. & Wolf, K. Plasticity of cell migration: a multiscale tuning model. *Journal of Cell Biology* **188**, 11–19 (2010).

[89] Petrie, R. J. & Yamada, K. M. At the leading edge of three-dimensional cell migration. *Journal of Cell Science* **125**, 5917–5926 (2012).

[90] Dobereiner, H.-G., Dubin-Thaler, B., Giannone, G., Xenias, H. & Sheetz, M. Dynamic phase transitions in cell spreading. *Physical Review Letters* **93**, 108105 (2004).

[91] Chamaraux, F., Fache, S., Bruckert, F. & Fourcade, B. Kinetics of cell spreading. *Physical Review Letters* **94**, 158102 (2005).

[92] Xiong, Y. *et al*. Mechanisms controlling cell size and shape during isotropic cell spreading. *Biophysical Journal* **98**, 2136–2146 (2010).

[93] Friedl, P. & Wolf, K. Proteolytic interstitial cell migration: a five-step process. *Cancer and Metastasis Reviews* **28**, 129–135 (2009).

[94] Wolf, K. & Friedl, P. Mapping proteolytic cancer cell-extracellular matrix interfaces. *Clinical and Experimental Metastasis* **26**, 289–298 (2009).

[95] Reinhart-King, C. A., Dembo, M. & Hammer, D. A. The dynamics and mechanics of endothelial cell spreading. *Biophysical Journal* **89**, 676–89 (2005).

[96] Chaudhuri, S., Nguyen, H., Rangayyan, R. M., Walsh, S. & Frank, C. B. A Fourier domain directional filtering method for analysis of collagen alignment in ligaments. *IEEE Transactions on Biomedical Engineering* **34**, 509–518 (1987).

[97] Petroll, W. M., Cavanagh, H. D., Barry, P., Andrews, P. & Jester, J. V. Quantitative analysis of stress fiber orientation during corneal wound contraction. *Journal of Cell Science* **104**, 353–363 (1993).

[98] Goodier, J. Concentration of stress around spherical and cylindrical inclusions and flaws. *Journal of Applied Mechanics* **1**, 39–44 (1933).

[99] Dikovsky, D., Bianco-Peled, H. & Seliktar, D. Defining the role of matrix compliance and proteolysis in three-dimensional cell spreading and remodeling. *Biophysical Journal* **94**, 2914–2925 (2008).

[100] Beer, F., Johnston, E. & DeWolf, J. *Mechanics of Materials* (McGraw–Hill, New York, 2002), 3 edn.

[101] Boal, D. *Mechanics of the Cell* (Cambridge University Press, Cambridge, 2002).

[102] Wolf, K. & Friedl, P. Extracellular matrix determinants of proteolytic and non-proteolytic cell migration. *Trends in Cell Biology* **21**, 736–744 (2011).

[103] Packard, B. Z., Artym, V. V., Komoriya, A. & Yamada, K. M. Direct visualization of protease activity on cells migrating in three-dimensions. *Matrix Biology* **28**, 3–10 (2009).

[104] Pelham, R. J. & Wang, Y. L. Cell locomotion and focal adhesions are regulated by substrate flexibility. *Proceedings of the National Academy of Sciences of the United States of America* **94**, 13661–13665 (1997).

[105] Klein, E. A. *et al.* Cell-cycle control by physiological matrix elasticity and in vivo tissue stiffening. *Current Biology* **19**, 1511–1518 (2009).

[106] Kim, J. H. & Asthagiri, A. R. Matrix stiffening sensitizes epithelial cells to EGF and enables the loss of contact inhibition of proliferation. *Journal of Cell Science* **124**, 1280–1287 (2011).

[107] Krishnan, R. *et al.* Substrate stiffening promotes endothelial monolayer disruption through enhanced physical forces. *American Journal of Physiology–Cell Physiology* **300**, C146–C154 (2011).

[108] Saez, A., Buguin, A., Silberzan, P. & Ladoux, B. Is the mechanical activity of epithelial cells controlled by deformations or forces? *Biophysical Journal* **89**, L52–L54 (2005).

[109] Parker, K. K. *et al.* Directional control of lamellipodia extension by constraining cell shape and orienting cell tractional forces. *FASEB Journal* **16** (2002).

[110] Brown, R. A., Prajapati, R., McGrouther, D. A., Yannas, I. V. & Eastwood, M. Tensional homeostasis in dermal fibroblasts: Mechanical responses to mechanical loading in three-dimensional substrates. *Journal of Cellular Physiology* **175**, 323–332 (1998).

[111] Takemasa, T., Sugimoto, K. & Yamashita, K. Amplitude-dependent stress fiber reorientation in early response to cyclic strain. *Experimental Cell Research* **230**, 407–410 (1997).

[112] De, R., Zemel, A. & Safran, S. A. Dynamics of cell orientation. *Nature Physics* **3**, 655–659 (2007).

[113] De, R., Zemel, A. & Safran, S. A. Do cells sense stress or strain? Measurement of cellular orientation can provide a clue. *Biophysical Journal* **94**, L29–L31 (2008).

[114] Yip, A. K. *et al.* Cellular response to substrate rigidity is governed by either stress or strain. *Biophys J* **104**, 19–29 (2013).

[115] Bischofs, I. B. & Schwarz, U. S. Cell organization in soft media due to active mechanosensing. *Proceedings of the National Academy of Sciences of the United States of America* **100**, 9274–9279 (2003).

[116] Reinhart-King, C. A., Dembo, M. & Hammer, D. A. Cell-cell mechanical communication through compliant substrates. *Biophysical Journal* **95**, 6044–6051 (2008).

[117] Eshelby, J. D. The elastic field outside an ellipsoidal inclusion. *Proceedings of the Royal Society of London Series A–Mathematical and Physical Sciences* **252**, 561–569 (1959).

[118] Bower, A. *Applied Mechanics of Solids* (Taylor & Francis, Boca Raton, FL, 2011).

[119] Mooney, M. A theory of large elastic deformation. *Journal of Applied Physics* **11**, 582–592 (1940).

[120] Arruda, E. M. & Boyce, M. C. A three-dimensional constitutive model for the large stretch behavior of rubber elastic materials. *Journal of the Mechanics and Physics of Solids* **41**, 389–412 (1993).

[121] Maksym, G. N., Fredberg, J. J. & Bates, J. H. T. Force heterogeneity in a two-dimensional network model of lung tissue elasticity. *Journal of Applied Physiology* **85**, 1223–1229 (1998).

[122] Onck, P., Koeman, T., van Dillen, T. & van der Giessen, E. Alternative explanation of stiffening in cross-linked semiflexible networks. *Physical Review Letters* **95**, 178102 (2005).

[123] Heussinger, C. & Frey, E. Stiff polymers, foams, and fiber networks. *Physical Review Letters* **96**, 017802 (2006).

[124] Conti, E. & MacKintosh, F. Cross-linked networks of stiff filaments exhibit negative normal stress. *Physical Review Letters* **102**, 088102 (2009).

[125] Ma, B. & Bates, J. H. T. Continuum vs. spring network models of airway-parenchymal interdependence. *Journal of Applied Physiology* **113**, 124–129 (2012).

[126] Haut, R. C. & Little, R. W. A constitutive equation for collagen fibers. *Journal of Biomechanics* **5**, 423–430 (1972).

[127] Storm, C., Pastore, J. J., MacKintosh, F. C., Lubensky, T. C. & Janmey, P. A. Nonlinear elasticity in biological gels. *Nature* **435**, 191–194 (2005).

[128] Collet, J. P., Shuman, H., Ledger, R. E., Lee, S. & Weisel, J. W. The elasticity of an individual fibrin fiber in a clot. *Proceedings of the National Academy of Sciences of the United States of America* **102**, 9133–9137 (2005).

[129] Piechocka, I. K., Bacabac, R. G., Potters, M., Mackintosh, F. C. & Koenderink, G. H. Structural hierarchy governs fibrin gel mechanics. *Biophysical Journal* **98**, 2281–2289 (2010).

[130] Marko, J. F. & Siggia, E. D. Stretching DNA. *Macromolecules* **28**, 8759–8770 (1995).

[131] Liu, W. *et al.* Fibrin fibers have extraordinary extensibility and elasticity. *Science* **313**, 634–634 (2006).

[132] Timoshenko, S. P. & Goodier, J. N. *Theory of Elasiticity* (McGraw-Hill, New York, 1970), 3 edn.

[133] Brown, A. E., Litvinov, R. I., Discher, D. E., Purohit, P. K. & Weisel, J. W. Multiscale mechanics of fibrin polymer: gel stretching with protein unfolding and loss of water. *Science* **325**, 741–474 (2009).

[134] Purohit, P. K., Litvinov, R. I., Brown, A. E., Discher, D. E. & Weisel, J. W. Protein unfolding accounts for the unusual mechanical behavior of fibrin networks. *Acta Biomaterialia* **7**, 2374–2383 (2011).

[135] Moore, B., Jaglinski, T., Stone, D. S. & Lakes, R. S. Negative incremental bulk modulus in foams. *Philosophical Magazine Letters* **86**, 651–659 (2006).

[136] Lakes, R. & Wojciechowski, K. W. Negative compressibility, negative Poisson's ratio, and stability. *Physica Status Solidi B* **245**, 545–551 (2008).

[137] Gatt, R. & Grima, J. N. Negative compressibility. *Physica Status Solidi–Rapid Research Letters* **2**, 236–238 (2008).

[138] Janmey, P. A. *et al.* Negative normal stress in semiflexible biopolymer gels. *Nature Materials* **6**, 48–51 (2007).

[139] Poynting, J. H. On pressure perpendicular to the shear planes in finite pure shears, and on the lenghtening of loaded wires when twisted. *Proceedings of the Royal Society of London Series A* **82**, 546–559 (1909).

[140] Winer, J. P., Oake, S. & Janmey, P. A. Non-linear elasticity of extracellular matrices enables contractile cells to communicate local position and orientation. *PLoS One* **4** (2009).

[141] Mato, J. M., Losada, A., Nanjundiah, V. & Konijn, T. M. Signal input for a chemotactic response in the cellular slime mold dictyostelium discoideum. *Proceedings of the National Academy of Sciences of the United States of America* **72**, 4991–4993 (1975).

[142] Parent, C. A. & Devreotes, P. N. A cell's sense of direction. *Science* **284**, 765–770 (1999).

[143] Wirtz, D. Particle-tracking microrheology of living cells: Principles and applications. *Annual Review of Biophysics* **38**, 301–326 (2009).

[144] Kotlarchyk, M. A. *et al.* Concentration independent modulation of local micromechanics in a fibrin gel. *PLoS One* **6**, e20201 (2011).

[145] Grediac, M., Pierron, F., Avril, S. & Toussaint, E. The virtual fields method for extracting constitutive parameters from full-field measurements: A review. *Strain* **42**, 233–253 (2006).

[146] Toussaint, E., Grediac, M. & Pierron, F. The virtual fields method with piecewise virtual fields. *International Journal of Mechanical Sciences* **48**, 256–264 (2006).

[147] Avril, S., Huntley, J. M., Pierron, F. & Steele, D. D. 3D heterogeneous stiffness reconstruction using MRI and the virtual fields method. *Experimental Mechanics* **48**, 479–494 (2008).

[148] Kong, H. J., Polte, T. R., Alsberg, E. & Mooney, D. J. FRET measurements of cell-traction forces and nano-scale clustering of adhesion ligands varied by substrate stiffness. *Pro-*

ceedings of the National Academy of Sciences of the United States of America **102**, 4300–4305 (2005).

[149] Grashoff, C. *et al.* Measuring mechanical tension across vinculin reveals regulation of focal adhesion dynamics. *Nature* **466**, 263–266 (2010).

[150] Meng, F., Suchyna, T. M., Lazakovitch, E., Gronostajski, R. M. & Sachs, F. Real time FRET based detection of mechanical stress in cytoskeletal and extracellular matrix proteins. *Cellular and Molecular Bioengineering* **4**, 148–159 (2011).

[151] Xu, Y. *et al.* Imaging in-plane and normal stresses near an interface crack using traction force microscopy. *Proceedings of the National Academy of Sciences of the United States of America* **107**, 14964–14967 (2010).

[152] Blatz, P. J. & Ko, W. L. Application of finite elastic theory to the deformation of rubbery materials. *Transactions of the Society of Rheology* **6**, 223–251 (1962).

[153] Gibson, L. J. Biomechanics of cellular solids. *Journal of Biomechanics* **38**, 377–399 (2005).

[154] Shokef, Y. & Safran, S. A. Scaling laws for the response of nonlinear elastic media with implications for cell mechanics. *Physical Review Letters* **108**, 178103 (2012).